博士論文

Global Linear Stability Analysis of Compressible Vortical Flows
（圧縮性渦流れの全体安定性解析に関する研究）

大道　勇哉

Doctoral Thesis

Global Linear Stability Analysis of Compressible Vortical Flows

Yuya Ohmichi

Department of Advanced Energy,
Graduate School of Frontier Sciences, The University of Tokyo
February 2014

Contents

List of Figures

List of Tables

1 Introduction

1.1 Background

1.1.1 Flow stability

A flow stability analysis is one of the most important subjects in fluid dynamics because flow instability often appears in practical flows. For example, if an object has a symmetry shape, a symmetric and steady flow around the object is apparently a candidate solution of its governing equations. However, in practical flows, the flow is usually asymmetry and unsteady, and often includes vortex formations. This is because the symmetric solution is unstable. More specifically, if the symmetric flow is perturbed, then the perturbations grow in time, the flow is broken, and the symmetric flow state transits to other flow states. The stability analysis of flow is the analysis in terms of such transitions, and it has been investigated from 1800s.[1]

The flow stability is important for engineering purposes. For example, vortices generated by cylinder-shaped structures, which is called Kármán vortices, make noise. Therefore, reduction of the loud noise caused by the cylinder-shaped structures is important for developments of automobiles, trains, buildings, and so on. To reduce the noise, stabilizing effect of contriving the shapes on such flows have been investigated.[2] On the other hand, vortices also have good effects, namely, momentum and scalar transports. These effects can be useful for a mixing of combustion air and fuels. By the use of vortex breakdowns which induces small vortices into a flowfield of a combustor, the mixing of the fuels are enhanced. Therefore, improvements of the combustion efficiency by the generations and breakdowns of vortices have been heavily investigated. However, it has been found that in the case of compressible flows, a mixing layer is stabilized by the compressibility.[3–9] Thus, the study of the compressibility effects on the stability of vorical flows is important for the development of the method to enhance the mixing in compressible flows.

The compressibility effects on the growth rate of a mixing layer have been investigated by many researchers.[3–9] Their results showed that if the convective Mach number is greater than about 0.3, the compressibility effects appear and the growth rate of a mixing layer rapidly decreases, and if the convective Mach number is greater than about 0.6, the flow becomes three-dimensional. Interestingly, a conventional linear stability analysis of a compressible mixing layer shows good agreement with experimental results which show the decrease of the growth rate by increasing of the Mach number. The linear stability analysis conducted by Sandham and Reynolds[8] revealed that the baroclinic and dilatational effects, which are caused by the compressibility, stabilize a mixing layer and deform the shape of vortices.

As mentioned above, it was demonstrated that the linear stability analysis is important and helpful for investigating the nature of flowfields. However, to derive tractable problems, the conventional linear stability analyses usually assume that a flowfield is a parallel flow, although most practical flows are not parallel. To elucidate the practical flow accurately, it is necessary to employ the stability analysis without such an assumption. In this study, we will conduct the linear stability analysis which does not employ the assumption about a geometry of flowfields.

1.1.2 Global linear stability analysis

The linear stability analysis with no assumption about the flow geometry is called the global linear stability analysis. The global linear stability analysis is contrasted with the conventional local linear stability analysis.

The local linear stability analysis assumes that the variation of perturbations is written by the following form:

$$\boldsymbol{q}'(x,\ y,\ t) = \hat{\boldsymbol{q}}(y)\exp(\lambda t - \alpha x) \tag{1.1}$$

where $(x,\ y)$, t, and $\lambda t - \alpha x$ denote spatial coordinates, time, and a phase function, respectively. This means that the conventional local linear stability analysis assumes a parallel flow expressed by a function of only one spatial variable y.

On the other hand, the global linear stability analysis assumes the following form:

$$\boldsymbol{q}'(x,\ y,\ t) = \hat{\boldsymbol{q}}(x,\ y)\exp(\lambda t) \tag{1.2}$$

This means that the global linear stability analysis permits the form of the perturbation (mode shape) $\hat{\boldsymbol{q}}$ to be expressed by two (or three in the case of three-dimensional analysis) spatial

variables. Thus, the global linear stability analysis can produce more accurate results than the conventional local linear stability analysis.

In the global linear stability analysis, the terms $\hat{\boldsymbol{q}}(x, y)$ and λ of Eq. 1.2 are found. Both terms can be a complex number. The real and imaginary parts of $\hat{\boldsymbol{q}}(x, y)$ represent the mode shape. The real part of λ, denoted σ hereinafter, represents a growth rate, and the imaginary part of λ, denoted ω hereinafter, represents an angular frequency.

Because the global linear stability analysis can deal with any flow geometry, this method can be used for a variety of practical flows such as flows appeared in the engineering. Moreover, this method is also helpful for developing flow control techniques, which is closely related to the flow stability.[10] It is believed that the global linear stability analysis can be used to find the location for controlling global instabilities of flowfields, and to develop reduced-order models (ROMs) for flow-control systems.[11]

1.1.3 Numerical methods for global linear stability analysis

There are two numerical methods for calculating the mode shape $\hat{\boldsymbol{q}}(x, y)$, the growth rate σ, and the angular frequency ω.

The one is the residual algorithm.[12,13] This method performs the temporal integration of the governing equations of fluids, and then extracts the mode shape, the growth rate, and the angular frequency from the temporal variation of the perturbations by some methods such as a least-squares method. This method is relatively easy to perform because it uses the routine of conventional CFD (Computational Fluid Dynamics) and its computational cost is cheap. However, this method can calculate only one mode, namely the most unstable or least stable mode.

The other is the method that solves an eigenvalue problem. This method firstly derives the following eigenvalue problem Eq. 1.3 by substituting the perturbation Eq. 1.2 to its governing equations, and then solves it.

$$\boldsymbol{A}\hat{\boldsymbol{q}} = \lambda\hat{\boldsymbol{q}} \tag{1.3}$$

Unlike the residual algorithm, this method can calculate multiple modes although its computational cost is relatively expensive. In this study, we will use this method.

The numerical methods for solving the eigenvalue problem Eq. 1.3 of the global linear stability analysis can be classified into two categories, namely the matrix-forming method[14–17] and the matrix-free method.[18–25] The former method constructs the matrix $\boldsymbol{A}$ of Eq. 1.3, which is a huge matrix and represents a discretization of operators of linearized governing equations. On the other hand, the latter method does not construct any matrix, and therefore the memory requirement of this method is significantly smaller than that of the matrix-forming method.

A time-stepping method is one of the matrix-free method which was introduced by Eriksson and Rizzi.[20] They developed this method to analyze the stability of numerical schemes for solving the compressible Euler equations. Then, Chiba[18,19] extended this method to incompressible viscous flows and employed it to analyze the linear stability of the two-dimensional cavity and circular cylinder wake flows. Therefore, this method is also called Chiba's method. Takeuchi et al.[21] successfully applied the time-stepping method to the three-dimensional incompressible flow analysis of a round jet. Tezuka and Suzuki[22] also successfully analyzed the three-dimensional incompressible flows around a spheroid by time-stepping method.

The major feature of the time-stepping method is that this method is based on a conventional CFD. A spectral transformation, which is necessary to solve an eigenvalue problem with an iterative method and (explained in Chapter 2), is performed by using a routine for a temporal integration of a CFD code. Therefore, the code of global linear stability analysis with the time-stepping method can be developed by adding a small modification to a conventional CFD code. Because of this simplicity of coding and the low memory requirement, the time-stepping method is highly practical for science and engineering purposes.

In the recent ten years, the number of studies on the global linear stability analysis has been increasing[26,27] with the rapid development of computers. However, the number of studies on compressible flows is still limited. Especially, the analysis of flowfields including shock waves is not found except for the work of Crouch et al.[16,17] Therefore, a standard method of the global linear stability analysis for compressible flows has not been established yet. The global linear stability analysis of unsteady compressible flows is important because they appear in many practical problems, such as compressible turbulent flows, the aeroacoustics, and wake flows behind a supersonic vehicle.

1.2 Objectives

Based on the above discussions, the objectives of this study are as follows:

- To develop a method of the global linear stability analysis for compressible flows
- To elucidate compressibility effects on the global linear stability of a cavity vortex

In terms of the first objective, we will develop a numerical method of the global linear stability analysis which has the high-order spatial accuracy and the low memory requirement. This aims at constructing the method for the turbulent and aeroacoustics analyses which are believed to be desired for future works. The second objective is related to the stabilizing effect of compressibility on shear layers which was mentioned above. If the compressibility effects on a cavity vortex is well understood, it is also helpful for the understanding of the stability of shear layer flows because the stability of the cavity flows is closely related to it, which will be described in Chapter 5.

In addition, through this thesis, we would like to show that the global linear stability analysis is helpful for understanding transition and unsteady phenomena.

1.3 Outline of this thesis

The outline of this thesis is as follows. First, in Chapter 2, theoretical consideration and numerical methods of the global linear stability analysis are explained. Then, numerical methods for fluid simulations are presented in Chapter 3. The global linear stability analysis is achieved by combining the methods of Chapters 2 and 3. In Chapter 4, we discuss about desired properties of a numerical method for future global linear stability analyses, and propose the method which satisfies the properties. The proposed method will be used in Chapter 5. In Chapter 5, the global linear stability of a compressible cavity vortex is conducted. Compressibility effects on the global linear stability of a cavity vortex is investigated in detail. Finally, in Chapter 6, the results of this thesis are summarized.

2 Global Linear Stability Analysis

2.1 Formulation of linear stability analysis

A governing equation of fluids, such as compressible Navier-Stokes and Euler equations, can be written in the following form:

$$\frac{d\boldsymbol{q}}{dt} = \boldsymbol{f}(\boldsymbol{q}) \tag{2.1}$$

Because the global linear stability analysis is a numerical analysis, the governing equation Eq. 2.1 is discretized. Thus, $\boldsymbol{q}$ is a vector of fluid variables, such as

$$\boldsymbol{q} = [q_1, q_2, \ldots, q_{4N-1}, q_{4N}]^T \tag{2.2}$$

$$= [\rho_1, u_1, v_1, p_1, \ldots, \rho_N, u_N, v_N, p_N]^T \tag{2.3}$$

for the case of two-dimensional compressible flow. The choice of fluid variables has an arbitrariness. The subscripts $1, 2, \ldots, N$ of Eq. 2.3 denote the index of a computational grid and N is the total number of the grid points. The subscripts $1, 2, \ldots, 4N$ of Eq. 2.2 correspond to a global numbering. $\boldsymbol{f}$ is a vector-valued function as following:

$$\boldsymbol{f} = [f_1(q_1, \ldots, q_{4N}), f_2(q_1, \ldots, q_{4N}), \ldots, f_{4N-1}(q_1, \ldots, q_{4N}), f_{4N}(q_1, \ldots, q_{4N})]^T \tag{2.4}$$

When small perturbations $\boldsymbol{q}'$ are superimposed to the basic state $\bar{\boldsymbol{q}}$, the perturbations satisfy the following equation:

$$\frac{d\boldsymbol{q}'}{dt} = \boldsymbol{A}\boldsymbol{q}' \tag{2.5}$$

where $\boldsymbol{A}$ is a Jacobian matrix defined by,

$$\boldsymbol{A} \equiv \left(\frac{\partial \boldsymbol{f}}{\partial \boldsymbol{q}}\right)_{\boldsymbol{q}=\bar{\boldsymbol{q}}} \tag{2.6}$$

and, can be written in a matrix form,

$$\boldsymbol{A} = \begin{bmatrix} \dfrac{\partial f_1}{\partial q_1} & \cdots & \dfrac{\partial f_1}{\partial q_{4N}} \\ \vdots & \ddots & \vdots \\ \dfrac{\partial f_{4N}}{\partial q_1} & \cdots & \dfrac{\partial f_{4N}}{\partial q_{4N}} \end{bmatrix} \tag{2.7}$$

When the temporal variation of the Jacobian matrix $\boldsymbol{A}$ is assumed to be small enough, the following decomposition can be applied to the perturbations $\boldsymbol{q}'$,

$$\boldsymbol{q}'(x, y, t) = \hat{\boldsymbol{q}}(x, y)\exp(\lambda t) \tag{2.8}$$

Finally, the eigenvalue problem is obtained by substituting Eq. 2.8 to Eq. 2.5,

$$\boldsymbol{A}\hat{\boldsymbol{q}} = \lambda\hat{\boldsymbol{q}} \tag{2.9}$$

where, $\lambda = \sigma + i\omega$ and $\hat{\boldsymbol{q}} = \hat{\boldsymbol{q}}_r + i\hat{\boldsymbol{q}}_i$ are the eigenvalue and eigenvector of the matrix $\boldsymbol{A}$, respectively. The eigenvector $\hat{\boldsymbol{q}}$ describes the mode shape. The real part σ and imaginary part ω of an eigenvalue describes the growth (or damping) rate and the angular frequency, respectively.

Consequently, the linear stability of the corresponding eigenvector $\hat{\boldsymbol{q}}$ is decided as follows:

$$\begin{aligned} \sigma > 0 \quad & \text{unstable} \\ \sigma = 0 \quad & \text{neutrally stable} \\ \sigma < 0 \quad & \text{stable} \end{aligned} \tag{2.10}$$

Therefore, when the largest growth rate σ is positive, the basic state $\overline{\boldsymbol{q}}$ is unstable.

The dimensions of the Jacobian matrix $\boldsymbol{A}$ is proportional to the number of grid points used in the numerical simulation (CFD), and is typically $O(10^4)$ - $O(10^5)$ for the two-dimensional case and $O(10^6)$ - $O(10^8)$ for the three-dimensional case. Therefore, it is difficult to solve the eigenvalue problem Eq. 2.9 with direct methods because of high computational memory requirements. Moreover, to form the Jacobian matrix $\boldsymbol{A}$ including boundary conditions is not easy. In the global linear stability analysis used in this study, these difficulties are avoided by using approaches of a JFNK (Jacobian-Free Newton-Krylov) method.[28] In the following sections, the approaches which have been successfully applied by many researchers[18–25] will be explained.

2.2 Arnoldi method

The Arnoldi method[29] is an iterative method to solve a large-scale eigenvalue problem. The Arnoldi method assumes that the eigenvectors corresponding to the M largest eigenvalues of an matrix $\boldsymbol{A}$ can be approximated by the basis of the following Krylov subspace $\boldsymbol{K}_n$.

$$\boldsymbol{K}_n = \left[\boldsymbol{b} \quad \boldsymbol{A}\boldsymbol{b} \quad \boldsymbol{A}^2\boldsymbol{b} \cdots \boldsymbol{A}^{M-1}\boldsymbol{b}\right] \tag{2.11}$$

$\boldsymbol{b}$: arbitrary vector

When the orthonormal vectors of $\boldsymbol{K}_n$ are denoted $\boldsymbol{\zeta}_k$ and a orthogonal matrix $\boldsymbol{V}_M$ is defined by the sequence of $\boldsymbol{\zeta}_k$, the approximate eigenvectors $\boldsymbol{\varphi}$ can be written as follows:

$$\boldsymbol{\varphi} = z_1\boldsymbol{\zeta}_1 + z_2\boldsymbol{\zeta}_2 + \cdots + z_M\boldsymbol{\zeta}_M = \boldsymbol{V}_M\boldsymbol{z} \tag{2.12}$$

$$\boldsymbol{z} = [z_1, z_2, \ldots, z_M]^T \tag{2.13}$$

Here, $\boldsymbol{z}$ is a coefficient vector. By substituting the approximate eigenvector Eq. 2.12 to the eigenvalue problem Eq. 2.9, a low-dimensional eigenvalue problem is derived.

$$\boldsymbol{V}_M{}^T\boldsymbol{A}\boldsymbol{V}_M\boldsymbol{z} = \lambda\boldsymbol{z} \quad (\text{where} \quad \boldsymbol{V}_M{}^T\boldsymbol{V}_M = \boldsymbol{I}) \tag{2.14}$$

The matrix $\boldsymbol{V}_M{}^T\boldsymbol{A}\boldsymbol{V}_M$ are calculated by the following algorithm:

Choose an arbitrary vector $\boldsymbol{q}_1$

$$\boldsymbol{\zeta}_1 = (\boldsymbol{q}_1 \cdot \boldsymbol{q}_1)^{-1/2}\boldsymbol{q}_1 \tag{2.15}$$

for $k = 1$ to M

$$\boldsymbol{q}_{k+1} = \boldsymbol{A}\boldsymbol{\zeta}_k - \sum_{j=1}^{k} h_{j,k}\boldsymbol{\zeta}_j \tag{2.16}$$

$$h_{j,k} = \boldsymbol{\zeta}_j \cdot \boldsymbol{A}\boldsymbol{\zeta}_k \tag{2.17}$$

$$h_{k+1,k} = (\boldsymbol{q}_{k+1} \cdot \boldsymbol{q}_{k+1})^{1/2} \tag{2.18}$$

$$\boldsymbol{\zeta}_{k+1} = \boldsymbol{q}_{k+1}/h_{k+1,k} \tag{2.19}$$

end

where, $h_{j,k}$ is an element of the matrix $\boldsymbol{V}_M{}^T\boldsymbol{A}\boldsymbol{V}_M$, and forms a upper Hessenberg matrix $\boldsymbol{H}$. The dimension of this matrix $\boldsymbol{H}$, which equals to M, is small enough to solve by direct methods.

The approximate eigenvector $\boldsymbol{\varphi}$ is calculated by using the eigenvectors and eigenvalues of the matrix $\boldsymbol{H} = \boldsymbol{V}_M{}^T \boldsymbol{A} \boldsymbol{V}_M$,

$$\boldsymbol{H}\boldsymbol{\psi}_j = \lambda_j \boldsymbol{\psi}_j \quad (j = 1, 2, \ldots, M) \tag{2.20}$$

$$\boldsymbol{\varphi}_j = \sum_{k=1}^{M} \left(\boldsymbol{\psi}_j\right)_k \zeta_k \tag{2.21}$$

where, λ_j is an eigenvalue of the matrix $\boldsymbol{H}$ (as explained above, λ_j is also an approximate eigenvalue of the matrix $\boldsymbol{A}$). The $\boldsymbol{\psi}_j$ and $\boldsymbol{\varphi}_j$ are the eigenvectors of the matrix $\boldsymbol{H}$ and the matrix $\boldsymbol{A}$, respectively. $\left(\boldsymbol{\psi}_j\right)_k$ denotes the k-th element of $\boldsymbol{\psi}_j$.

The description of this section follows the thesis of Chiba.[18, 19]

2.3 Spectral transformation

As expected from the similarity of the power method and the Krylov subspace (Eq. 2.11) of the Arnoldi method, the Arnoldi method can obtain the eigenvalues which have a large absolute value, and corresponding eigenvectors. On the other hand, the modes which we need to analyze here have a large real part, which means a low stability, and do not always have a large absolute value. Therefore, the global linear stability analysis needs the spectral transformation in order to make the absolute value of the desired stability modes large. In this study, two methods for the spectral transformation are introduced.

2.3.1 Time-stepping method (Chiba's Method)

The time-stepping method was proposed by Eriksson and Rizzi[20] as a method for analyzing the stability of numerical methods for the compressible Euler equations. Later, Chiba[18, 19] successfully applied the time-stepping method to the physical stability analysis of incompressible flows. Therefore, time-stepping method is also called Chiba's method. After the Chiba's researches, the time-stepping method has been used for many studies.

The time-stepping method uses following relation:

$$\boldsymbol{q}'(t + \Delta t) = \exp(\boldsymbol{A}\Delta t)\boldsymbol{q}'(t) \tag{2.22}$$

This equation can be obtained by integrating the Eq. 2.5 in time. Here, we introduce the trans-

formed matrix B:

$$\boldsymbol{B} = \exp(\boldsymbol{A}\Delta t) \tag{2.23}$$

where Δt is an adjustable parameter. When the eigenvalues and eigenvectors of the matrices $\boldsymbol{A}$ and $\boldsymbol{B}$ are denoted by the subscripts A and B, the following relations are established:

$$\lambda_B = \exp(\lambda_A \Delta t) \tag{2.24}$$

$$\hat{\boldsymbol{q}}_B = \hat{\boldsymbol{q}}_A \tag{2.25}$$

The Eq. 2.24 can be written in the following form:

$$\lambda_A = \frac{\log|\lambda_B| + i\mathrm{Arg}\,(\lambda_B) + i2n\pi}{\Delta t}, \quad n = 0, \ \pm 1, \ \pm 2, \ \cdots \tag{2.26}$$

where $\mathrm{Arg}\,(\lambda_B)$ denotes the principal value of argument of λ_B, defined to lie in the interval $(-\pi, \ \pi]$. Note that this spectral transformation method does not take account of multiple eigenvalues.

The relation between the stability and the transformed eigenvalue λ_B is,

$$\begin{aligned} |\lambda_B| &> 1 \quad \text{unstable} \\ |\lambda_B| &= 1 \quad \text{neutrally stable} \\ |\lambda_B| &< 1 \quad \text{stable} \end{aligned} \tag{2.27}$$

Therefore, the absolute values of the eigenvalues of unstable modes become large in the transformed matrix $\boldsymbol{B}$. An example of the spectral transformation performed by the time-stepping method is shown in Fig. 2.1.

Calculation of $\boldsymbol{B}\boldsymbol{\zeta}_k$

The Arnoldi method which incorporates the time-stepping method is a matrix-free method, namely, this method does not need to calculate and store the matrices $\boldsymbol{A}$ and $\boldsymbol{B}$. Only the matrix-vector product $\boldsymbol{B}\boldsymbol{\zeta}_k$ for Eqs. 2.16 and 2.17 is needed. The advantage of the matrix-free method is the decrease in the required memory to store the matrix. Here, the method for calculations of $\boldsymbol{B}\boldsymbol{\zeta}_k$ is explained.

If we substitute $\boldsymbol{\zeta}_k$ to $\boldsymbol{q}'(t)$ of Eq. 2.22, $\boldsymbol{B}\boldsymbol{\zeta}_k$ can be calculated as,

$$\boldsymbol{B}\boldsymbol{\zeta}_k = \boldsymbol{q}'(t + \Delta t) \tag{2.28}$$

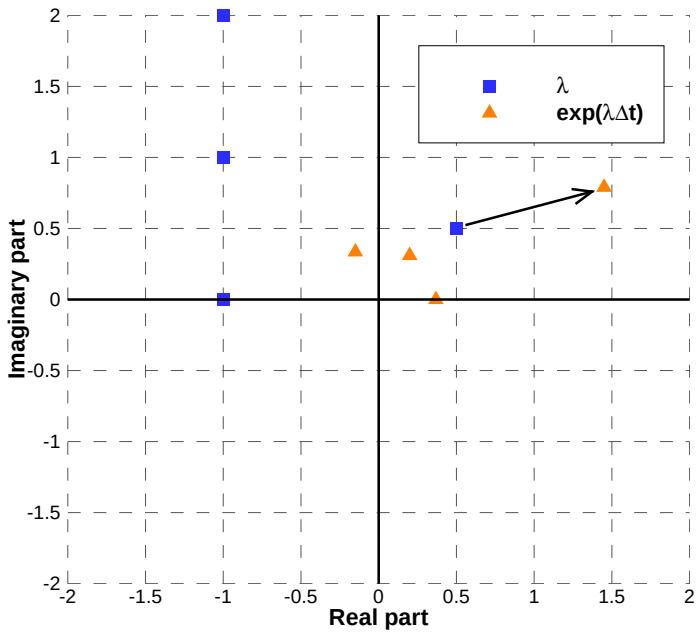

Figure 2.1: Example of the spectral transformation performed by the time-stepping method. Δt is set to 1.

where $\boldsymbol{q}'(t + \Delta t)$ is calculated by integrating the linearized governing equation Eq. 2.5 in time, with the initial condition $\boldsymbol{q}'(t) = \boldsymbol{\zeta}_k$.

Alternatively, the following equation can be also used,

$$\boldsymbol{B}\boldsymbol{\zeta}_k = \frac{\boldsymbol{q}(t + \Delta t) - \bar{\boldsymbol{q}}}{\varepsilon} \tag{2.29}$$

where $\boldsymbol{q}(t + \Delta t)$ is calculated by integrating the governing equation Eq. 2.1 with the initial condition $\boldsymbol{q}(t) = \bar{\boldsymbol{q}} + \varepsilon\boldsymbol{\zeta}_k$. Here, ε is a small positive constant for adjusting the magnitude of the $\boldsymbol{\zeta}_k$ which works as a perturbation. Because the $\boldsymbol{q}(t + \Delta t)$ includes the effect of nonlinear terms of the full governing equations, the approximation by Eq. 2.29 is not accurate when the amplitude of the perturbation is large.

The time-integration for performing this method can be conducted by a conventional time-integration method of CFD, which is explained in Chapter 3.

2.3.2 Shift-invert method

The shift-invert method is often used with Arnoldi method for an eigenvalue problem, not limited to the global linear stability analysis. This method is often called the shift-invert Arnoldi

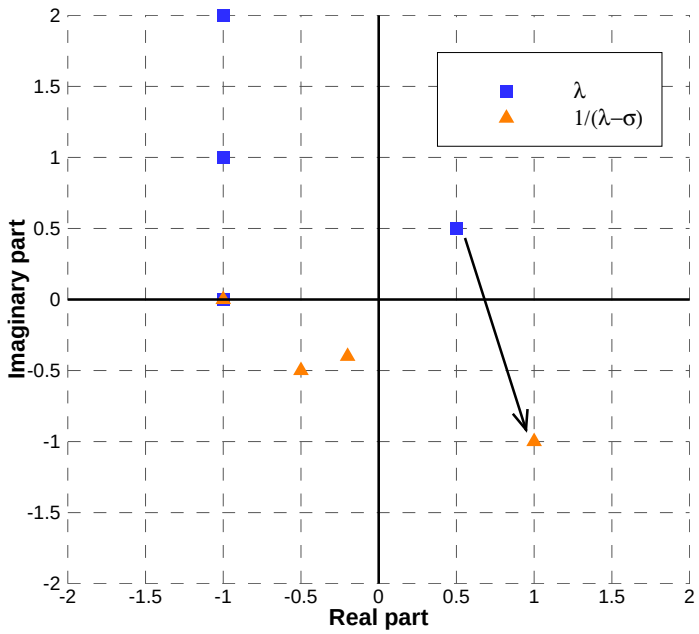

Figure 2.2: Example of the spectral transformation performed by the shift-invert method. s is set to 0.

method. The shift-invert method uses a following matrix:

$$\boldsymbol{B} = (\boldsymbol{A} - s\boldsymbol{I})^{-1} \tag{2.30}$$

where, s is a shift parameter and is a complex number. The eigenvalues and eigenvectors of the matrix $\boldsymbol{A}$ and the transformed matrix $\boldsymbol{B}$ are connected by the following equations:

$$\lambda_B = \frac{1}{\lambda_A - s} \tag{2.31}$$

$$\hat{\boldsymbol{q}}_B = \hat{\boldsymbol{q}}_A \tag{2.32}$$

Therefore, when λ_A is near the s, the absolute of λ_B takes a large value. An example of the spectral transformation performed by the shift-invert method is shown in Fig. 2.2.

Calculation of $\boldsymbol{B}\boldsymbol{\zeta}_k$

$\boldsymbol{B}\boldsymbol{\zeta}_k$ can be calculated by the following procedures. When a vector $\boldsymbol{y}$ is defined as

$$\boldsymbol{B}\boldsymbol{\zeta}_k = \boldsymbol{y} \tag{2.33}$$

the following equation is derived.

$$(\boldsymbol{A} - s\boldsymbol{I})\boldsymbol{y} = \boldsymbol{\zeta}_k \tag{2.34}$$

This is a system of linear equations with the large matrix A. In order to obtain the vector $\boldsymbol{y}$, iterative methods such as Bi-CGSTAB[30] and GMRES[31] method or direct methods for a sparse matrix can be used (if A is a sparse matrix). In this study, a direct method, the PARDISO solver,[32] is used.

In order to solve Eq. 2.34 by direct methods, or iterative methods with some preconditioning technique, the elements of matrix $\boldsymbol{A}$ denoted $a_{i,j}$ are required. Therefore, this method is not a matrix-free method unlike the time-stepping method, namely, this method is a matrix-forming method. The elements $a_{i,j}$ can be approximated as follows:[28]

$$a_{i,j} = \frac{f_i\left(\overline{\boldsymbol{q}} + \varepsilon_j \boldsymbol{e}_j\right) - f_i\left(\overline{\boldsymbol{q}}\right)}{\varepsilon_j} \tag{2.35}$$

$$\varepsilon_j = \varepsilon_1 q_j + \varepsilon_2 \tag{2.36}$$

where $\boldsymbol{e}_j$ is a vector which has all zeros and the value 1 in the j-th location. ε_1 and ε_2 are the small positive parameters and set to $\varepsilon_1 = 10^{-4}$ and $\varepsilon_2 = 10^{-6}$ in Chapter 4.

2.4 Flowchart of global linear stability analysis

In Fig. 2.3, the flowchart of the global linear stability analysis is shown. The calculation of $\boldsymbol{B}\boldsymbol{\zeta}_k$ has highest computational time cost in this flowchart, because we must perform time integrations or solve the large system of linear equations in the each loop of the Arnoldi iterations.

This method needs to conduct numerical fluid simulations (CFD) in order to obtain the basic state $\overline{\boldsymbol{q}}$ and the term $\boldsymbol{B}\boldsymbol{\zeta}_k$ as explained above. In the next chapter, the numerical methods of CFD are explained in detail.

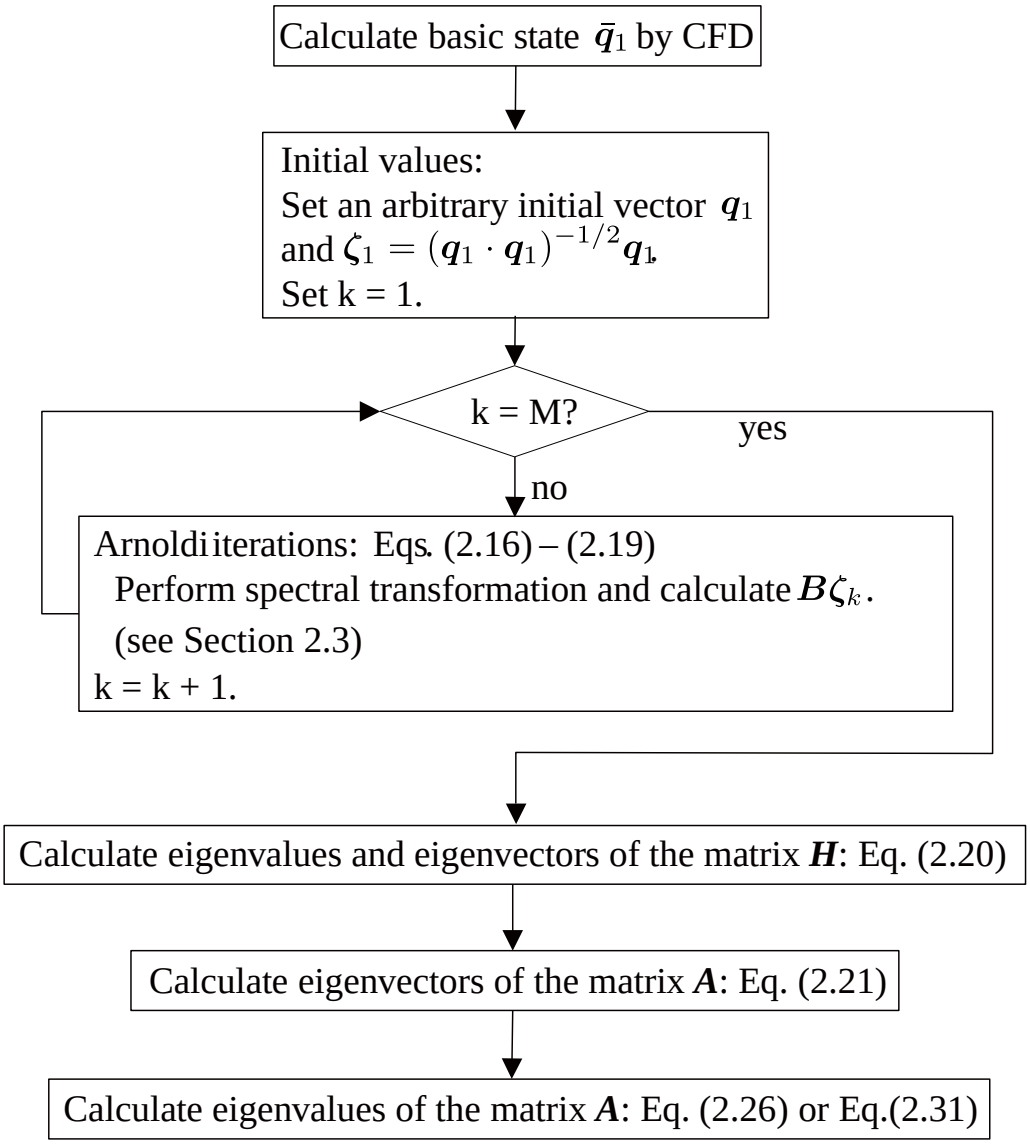

Figure 2.3: Flowchart of global linear stability analysis.

3 Numerical Methods for Fluid Dynamics

3.1 Gorverning equations

3.1.1 Compressible Navier-Stokes equations

Compressible Navier-Stokes equations in Cartesian coordinate (x, y)

In Chapters 4 and 5, the two-dimensional full Navier-Stokes equations are solved in order to obtain basic states $\bar{\boldsymbol{q}}$ of the compressible viscous flows. These equations in Cartesian coordinates (x, y) are as follows:

$$\frac{\partial \boldsymbol{Q}}{\partial t} + \frac{\partial \boldsymbol{E}}{\partial x} + \frac{\partial \boldsymbol{F}}{\partial y} = \frac{\partial \boldsymbol{E}_v}{\partial x} + \frac{\partial \boldsymbol{F}_v}{\partial y} \tag{3.1}$$

$$\boldsymbol{Q} = \begin{bmatrix} \rho \\ \rho u \\ \rho v \\ e \end{bmatrix} \tag{3.2}$$

$$\boldsymbol{E} = \begin{bmatrix} \rho u \\ \rho u^2 + p \\ \rho u v \\ (e + p)u \end{bmatrix}, \quad \boldsymbol{F} = \begin{bmatrix} \rho v \\ \rho v u \\ \rho v^2 + p \\ (e + p)v \end{bmatrix} \tag{3.3}$$

$$\boldsymbol{E}_v = \begin{bmatrix} 0 \\ \tau_{xx} \\ \tau_{xy} \\ \beta_x \end{bmatrix}, \quad \boldsymbol{F}_v = \begin{bmatrix} 0 \\ \tau_{yx} \\ \tau_{yy} \\ \beta_y \end{bmatrix} \tag{3.4}$$

$$\beta_x = \tau_{xx} u + \tau_{xy} v + \kappa \frac{\partial T}{\partial x}$$
$$\beta_y = \tau_{yx} u + \tau_{yy} v + \kappa \frac{\partial T}{\partial y}$$

where, $\boldsymbol{Q}$ is the conservative variables, $\boldsymbol{E}$ and $\boldsymbol{F}$ are the inviscid terms, and $\boldsymbol{E}_v$ and $\boldsymbol{F}_v$ are the viscous terms. u and v are the velocity in x- and y-directions, respectively. ρ is the density, e is the total energy per unit volume, p is the pressure, T is the temperature, and t is the time.

Pressure p is calculated as follows:

$$p = (\gamma - 1)\left[e - \frac{1}{2}\rho(u^2 + v^2)\right] \tag{3.5}$$

where γ is the ratio of specific heats and set to 1.4.

The equation of state of the perfect gas is as follows:

$$p = \rho RT \tag{3.6}$$

where R is the gas constant.

τ_{ij} is the viscous stress tensor and can be calculated as follows:

$$\begin{aligned}
\underline{\boldsymbol{\tau}} &= \begin{bmatrix} \tau_{xx} & \tau_{xy} \\ \tau_{yx} & \tau_{yy} \end{bmatrix} \\
&= \mu 2\underline{\boldsymbol{S}} + \left(\beta - \frac{2}{3}\mu\right)(\boldsymbol{\nabla}\cdot\boldsymbol{u})\underline{\boldsymbol{\delta}} \\
&= \begin{bmatrix} \frac{2}{3}\mu\left(2\frac{\partial u}{\partial x} - \frac{\partial v}{\partial y}\right) & \mu\left(\frac{\partial u}{\partial x} + \frac{\partial v}{\partial y}\right) \\ \mu\left(\frac{\partial u}{\partial x} + \frac{\partial v}{\partial y}\right) & \frac{2}{3}\mu\left(2\frac{\partial v}{\partial y} - \frac{\partial u}{\partial x}\right) \end{bmatrix}
\end{aligned} \tag{3.7}$$

where μ is the dynamic viscosity, β is the bulk viscosity (set to 0), $\underline{\boldsymbol{\delta}}$ is the Kronecker delta, and $\underline{\boldsymbol{S}}$ is the strain rate tensor defined by $\underline{\boldsymbol{S}} = \frac{1}{2}\left(\boldsymbol{\nabla u} + (\boldsymbol{\nabla u})^T\right)$.

κ is the thermal conductivity,

$$\kappa = \frac{\gamma R}{\gamma - 1}\frac{\mu}{Pr} \tag{3.8}$$

where Pr denotes the Prandtl number and is set to 0.72 in this study.

Nondimensionalization

Nondimensionalization of the equations is based on reference quantities U_∞, ρ_∞, p_∞, T_∞, μ_∞ and a characteristic physical length L.

$$\begin{aligned}
x^* &= \frac{x}{L}, \quad y^* = \frac{y}{L}, \quad u^* = \frac{u}{U_\infty}, \quad v^* = \frac{v}{U_\infty}, \quad t^* = \frac{t}{L/U_\infty} \\
\rho^* &= \frac{\rho}{\rho_\infty}, \quad p^* = \frac{p}{\rho_\infty U_\infty^2}, \quad T^* = \frac{T}{T_\infty}, \quad \mu^* = \frac{\mu}{\mu_\infty}
\end{aligned}$$

where superscript asterisk * denotes nondimensional variables.

By using above nondimensional vaiables, the equation 3.1 is written as the following form:

$$\frac{\partial \boldsymbol{Q}^*}{\partial t^*} + \frac{\partial \boldsymbol{E}^*}{\partial x^*} + \frac{\partial \boldsymbol{F}^*}{\partial y^*} = \frac{1}{Re}\left[\frac{\partial \boldsymbol{E}_v^*}{\partial x^*} + \frac{\partial \boldsymbol{F}_v^*}{\partial y^*}\right] \tag{3.9}$$

where Re is the Reynolds number and defined as follows:

$$Re = \frac{\rho_\infty U_\infty L}{\mu_\infty} \tag{3.10}$$

The components of the vectors $\boldsymbol{Q}^*$, $\boldsymbol{E}^*$, $\boldsymbol{F}^*$, $\boldsymbol{E}_v^*$, and $\boldsymbol{F}_v^*$ are same as those of Eq. 3.1 which are replaced by nondimensional variables.

The nondimensionalized equation of the state of the perfect gas is as follows:

$$p^* = \rho^* R^* T^* \tag{3.11}$$

where,

$$R^* = \frac{1}{\gamma Ma^2} \tag{3.12}$$

Ma is the Mach number, which is defined by the reference velocity U_∞ and the speed of sound c_∞:

$$Ma = \frac{U_\infty}{c_\infty} \tag{3.13}$$

A temperature dependability of the viscous coefficient μ^* can be calculated by the Sutherland's formula:

$$\mu^* = C_1^* \frac{(T^*)^{\frac{3}{2}}}{T^* + C_2^*} \tag{3.14}$$

$$C_1^* = \frac{1.458 \times 10^{-6}}{\mu_\infty}\sqrt{T_\infty}, \quad C_2^* = \frac{110.4}{T_\infty}$$

In this study, all the simulations are performed by using the nondimensional variables. Therefore, hereinafter in this paper, we omit the superscript asterisk * for brevity.

Compressible Navier-Stokes equations in curvilinear coordinates (ξ, η)

The Eq. 3.9 can be transformed from Cartesian coordinates (x, y) to curvilinear coordinates (ξ, η) where,

$$\xi = \xi(x, y)$$

$$\eta = \eta(x, y)$$

By applying the chain rule, the Eq 3.9 takes the following form:

$$\frac{\partial \hat{\boldsymbol{Q}}}{\partial t} + \frac{\partial \hat{\boldsymbol{E}}}{\partial \xi} + \frac{\partial \hat{\boldsymbol{F}}}{\partial \eta} = \frac{1}{Re}\left[\frac{\partial \hat{\boldsymbol{E}}_v}{\partial \xi} + \frac{\partial \hat{\boldsymbol{F}}_v}{\partial \eta}\right] \tag{3.15}$$

where,

$$\hat{\boldsymbol{Q}} = \frac{\boldsymbol{Q}}{J} = \frac{1}{J}\begin{bmatrix} \rho \\ \rho u \\ \rho v \\ e \end{bmatrix} \tag{3.16}$$

$$\hat{\boldsymbol{E}} = \frac{\xi_x}{J}\boldsymbol{E} + \frac{\xi_y}{J}\boldsymbol{F} = \frac{1}{J}\begin{bmatrix} \rho U \\ \rho u U + \xi_x p \\ \rho v U + \xi_y p \\ (e+p)U \end{bmatrix}, \quad \hat{\boldsymbol{F}} = \frac{\eta_x}{J}\boldsymbol{E} + \frac{\eta_y}{J}\boldsymbol{F} = \frac{1}{J}\begin{bmatrix} \rho V \\ \rho u V + \eta_x p \\ \rho v V + \eta_y p \\ (e+p)V \end{bmatrix} \tag{3.17}$$

$$\hat{\boldsymbol{E}}_v = \frac{\xi_x}{J}\boldsymbol{E}_v + \frac{\xi_y}{J}\boldsymbol{F}_v = \frac{1}{J}\begin{bmatrix} 0 \\ \xi_x\tau_{xx} + \xi_y\tau_{xy} \\ \xi_x\tau_{yx} + \xi_y\tau_{yy} \\ \xi_x\beta_x + \xi_y\beta_y \end{bmatrix}, \quad \hat{\boldsymbol{F}}_v = \frac{\eta_x}{J}\boldsymbol{E}_v + \frac{\eta_y}{J}\boldsymbol{F}_v = \frac{1}{J}\begin{bmatrix} 0 \\ \eta_x\tau_{xx} + \eta_y\tau_{xy} \\ \eta_x\tau_{yx} + \eta_y\tau_{yy} \\ \eta_x\beta_x + \eta_y\beta_y \end{bmatrix} \tag{3.18}$$

The subscripts x and y denote the partial derivatives with respect to x and y, respectively. The metrics $\xi_x, \xi_y, \eta_x, \eta_y$, and the metric Jacobian J are calculated by following relations:

$$\xi_x = Jy_\eta, \quad \xi_y = -Jx_\eta$$

$$\eta_x = -Jy_\xi, \quad \eta_y = Jx_\xi \tag{3.19}$$

$$J = 1/\begin{vmatrix} x_\xi & x_\eta \\ y_\xi & y_\eta \end{vmatrix} \tag{3.20}$$

where, subscripts ξ and η denote the partial derivatives with respect to ξ and η, respectively. For the calculation of the derivatives x_ξ, x_η, y_ξ, and y_η, the second-order central difference method is used when the SLAU scheme is used for the calculation of inviscid terms, and the compact difference scheme is used when the compact difference scheme is also used for the inviscid terms. The calculation of the inviscid terms is explained in Section 3.2.

3.1.2 Linearized compressible Navier-Stokes equations

In Chapters 4 and 5, the linearized compressible Navier-Stokes equations are solved in order to develop the perturbations $\boldsymbol{q}'$ superimposed on the basic states $\bar{\boldsymbol{q}}$ in time.

The linearized compressible Navier-Stokes equations can be derived by substituting $\boldsymbol{q} = \bar{\boldsymbol{q}} + \boldsymbol{q}'$ into Eq. 3.1, canceling the terms of $\bar{\boldsymbol{q}}$, and neglecting second or higher order terms of $\boldsymbol{q}'$,

$$\frac{\partial \boldsymbol{Q}'}{\partial t} + \frac{\partial \boldsymbol{E}'}{\partial x} + \frac{\partial \boldsymbol{F}'}{\partial y} = \frac{\partial \boldsymbol{E}'_v}{\partial x} + \frac{\partial \boldsymbol{F}'_v}{\partial y} \tag{3.21}$$

$$\boldsymbol{Q}' = \begin{bmatrix} \rho' \\ \bar{\rho}u' + \rho'\bar{u} \\ \bar{\rho}v' + \rho'\bar{v} \\ \rho'(C_v\bar{T} + 0.5(\bar{u}^2 + \bar{v}^2)) + \bar{\rho}(C_vT' + \bar{u}u' + \bar{v}v') \end{bmatrix} \tag{3.22}$$

$$\begin{aligned} \boldsymbol{E}' &= \begin{bmatrix} \bar{\rho}u' + \rho'\bar{u} \\ \rho'\bar{u}^2 + 2\overline{\rho u}u' + p' \\ \overline{\rho u}v' + \bar{\rho}u'\bar{v} + \rho'\overline{uv} \\ (\bar{\rho}u' + \rho'\bar{u})(C_p\bar{T} + 0.5(\bar{u}^2 + \bar{v}^2)) + \overline{\rho u}(C_pT' + \bar{u}u' + \bar{v}v') \end{bmatrix}, \\ \boldsymbol{F}' &= \begin{bmatrix} \bar{\rho}v' + \rho'\bar{v} \\ \overline{\rho u}v' + \bar{\rho}u'\bar{v} + \rho'\overline{uv} \\ \rho'\bar{v}^2 + 2\overline{\rho v}v' + p' \\ (\bar{\rho}v' + \rho'\bar{v})(C_p\bar{T} + 0.5(\bar{u}^2 + \bar{v}^2)) + \overline{\rho v}(C_pT' + \bar{u}u' + \bar{v}v') \end{bmatrix} \end{aligned} \tag{3.23}$$

$$\begin{aligned} \boldsymbol{E}'_v &= \begin{bmatrix} 0 \\ \tau'_{xx} \\ \tau'_{xy} \\ u'\bar{\tau}_{xx} + v'\bar{\tau}_{xy} + \bar{u}\tau'_{xx} + \bar{v}\tau'_{xy} + \bar{\kappa}\frac{\partial T'}{\partial x} + \kappa'\frac{\partial \bar{T}}{\partial x} \end{bmatrix}, \\ \boldsymbol{F}'_v &= \begin{bmatrix} 0 \\ \tau'_{xy} \\ \tau'_{yy} \\ u'\bar{\tau}_{xy} + v'\bar{\tau}_{yy} + \bar{u}\tau'_{xy} + \bar{v}\tau'_{yy} + \bar{\kappa}\frac{\partial T'}{\partial y} + \kappa'\frac{\partial \bar{T}}{\partial y} \end{bmatrix} \end{aligned} \tag{3.24}$$

where,

$$p' = \rho' R\bar{T} + \bar{\rho}RT' \tag{3.25}$$

$$\begin{aligned} \tau'_{xy} &= \tau'_{yx} = \bar{\mu}\left(\frac{\partial u'}{\partial y} + \frac{\partial v'}{\partial x}\right) + \mu'\left(\frac{\partial \bar{u}}{\partial y} + \frac{\partial \bar{v}}{\partial x}\right), \\ \tau'_{xx} &= \frac{2}{3}\bar{\mu}\left(2\frac{\partial u'}{\partial x} - \frac{\partial v'}{\partial y}\right) + \frac{2}{3}\mu'\left(2\frac{\partial \bar{u}}{\partial x} - \frac{\partial \bar{v}}{\partial y}\right), \\ \tau'_{yy} &= \frac{2}{3}\bar{\mu}\left(2\frac{\partial v'}{\partial y} - \frac{\partial u'}{\partial x}\right) + \frac{2}{3}\mu'\left(2\frac{\partial \bar{v}}{\partial y} - \frac{\partial \bar{u}}{\partial x}\right) \end{aligned} \tag{3.26}$$

$$\bar{\kappa} = \frac{C_p\bar{\mu}}{Pr}, \quad \kappa' = \frac{C_p\mu'}{Pr} \tag{3.27}$$

and, C_p and C_v are the specific heat at constant pressure and constant volume, respectively.

$$C_p = \frac{\gamma R}{\gamma - 1}, \quad C_v = \frac{R}{\gamma - 1} \tag{3.28}$$

The nondimensionalization and the coordinate transformation can be made by the same manner as Section 3.1.1.

3.2 Discretization of the governing equations

3.2.1 Discretization of inviscid terms

Compact difference scheme

In Chapters 4 and 5, the six-order compact difference scheme[33] is used for the evaluation of spatial derivatives for convective terms, viscous terms, metrics and the Jacobian J, in order to solve the Eqs. 3.1 and 3.21. For any scalar quantity ϕ, the spatial derivative $\dfrac{\partial \phi}{\partial \xi}$ is obtained in the transformed plane by the following tridiagonal system:

$$\frac{1}{3}\left(\frac{\partial \phi}{\partial \xi}\right)_{i-1} + \left(\frac{\partial \phi}{\partial \xi}\right)_{i} + \frac{1}{3}\left(\frac{\partial \phi}{\partial \xi}\right)_{i+1} = \frac{1}{9}\frac{\phi_{i+2} - \phi_{i-2}}{4\Delta\xi} + \frac{14}{9}\frac{\phi_{i+1} - \phi_{i-1}}{2\Delta\xi} \tag{3.29}$$

At the boundary points $i = 1$ and $i = 2$, following formulas[34] which retain the tridiagonal form are used,

$$\left(\frac{\partial \phi}{\partial \xi}\right)_{1} + 3\left(\frac{\partial \phi}{\partial \xi}\right)_{2} = \frac{1}{\Delta\xi}\left(-\frac{17}{6}\phi_1 + \frac{3}{2}\phi_2 + \frac{3}{2}\phi_3 - \frac{1}{6}\phi_4\right) \tag{3.30}$$

$$\frac{1}{4}\left(\frac{\partial \phi}{\partial \xi}\right)_{1} + \left(\frac{\partial \phi}{\partial \xi}\right)_{2} + \frac{1}{4}\left(\frac{\partial \phi}{\partial \xi}\right)_{3} = \frac{1}{\Delta\xi}\left(-\frac{3}{4}\phi_1\right) \tag{3.31}$$

These are the fourth-order formulas. The formulas at the boundary points $i = i_{max}$ and $i = i_{max}-1$ are similar.

In addition to the compact difference scheme, the filtering procedure described below is performed because the compact difference scheme is susceptible to numerical instabilities.

Filtering scheme

The eighth-order low-pass spatial filtering scheme[34] is applied with the compact difference scheme. In this scheme, the following tridiagonal system is solved:

$$\alpha_f \hat{\phi}_{i-1} + \hat{\phi}_i + \alpha_f \hat{\phi}_{i+1} = \sum_{n=0}^{4} \frac{a_n}{2}(\phi_{i+n} + \phi_{i-n}) \tag{3.32}$$

where ϕ is the solution vector and $\hat{\phi}$ is the filtered value. The α_f is an adjustable parameter which satiesfies the inequality $-0.5 < \alpha_f \leq 0.5$. The large value of α_f corresponds to a less dissipative filter. Visbal and Gaitonde[35] suggested the values of α_f between 0.3 and 0.5. The coefficients of this equation are shown in Table 3.1. Moreover, at near boundary point $i = 2$ and $i = 3$, a following formula is used:

$$\alpha_f \hat{\phi}_{i-1} + \hat{\phi}_i + \alpha_f \hat{\phi}_{i+1} = \sum_{n=1}^{7} a_{n,i}\phi_n \tag{3.33}$$

These coefficients a_n are shown in Table 3.2. The coefficients of near boundary points $i \leq 4$ corresponds to the sixth-order scheme. The coefficients at the points $i \geq i_{max} - 3$ are similar.

Table 3.1: Coefficients for the filtering formula Eq. 3.32.

Points	a_0	a_1	a_2	a_3	a_4
$i = 4$	$\frac{11 + 10\alpha_f}{16}$	$\frac{15 + 34\alpha_f}{32}$	$\frac{-3 + 6\alpha_f}{16}$	$\frac{1 - 2\alpha_f}{32}$	0
$5 \leq i \leq i_{max} - 4$	$\frac{93 + 70\alpha_f}{128}$	$\frac{7 + 18\alpha_f}{16}$	$\frac{-7 + 14\alpha_f}{32}$	$\frac{1 - 2\alpha_f}{16}$	$\frac{-1 + 2\alpha_f}{128}$

Table 3.2: Coefficients for the filtering formula Eq. 3.33.

Points	$a_{1,i}$	$a_{2,i}$	$a_{3,i}$	$a_{4,i}$	$a_{5,i}$	$a_{6,i}$	$a_{7,i}$
$i = 2$	$\frac{1 + 62\alpha_f}{64}$	$\frac{29 + 6\alpha_f}{32}$	$\frac{15 + 34\alpha_f}{64}$	$\frac{-5 + 10\alpha_f}{16}$	$\frac{15 - 30\alpha_f}{64}$	$\frac{-3 + 6\alpha_f}{32}$	$\frac{1 - 2\alpha_f}{64}$
$i = 3$	$\frac{-1 + 2\alpha_f}{64}$	$\frac{3 + 26\alpha_f}{32}$	$\frac{49 + 30\alpha_f}{64}$	$\frac{5 + 6\alpha_f}{16}$	$\frac{-15 + 30\alpha_f}{64}$	$\frac{3 - 6\alpha_f}{32}$	$\frac{-1 + 2\alpha_f}{64}$

LAD (Localized Artificial Diffusivity) method

If a flowfield includes shock waves, a LAD method[36,37] with the compact difference scheme is useful for a shock-capturing. When the compact difference scheme described above is applied to the flowfiled including discontinuities, spurious oscillations occur. The LAD method suppresses such an oscillation by adding local artificial viscosities to the coefficients[38] in Eq. 3.1.

$$\mu = \mu_f + \mu_a, \quad \beta = \beta_f + \beta_a, \quad \kappa = \kappa_f + \kappa_a \tag{3.34}$$

where the subscripts f and a denote fluid and artificial coefficients. These coefficients μ_a, β_a and κ_a serve the subgrid-scale transport, shock wave capturing, and the contact surface capturing, respectively.

In this study, the artificial viscosities designed by Kawai and Lele[37] are used. For a two-dimensional simulation, these can be written as follows:

$$\mu_a = C_\mu \rho \overline{\left| \sum_{l=1}^{2} \frac{\partial^4 \mathcal{F}_\mu}{\partial \xi_l^4} \Delta_{l,\mu}^2 \right|} \tag{3.35}$$

$$\beta_a = C_\beta \rho f_{sw} \overline{\left| \sum_{l=1}^{2} \frac{\partial^4 \mathcal{F}_\beta}{\partial \xi_l^4} \Delta_{l,\beta}^2 \right|} \tag{3.36}$$

$$\kappa_a = C_\kappa \frac{\rho c}{T} \overline{\left| \sum_{l=1}^{2} \frac{\partial^4 \mathcal{F}_\kappa}{\partial \xi_l^4} \Delta_{l,\kappa} \right|} \tag{3.37}$$

where C_μ, C_β, and C_κ are dimensionless adjustable constants. $\mathcal{F}_\mu$, $\mathcal{F}_\beta$, and $\mathcal{F}_\kappa$ are functions for detecting unresolved subgrid-scale eddies, shock waves, and contact surfaces. f_{sw} is a switching function which removes unnecessary artificial viscosities in smooth regions (which do not include discontinuities). The ξ_l denotes ξ and η for $l = 1$ and 2. The $\Delta_{l,(\mu,\beta,\kappa)}$ is the grid spacing in the physical space.

The overbar denotes an approximate truncated-Gaussian filter.[39]

$$\begin{aligned} \bar{\phi}_i = \frac{3565}{10368}\phi_i + \frac{3091}{12960}(\phi_{i-1} + \phi_{i+1}) + \frac{1997}{25920}(\phi_{i-2} + \phi_{i+2}) \\ + \frac{149}{12960}(\phi_{i-3} + \phi_{i+3}) + \frac{107}{103680}(\phi_{i-4} + \phi_{i+4}) \end{aligned} \tag{3.38}$$

This filter is applied along each grid line (namely, ξ and η directions). At near boundary points, ϕ_i is mirrored across the boundary.[36]

The detector functions $\mathcal{F}_\mu$, $\mathcal{F}_\beta$, and $\mathcal{F}_\kappa$ can be chosen as follows:

$$\mathcal{F}_\mu = S \tag{3.39}$$

$$\mathcal{F}_\beta = \boldsymbol{\nabla} \cdot \boldsymbol{u} \tag{3.40}$$

$$\mathcal{F}_\kappa = C_v T = \frac{1}{\gamma - 1}\frac{p}{\rho} \tag{3.41}$$

where S is the strain rate of Eq. 3.7.

The switching function f_{sw} is as follows:

$$f_{sw} = H(-\boldsymbol{\nabla} \cdot \boldsymbol{u}) \times \frac{(\boldsymbol{\nabla} \cdot \boldsymbol{u})^2}{(\boldsymbol{\nabla} \cdot \boldsymbol{u})^2 + |\boldsymbol{\nabla} \times \boldsymbol{u}|^2 + \varepsilon} \tag{3.42}$$

This is the combination of the Ducros-type shock sensor[40] $\dfrac{(\boldsymbol{\nabla} \cdot \boldsymbol{u})^2}{(\boldsymbol{\nabla} \cdot \boldsymbol{u})^2 + |\boldsymbol{\nabla} \times \boldsymbol{u}|^2 + \varepsilon}$ and the detector function for negative dilatation. Here, H is the Heaviside function and $\varepsilon = 10^{-32}$ is a small positive constant.

In order to scale the artificial viscosity properly, $\Delta_{l,(\mu,\beta,\kappa)}$ is defined as follows[37] :

$$\Delta_{l,\mu} = |\boldsymbol{\Delta} x_l|, \quad \Delta_{l,\beta} = \left|\boldsymbol{\Delta} x_l \cdot \frac{\boldsymbol{\nabla}\rho}{|\boldsymbol{\nabla}\rho|}\right|, \quad \Delta_{l,\kappa} = \left|\boldsymbol{\Delta} x_l \cdot \frac{\boldsymbol{\nabla} T}{|\boldsymbol{\nabla} T|}\right| \tag{3.43}$$

where $\boldsymbol{\Delta} x_l = \left(\dfrac{x_{j+1} - x_{j-1}}{2}, \dfrac{y_{j+1} - y_{j-1}}{2}\right)$, and j is an index of the ξ_l direction.

In this study, C_μ is set to 0, because we ignore the effects of subgrid-scale eddies. Therefore, the equations in terms of μ_a are not used. The coefficients C_β and C_κ is set to 1.75 and 0.01, respectively.

SLAU scheme with MUSCL interpolation

In Chapter 4, SLAU (Simple Low-dissipation AUSM) scheme[41,42] is used for the calculation of inviscid terms. SLAU scheme is a type of the AUSM (Advection Upstream Splitting Method)[43] scheme.

The inviscid flux of the AUSM scheme can be written in the following form:

$$\boldsymbol{F}_{1/2} = \frac{\dot{m} + |\dot{m}|}{2}\boldsymbol{\Phi}^+ + \frac{\dot{m} - |\dot{m}|}{2}\boldsymbol{\Phi}^- + p_{1/2}\boldsymbol{N} \tag{3.44}$$

where,

$$\boldsymbol{\Phi} = \begin{bmatrix} 1 \\ u \\ v \\ h \end{bmatrix}, \quad \boldsymbol{N} = \begin{bmatrix} 0 \\ x_n \\ y_n \\ 0 \end{bmatrix} \tag{3.45}$$

$$h = \frac{e + p}{\rho} \tag{3.46}$$

(x_n, y_n) is a unit vector normal to a cell interface. $\dot{m}$ and $p_{1/2}$ are a mass flux and a pressure on a cell interface, respectively. Superscripts + and − denote the left and right values of the cell interface.

In the SLAU scheme, the pressure term $p_{1/2}$ in Eq. 3.44 is evaluated as follows:

$$p_{1/2} = \frac{p^+ + p^-}{2} + \frac{\beta^+ - \beta^-}{2}(p^+ - p^-) + (1 - \chi)(\beta^+ + \beta^- - 1)\frac{p^+ + p^-}{2} \tag{3.47}$$

where,

$$\beta^\pm = \begin{cases} \frac{1}{4}(2 \mp M^\pm)(M^\pm \pm 1)^2, & |M^\pm| < 1 \\ \frac{1}{2}(1 + sign(\pm M^\pm)), & otherwise \end{cases} \tag{3.48}$$

$$M^\pm = \frac{V_n^\pm}{\bar{c}} \tag{3.49}$$

$$V_n^\pm = u^\pm x_n + v^\pm y_n + w^\pm z_n \tag{3.50}$$

$$\chi = (1 - \hat{M})^2 \tag{3.51}$$

$$\hat{M} = min\left(1.0, \frac{1}{\bar{c}}\sqrt{\frac{V_n^{+2} + V_n^{-2}}{2}}\right) \tag{3.52}$$

$$\bar{c} = \frac{1}{2}(c^+ + c^-) \tag{3.53}$$

c is the speed of sound which can be calculated by the following equation:

$$c = \sqrt{\frac{\gamma p}{\rho}} \tag{3.54}$$

The mass flux $\dot{m}$ is evaluated as follows:

$$\dot{m} = \frac{1}{2}\left\{\rho^+(V_n^+ + |\bar{V}_n|^+) + \rho^-(V_n^- - |\bar{V}_n|^-) - \frac{\chi}{\bar{c}}(p^- - p^+)\right\} \tag{3.55}$$

where,

$$|\bar{V}_n|^\pm = (1 - g)|\bar{V}_n| + g|V_n|^\pm \tag{3.56}$$

$$g = -max\left(min(M^+, 0), -1\right) \cdot min\left(max(M^-, 0), 1\right) \tag{3.57}$$

$$|\bar{V}_n| = \frac{\rho^+|V_n|^+ + \rho^-|V_n|^-}{\rho^+ + \rho^-} \tag{3.58}$$

The MUSCL interpolation[44,45] is used for the evaluations of quantities on the left and right side of the cell interface, denoted superscripts + and − in above equations. Limiter functions

such as the van Albada limiter[46] is not used because the flowfield to be analyzed does not include any discontinuities. The third-order MUSCL interpolation is as follows:

$$(q^+)_{i+\frac{1}{2}} = \frac{2q_{i+1} + 5q_i - q_{i-1}}{6} \tag{3.59}$$

$$(q^-)_{i+\frac{1}{2}} = \frac{2q_i + 5q_{i+1} - q_{i+2}}{6} \tag{3.60}$$

After the inviscid flux $F_{1/2}$ is obtained by the above equations, the inviscid terms are finally calculated by the following equation:

$$\frac{\partial \boldsymbol{F}}{\partial \xi} = \frac{\boldsymbol{F}_{1/2} - \boldsymbol{F}_{-1/2}}{\Delta \xi} \tag{3.61}$$

3.2.2 Discretization of viscous terms

In this study, the viscous terms are calculated by twice difference operations. First, we calculate first derivatives ϕ_x and ϕ_y by the chain rule:

$$\begin{aligned} \phi_x &= \xi_x \phi_\xi + \eta_x \phi_\eta, \\ \phi_y &= \xi_y \phi_\xi + \eta_y \phi_\eta \end{aligned} \tag{3.62}$$

ϕ denotes a scalar quantity. All the derivatives of the right hand side of Eq. 3.62 are evaluated by the second-order central difference method when the SLAU scheme is used for the calculation of inviscid terms, and by the compact difference scheme when the compact difference scheme is used for the inviscid terms.

Secondly, second derivatives are evaluated in the same manner by using the first derivatives obtained in the first step.

3.2.3 Time integration

Third-order TVD Runge-Kutta scheme

In this study, all time integrations are performed by the third-order TVD Runge-Kutta scheme.[47] For brevity, we write a governing equation in the following form:

$$\frac{\partial \boldsymbol{Q}}{\partial t} = \boldsymbol{R}(\boldsymbol{Q})$$

$\boldsymbol{R}(\boldsymbol{Q})$ denotes the right hand side of the equation which is functions of variables $\boldsymbol{Q}$. Here, the third-order TVD Runge-Kutta scheme is given by the following steps:

$$\begin{aligned} \boldsymbol{Q}^{(1)} &= \boldsymbol{Q}^n + \Delta t \boldsymbol{R}(\boldsymbol{Q}^n) \\ \boldsymbol{Q}^{(2)} &= \frac{3}{4}\boldsymbol{Q}^n + \frac{1}{4}\boldsymbol{Q}^{(1)} + \frac{1}{4}\Delta t \boldsymbol{R}(\boldsymbol{Q}^{(1)}) \\ \boldsymbol{Q}^{n+1} &= \frac{1}{3}\boldsymbol{Q}^n + \frac{2}{3}\boldsymbol{Q}^{(2)} + \frac{2}{3}\Delta t \boldsymbol{R}(\boldsymbol{Q}^{(2)}) \end{aligned} \tag{3.63}$$

This is the calculation for the time developing of $\boldsymbol{Q}$ from the time-step n to $n + 1$.

4 High-Resolution and Matrix-Free Method for Global Linear Stability Analysis

4.1 Introduction

In this chapter, we propose a numerical method for the global linear stability analysis which has high-order spatial accuracy and needs low memory requirements.

First, two methods for the spectral transformation, the time-stepping method and the shift-invert method, are compared, and we show that the time-stepping method has the low memory requirement and is promising for future global linear stability analyses. Then, we propose the numerical method for the global linear stability analysis using the time-stepping method as the method for the spectral transformation and the compact difference scheme as the method for fluid simulations. Several results of this method are shown as validation results and examples of the global linear stability analysis. Moreover, influences of outflow boundary conditions on the global linear stability analysis are investigated. Finally, the applicability of the proposed method to flowfields including shock waves is examined.

Through this chapter, a two-dimensional flow past a circular cylinder is analyzed, because this flow has been investigated by many researchers[16, 18, 19, 48] and therefore has many available data. Details are described in the next section.

4.2 Two-dimensional flow past a circular cylinder

Figure 4.1 shows two-dimensional viscous flows past a circular cylinder. When the Reynolds number is small enough, this flowfield is a steady state and a twin-vortex is formed behind the cylinder. When the Reynolds number exceeds a certain number (the critical Reynolds number

Re_{cr}), this flowfield is an unsteady state and the twin-vortex separates from the cylinder surface (the Kármán vortex-street). Here, the Reynolds number of this flow is defined as follows:

$$Re = \frac{\rho_\infty u_\infty D}{\mu_\infty} \tag{4.1}$$

where subscript ∞ denotes freestream variables and D is a diameter of the circular cylinder.

The instability of this flow has been studied for several decades.[16, 18, 19, 48] The previous studies revealed that the critical Reynolds number is between 45.5 and 49. Moreover, few incompressible[18, 19] and compressible[16] global linear stability analyses were conducted and found the unstable mode which induces the Kármán vortex-street. In the following sections, we analyze this flow as the test problem for numerical methods of the global linear stability analysis.

4.3 Comparison of numerical methods for spectral transformation

In this section, two methods of the spectral transformation, the time-stepping method and the shift-invert method explained in Section 2.3, are compared. The characteristics of these methods are discussed.

4.3.1 Problem description and Numerical method

Flow condition and computational grid

A flow to be analyzed is the flow around the circular cylinder described above. The Mach number of the freestream is $Ma = 0.05$, and five cases of the Reynolds number between 45 and 55 are analyzed. A computational grid used in this calculation is shown in Fig. 4.2. The grid is a structured grid which consists of radial lines and concentric circles. In the step of calculating steady flows, the flow of only the half domain ($y \geq 0$) is solved with the symmetric condition as it is described later, whereas the entire domain is used for the global linear stability analysis. The number of grid points is 121×151 (azimuthal $\times$ radial directions) for the half domain ($y \geq 0$) and 241×151 for the entire domain. The minimum grid spacing is $\Delta_{min} = 0.005D$.

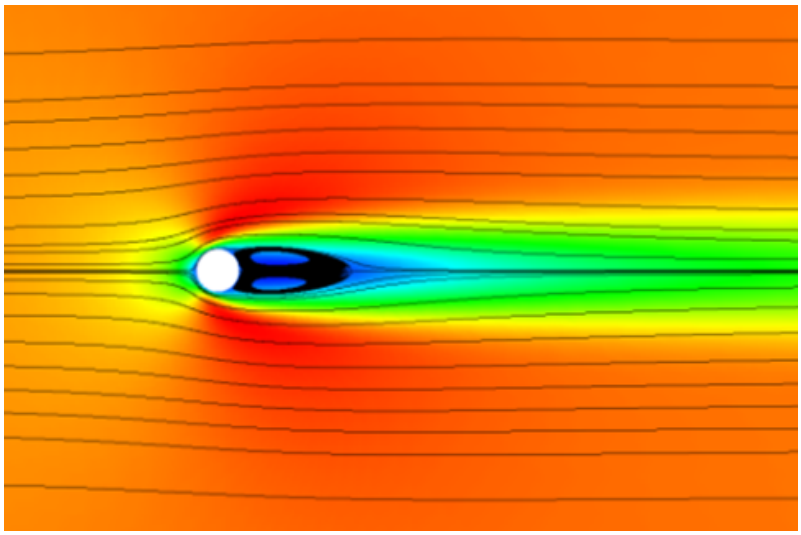

(a) Steady solution at $Re = 45$. Symmetric twin-vortex behind the cylinder is described by velocity u distribution and streamlines.

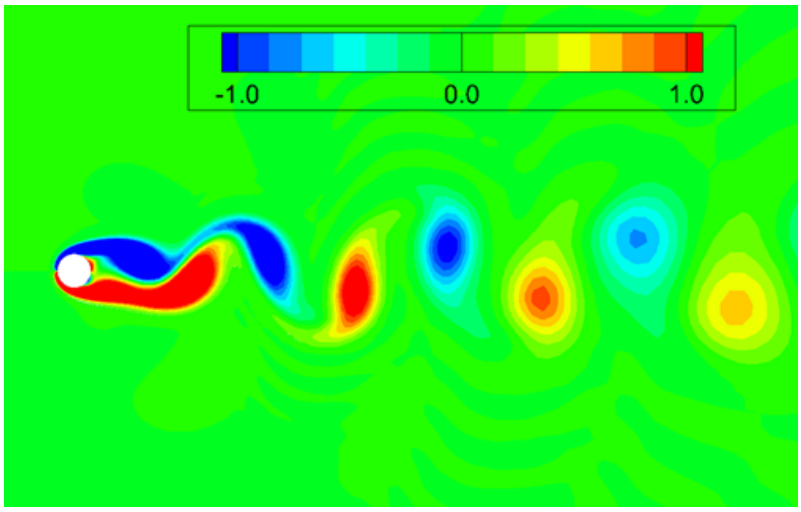

(b) Periodic solution at $Re = 120$. Kármán vortex-street behind the cylinder is described by vorticity distribution.

Figure 4.1: Steady and periodic solutions of the flow field behind a circular cylinder.

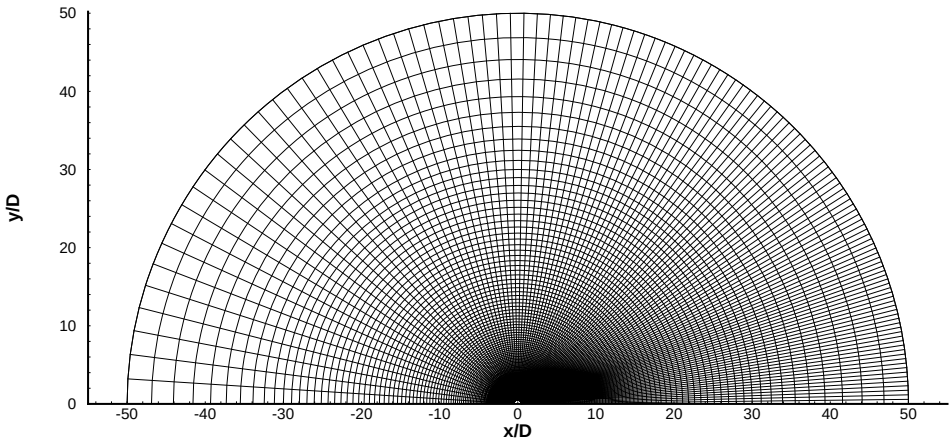

Figure 4.2: Computational grid.

Simulation of full compressible Navier-Stokes equations

The inviscid terms of the full compressible Navier-Stokes equations are calculated by the SLAU scheme with the third-order MUSCL interpolation, and the viscous terms are calculated by the second-order central difference method. The time-integration is performed by the third-order TVD Runge-Kutta scheme.

For the wall boundary (the cylinder surface), the no-slip condition and the adiabatic wall condition are used.

$$u = 0 \tag{4.2}$$

$$v = 0 \tag{4.3}$$

$$\frac{\partial p}{\partial n} = 0 \tag{4.4}$$

$$\frac{\partial T}{\partial n} = 0 \tag{4.5}$$

where n denotes a vector normal to the boundaries. The partial difference $\frac{\partial}{\partial n}$ is evaluated by the first-order one-sided finite difference.

For the far-field boundary conditions ($r = 50D,\ x > 0$), the pressure on the boundary is assumed to be the freestream value and the other variables are extrapolated by linear approxi-

mations.

$$p_{ib} = p_\infty \tag{4.6}$$

$$\rho_{ib} = 2\rho_{ib-1} - \rho_{ib-2} \tag{4.7}$$

$$(\rho u)_{ib} = 2(\rho u)_{ib-1} - (\rho u)_{ib-2} \tag{4.8}$$

$$(\rho v)_{ib} = 2(\rho v)_{ib-1} - (\rho v)_{ib-2} \tag{4.9}$$

where subscripts ib denotes the index of grid points on the outflow boundary.

On the symmetry plane ($y = 0$), the symmetry boundary conditions are used. By applying this condition, steady states can be obtained at the Reynolds number being higher than the critical value. This is because the sinuous mode is less stable than the varicose mode and the sinuous mode induces the Kármán vortex-street.[49]

Settings of time-stepping method and shift-invert method

In the process of the time-stepping method, the term $\boldsymbol{B\zeta}$ of the Arnoldi iterations is calculated by Eq. 2.29, which needs to solve the full compressible Navier-Stokes equation Eq. 3.1. The small constant ε in Eq. 2.29 is set to 0.01. By the preliminary calculations, we have confirmed that the constant ε between 0.001 and 0.1 do not affects the results. The parameter Δt is set to 1.0 and the number of iterations for Arnoldi iterations M is 250.

In the process of the shift-invert method, the shift parameter s is set to 0 because the transition of flows from the steady to the unsteady state occurs when a real part of an eigenvalue becomes positive. The number of iterations for the Arnoldi method M is set to 500. The difference of M of the time-stepping method and the shift-invert method is caused by the difference of convergence properties of these method.

The detailed explanation of the time-stepping method and the shift-invert methods are shown in Section 2.3.

4.3.2 Results and Discussions

Comparison of most unstable mode

Figure 4.3 shows the eigenvectors of the most unstable mode (in other words, the least stable mode) at $Re = 45$. As it will be described later, the Kármán vortex-street occurs when this mode

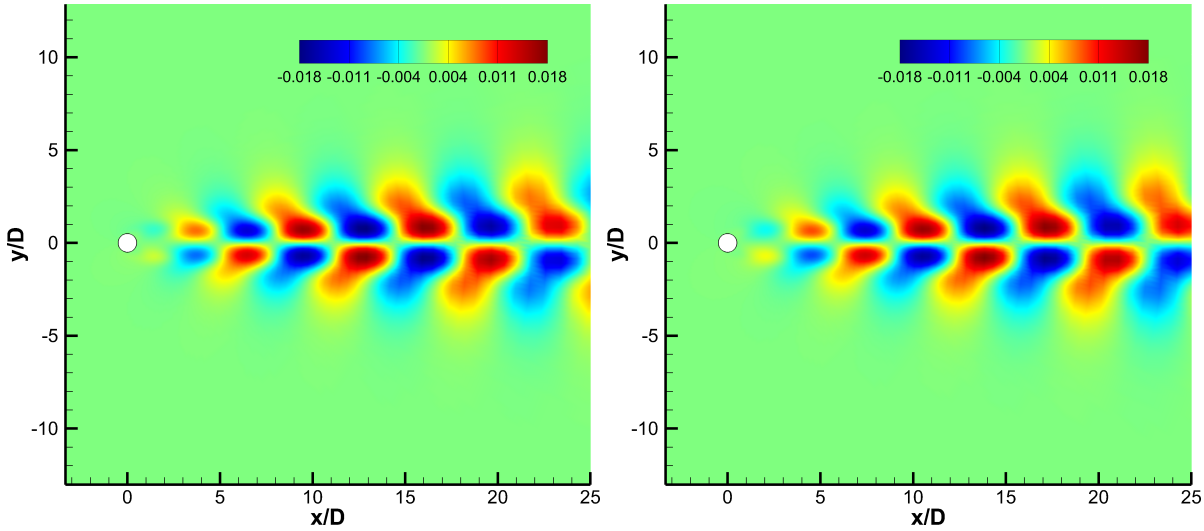

(a) Result of time-stepping method

(b) Result of shift-invert method

Figure 4.3: Eigenvectors of most unstable mode at $Re = 45$. Momentum in x-direction ρu is illustrated.

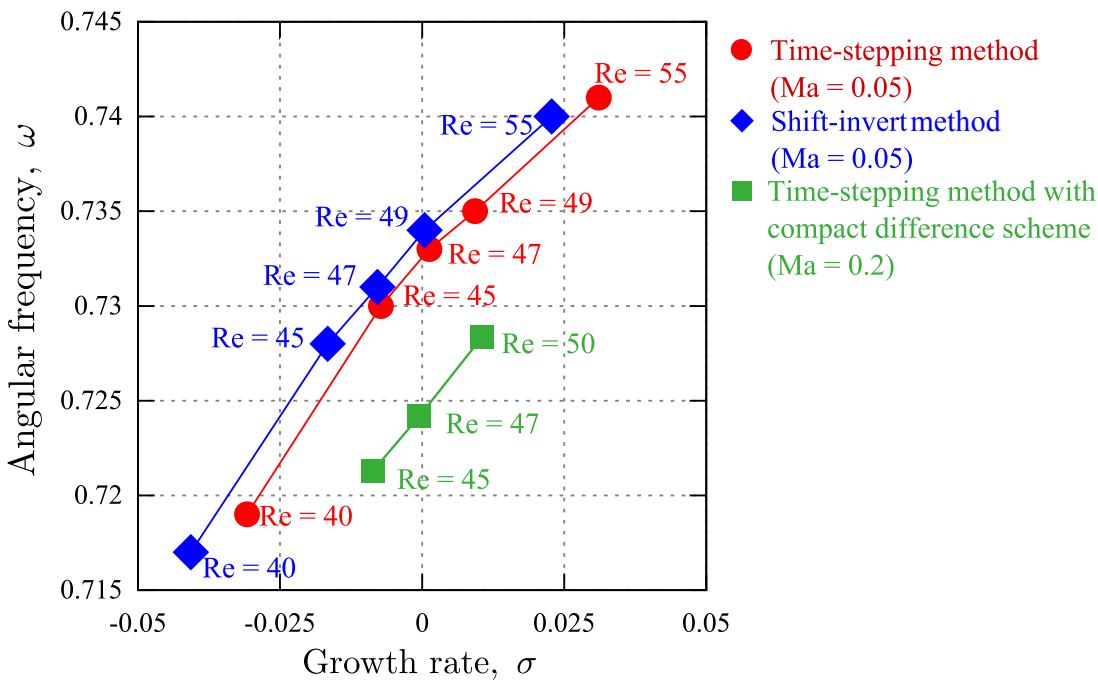

Figure 4.4: Change of the eigenvalues of the most unstable mode by Reynolds number.

Table 4.1: Critical Reynolds and Strouhal numbers obtained by previous studies.

	Re_{cr}	St_{cr}	Analysis method
Nishioka (1978)[48]	46	0.12	Experiment
Chiba (1997)[18, 19]	45.5	0.119	Numerical simulation (Incompressible)
Crouch (2007)[16]	47	0.116	Numerical simulation (Compressible, $Ma = 0.2$)
Present work	47, 49	0.117	Numerical simulation (Compressible, $Ma = 0.05$)

becomes unstable. The alternating distributions appeared in the wake of the circular cylinder. This distribution is in good agreement with the results of Crouch et al.[16] The change of the eigenvalue of the most unstable mode by the Reynolds number is shown in Fig. 4.4. (The result obtained by using the time-stepping method with the compact difference scheme shown in this figure will be referenced in the next section.) The results obtained by using the time-stepping method and the shift-invert method indicate that both the real part (the growth rate) and the imaginary part (the angular frequency) increase as the Reynolds number increases. The critical Reynolds number Re_{cr} can be estimated to 47 and 49 from the results of the time-stepping method and the shift-invert method, respectively. In both cases, the imaginary parts are similar values and the critical Strouhal number $St = \dfrac{\omega}{2\pi}$ is estimated to 0.117. It is inferred that the small difference of the critical Reynolds number, as well as the real part of eigenvalues, is caused by the numerical stability of the time integration which only used in the time-stepping method. The estimated critical Reynolds and Strouhal numbers of our results coincide with the previous numerical and experimental studies,[16, 18, 19, 48] as detailed in Table 4.1.

Consequently, we confirmed that both methods of the spectral transformation can reproduce the results of previous studies which are well validated, and the results of the time-stepping method and the shift-invert method are qualitatively same although the real parts of eigenvalues are a little different.

Aliasing problem of time-stepping method

The time-stepping method cannot determine the imaginary part of eigenvalues uniquely, because Eq. 2.24 has a multiple-value function, as following:

$$\lambda_A = \frac{\log|\lambda_B| + i\mathrm{Arg}(\lambda_B) + i2n\pi}{\Delta t}, \quad n = 0, \ \pm 1, \ \pm 2, \ \cdots \tag{4.10}$$

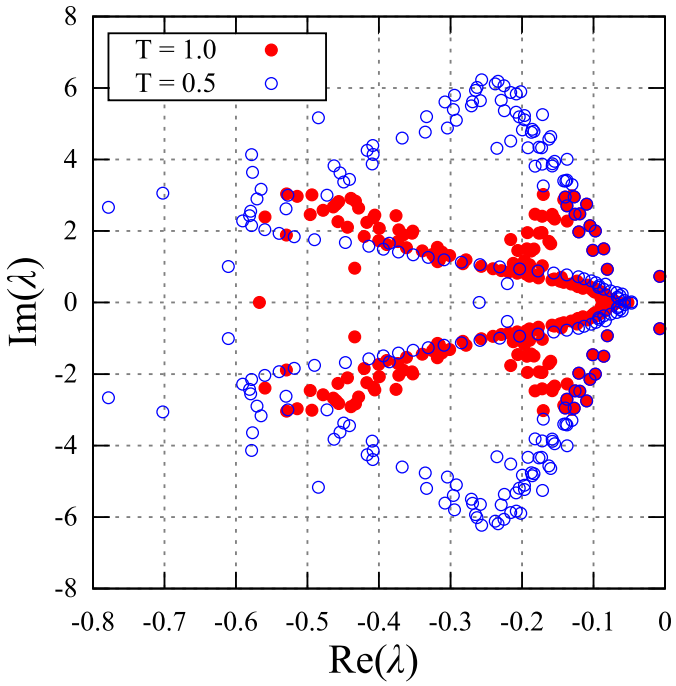

Figure 4.5: Aliasing phenomena due to Eq. 4.10. n is set to 0.

where $\mathrm{Arg}\,(\lambda_B)$ denotes the principal value of argument of λ_B, defined to lie in the interval $(-\pi,\ \pi]$. Figure 4.5 shows the eigenvalue distributions obtained by the time-stepping method with the parameter $\Delta t = 1.0$ and 0.5. An integer n in Eq. 4.10 is set to 0, which means that ω satisfies $-\dfrac{\pi}{\Delta t} < \omega \leq \dfrac{\pi}{\Delta t}$. Figure 4.5 clearly indicates that the aliasing problem occurs and there is a Nyquist frequency $\omega_N = \dfrac{\pi}{\Delta t}$. In the case of $\Delta t = 1.0$, the eigenvalues in the region of $|\omega| > \pi$ jump to the region of $|\omega| < \pi$, and the similar phenomenon also occurs with $|\omega_N| = 2\pi$ in the case of $\Delta t = 0.5$.

Therefore, the original frequency should be confirmed by comparing with the results of the additional global linear stability analysis with different Δt, the direct numerical simulation, or other available data, etc.

On the computational cost and coding

The spectral transformation needs the highest computational cost of all the routines for the global linear stability analysis. Table 4.2 shows the computational time and memory requirements for performing the global linear stability analysis by using the time-stepping method and the shift-invert method. Here, the CPU used for this analysis is the Intel Core i7 3930K (6

Table 4.2: Computational time (CPU time) and memory requirements for performing the global linear stability analysis. Flow conditions are $Ma = 0.2$ and $Re = 45$.

	Dimension of Jacobian matrix	CPU time (sec)	Memory (MBytes)
Time-stepping	4.8×10^4	4.9×10^2	5.4×10^2
method	1.4×10^5	3.3×10^3	1.5×10^3
$(M = 300, \Delta t = 0.5)$	3.2×10^5	1.6×10^4	3.2×10^3
Shift-invert	4.8×10^4	2.0×10^2	6.8×10^2
method	1.4×10^5	8.5×10^2	2.1×10^3
$(M = 300, s = 0)$	3.2×10^5	2.5×10^3	4.9×10^3

cores, 3.2 GHz) and the codes are parallelized with OpenMP. For the shift-invert method which forms a matrix, the matrix is stored by the compressed sparse row (CSR) format which saves the computational memory by storing only non-zero elements of a sparse matrix.

Table 4.2 indicates that the time-stepping method needs much computational time because it conducts the numerical simulations of time developing of fluids. The computational time cost of the time-stepping method strongly depends on flow conditions. For example, a simulation of low Mach number flows needs high computational time costs due to the discrepancy of small time-step size for the numerical simulation which is restricted by the CFL condition and the time scale of the physical phenomena. Other cases whose time marching takes a high cost, such as high Reynolds number wall-bounded flows, are also computationally expensive. On the other hand, the routines of shift-invert method itself are not affected by flow conditions.

However, because the shift-invert method forms the Jacobian matrix $\boldsymbol{A}$ and perform direct inversions of it, the memory requirement for the shift-invert method is much larger than that of the time-stepping method. The memory requirements for the shift-invert method is proportional to the square of the dimension of the Jacobian matrix $\boldsymbol{A}$. Therefore, the memory requirement rapidly increases when the analysis has third-dimension and/or the number of grid points increases. This problem can be critical when the available memory of the computer is not sufficient. By contrast, the memory requirement for the time-stepping method is considerably less than that of the shift-invert method because it is proportional to the dimension of Jacobian

matrix $\boldsymbol{A}$. This is because the time-stepping method does not form the Jacobian matrix $\boldsymbol{A}$, in other words, this method is matrix-free.

Moreover, the coding of the routines for performing the time-stepping method is easy. This method uses the time integration routine of CFD as the spectral transformation and does not need to form any matrix explicitly, as explained in Section 2.3.1. Therefore, the code of the global linear stability analysis with the time-stepping method is mainly based on conventional CFD codes. Only the routines of the Arnoldi method and a conventional solver for eigenvalue problems of a small dense matrix (such as LAPACK) need to be added. On the other hand, the shift-invert method need to store a huge and sparse (or sometimes dense) matrix and invert it, and therefore its coding is a little more difficult than that of the time-stepping method.

In this study, we use the time-stepping method as the spectral transformation, because the memory requirements might be a crucial problem if many grid points are used for fluid simulations.

4.4 Proposed method for global linear stability analysis

In this section, we propose and validate the numerical method for the global linear stability analysis using the time-stepping method as the method for the spectral transformation and the compact difference scheme as the method for spatial discretization of the governing equation. Then, validations of the proposed method are conducted and influences of an outflow boundary condition on the global linear stability analysis are investigated. The method proposed here is used in Chapter 5.

4.4.1 Introduction of proposed method

The proposed method is the method that uses the time-stepping method and the compact difference scheme as methods for the spectral transformation and the numerical simulation of fluids, respectively. The term $\boldsymbol{B\zeta}$ in the Arnoldi iterations is calculated by Eq. 2.28, which needs to solve a linearized governing equation (Eq. 3.21, in this study).

The advantage of the use of Eq. 2.28, rather than Eq. 2.29, for evaluating the term $\boldsymbol{B\zeta}$ is that it can exclude the arbitrary parameter ε which affects the accuracy of the approximation of the derivative in Eq. 2.29. Although the calculation of Eq. 2.28 needs to solve the linearized

governing equation Eq. 3.21 in addition to the full governing equation Eq. 3.1, this calculation is easy because the compact difference scheme can solve both equations in the same manner. In addition, other fluid simulations such as the magnetohydrodynamics (MHD)[50] and supersonic flows[36,37] also can be solved in the same manner. Moreover, the compact difference scheme can achieve the high-order spatial accuracy. Therefore, this method is often used for the simulations of vortical flows,[51,52] turbulent flows,[53–55] and the aeroacoustics,[56,57] which need to resolve small spatial structures and perturbations of fluids. Because the number of computational grid points for high-order spatial accuracy schemes is less than for lower-order spatial accurate schemes, the dimension of the matrix $\boldsymbol{A}$ also becomes small when the compact difference scheme is used, and therefore the saving of computational memory is achieved. Besides, the proposed method does not need much computational memory and its coding is easy because the time-stepping method is used as the spectral transformation.

Although each of these methods, namely the compact difference scheme and the time-stepping method, has been used for the global linear stability analysis by some researchers,[13,58] the combination of these methods has not been used and validated. As mentioned above, the combination of these method has good properties: the high-order spatial accuracy, the applicability to various fluid phenomena, the low memory requirement, and the simplicity of the coding. Therefore, this method is promising for the future studies such as analyses of three-dimensional flows, the aeroacoustics, turbulent flows, and the magnetohydrodynamics (MHD), which need to solve small spatial structures and/or various governing equations. In the following sections, the validation of this method is conducted.

4.4.2 Problem description and Numerical method for validation analysis

Flow condition and computational grid

The flowfield to be analyzed is two-dimensional flows past a circular cylinder again, and the freestream Mach number Ma is 0.2. Three cases of the Reynolds number Re between 45 and 50 are analyzed. The computational grid used in this calculation is similar to that of Fig. 4.2. The number of grid points is 121×181 (azimuthal $\times$ radial directions) for the half domain ($y \geq 0$) and 241×181 for the entire domain. The minimum grid spacing is $\Delta_{min} = 0.005D$.

Simulation of full compressible Navier-Stokes equation for obtaining basic state $\bar{q}$

The sixth-order compact difference scheme is used for the calculations of inviscid and viscous terms of the full compressible Navier-Stokes equation Eq. 3.1. The eighth-order tridiagonal filter is used in order to suppress spurious oscillations. The coefficient α_f is set to 0.495. Time integration is made by the third-order TVD Runge-Kutta scheme.

The wall boundary conditions are same as Eqs. 4.2 - 4.5 except for the evaluation of $\frac{\partial}{\partial n}$. Here, the partial difference $\frac{\partial}{\partial n}$ is evaluated by the second-order one-sided finite difference method.

The compact difference scheme is sensitive to outflow boundary conditions, because the acoustic waves and vortical structures propagate with less dissipation and reflect at the boundary (it will be discussed later). Therefore, in order to suppress such spurious effects, the outflow boundary is placed at far distances of $r = 150D$, in addition, simple non-reflecting boundary conditions proposed by Rudy and Strikwerda[59,60] are adopted. The non-reflecting outlet is achieved by the following equations:

$$\frac{\partial p}{\partial t} - \rho c \frac{\partial V}{\partial t} + \alpha_{rs}(p - p_\infty) = 0 \tag{4.11}$$

where α_{rs} is a constant and set to 1.5. V denotes a velocity in the normal direction to the boundary.

The discretization of Eq. 4.11 is as follows:[59]

$$p_{ib}^{n+1} = \frac{p_{ib}^n + \alpha_{rs}\Delta t_n p_\infty + \rho_{ib}^n c_{ib}^n (V_{ib}^{n+1} - V_{ib}^n)}{1 + \alpha_{rs}\Delta t_n} \tag{4.12}$$

where superscript n denotes the time step, and Δt_n denotes the time step size. Other variables are extrapolated as follows:

$$u_{ib} = u_{ib-1}, \quad v_{ib} = v_{ib-1}, \quad T_{ib} = T_{ib-1} \tag{4.13}$$

On the symmetry plane $y = 0$, the symmetry boundary conditions are used in order to obtain steady states at the Reynolds number higher than a critical value.

Simulation of Linearized compressible Navier-Stokes equations for time-stepping method

As mentioned above, the linearized compressible Navier-Stokes equation Eq. 3.21 can be solved in the same manner with the full compressible Navier-Stokes equation Eq. 3.1. Therefore, the

sixth-order compact difference scheme, the eighth-order tridiagonal filter with $\alpha_f = 0.495$, and the third-order TVD Runge-Kutta scheme are used for the simulation of the linearized compressible Navier-Stokes equation.

Initial conditions are set to $\boldsymbol{q}'(t_0) = \boldsymbol{\zeta}$. This means that a vector $\boldsymbol{\zeta}$ in Arnoldi iterations is used as an initial perturbation.

Boundary conditions are obtained by substituting $\boldsymbol{q} = \bar{\boldsymbol{q}} + \boldsymbol{q}'$ into the boundary conditions for the full compressible Navier-Stokes equation.

$$u' = 0 \tag{4.14}$$

$$v' = 0 \tag{4.15}$$

$$\frac{\partial p'}{\partial n} = 0 \tag{4.16}$$

$$\frac{\partial T'}{\partial n} = 0 \tag{4.17}$$

Similarly, outflow boundary conditions are,

$$p'^{n+1}_{ib} = \frac{p'^{n}_{ib} + \bar{\rho}_{ib}\bar{c}_{ib}(V'^{n+1}_{ib} - V'^{n}_{ib})}{1 + \alpha_{rs}\Delta t} \tag{4.18}$$

and,

$$u'_{ib} = u'_{ib-1}, \quad v'_{ib} = v'_{ib-1}, \quad T'_{ib} = T'_{ib-1} \tag{4.19}$$

4.4.3 Validation results

The eigenvalues of the most unstable mode produced by the proposed method is also shown in Fig. 4.4 along with the results of Section 4.3. Similarly to the cases of Section 4.3, the real part (growth rate) and the imaginary part (frequency) increase as the Reynolds number increases, although the imaginary parts are a little different because of the difference of the Mach number. The critical Reynolds and Stouhal numbers are estimated to $Re_{cr} = 47$ and $St_{cr} = \dfrac{0.724}{2\pi} = 0.115$, respectively. Figure 4.6 shows the eigenvalue distributions for the case of $Re = 50$. This eigenvalue distribution is similar with a result of an incompressible flow analysis conducted by Tezuka and Suzuki.[58] More specifically, except for the most unstable mode, the growth rate decreases as the frequency increases because high frequency modes have small spatial structures and therefore they are susceptible to the viscosity.[58] At $Re = 50$, only the most unstable mode has a positive real part, and the real and imaginary parts of this mode

are $\sigma = 1.09 \times 10^{-2}$ and $St = 0.116$. The eigenvectors of this mode are shown in Fig. 4.7. These results are in good agreement with previous studies[16, 18, 19, 58] and the results of Section 4.3.

Figure 4.8 shows the comparison of two flowdields. The one is an unsteady flowfiled (the Kármán vortex-street) obtained by a direct numerical simulation, and the other is made by a superimposition of the steady flowfield (this is the basic state $\bar{\boldsymbol{q}}$) and the eigenvectors (Fig. 4.7) of the most unstable mode. These flowfields are quite similar, especially in the wake region near the circular cylinder. The reason of the difference of the wake flows far from the cylinder is that a perturbation is influenced by nonlinear effects when it grows enough.

Then, the temporal evolution of the perturbations are calculated by the direct numerical simulation in order to validate the eigenvalue. As the initial condition, the superimposition of the steady flowfield and the eigenvectors of the most unstable mode are used. Figure 4.9 shows the time history of the velocity in y-direction of the perturbation, at $x/D = 10$, $y/D = 0$. The figure indicates that the perturbation is oscillatory and its amplitude grows in time. The growth rate and the Strouhal number $\left(= \dfrac{\omega}{2\pi}\right)$ of the oscillation are estimated to $\sigma = 1.07 \times 10^{-2}$ and $St = 0.116$, when we assume that the perturbation follows the function $v(t) = \exp(\sigma t)\cos(\omega t)$. The estimated growth rate and the Strouhal number agree very well with the eigenvalue obtained by the global linear stability analysis.

In conclusion, it is confirmed that the proposed method can analyze the global linear stability of two-dimensional compressible viscous flows.

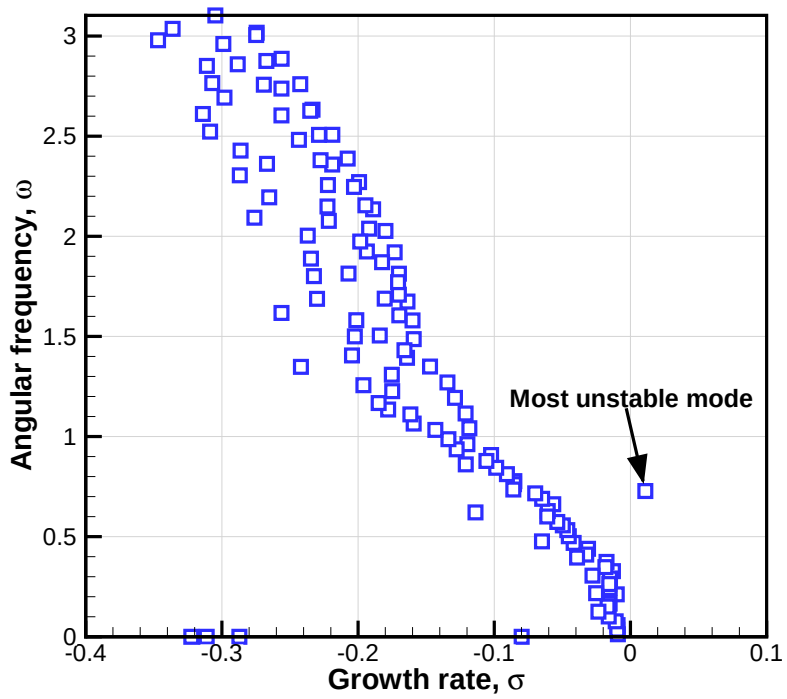

Figure 4.6: Eigenvalue distribution at $Re = 50$, $Ma = 0.2$.

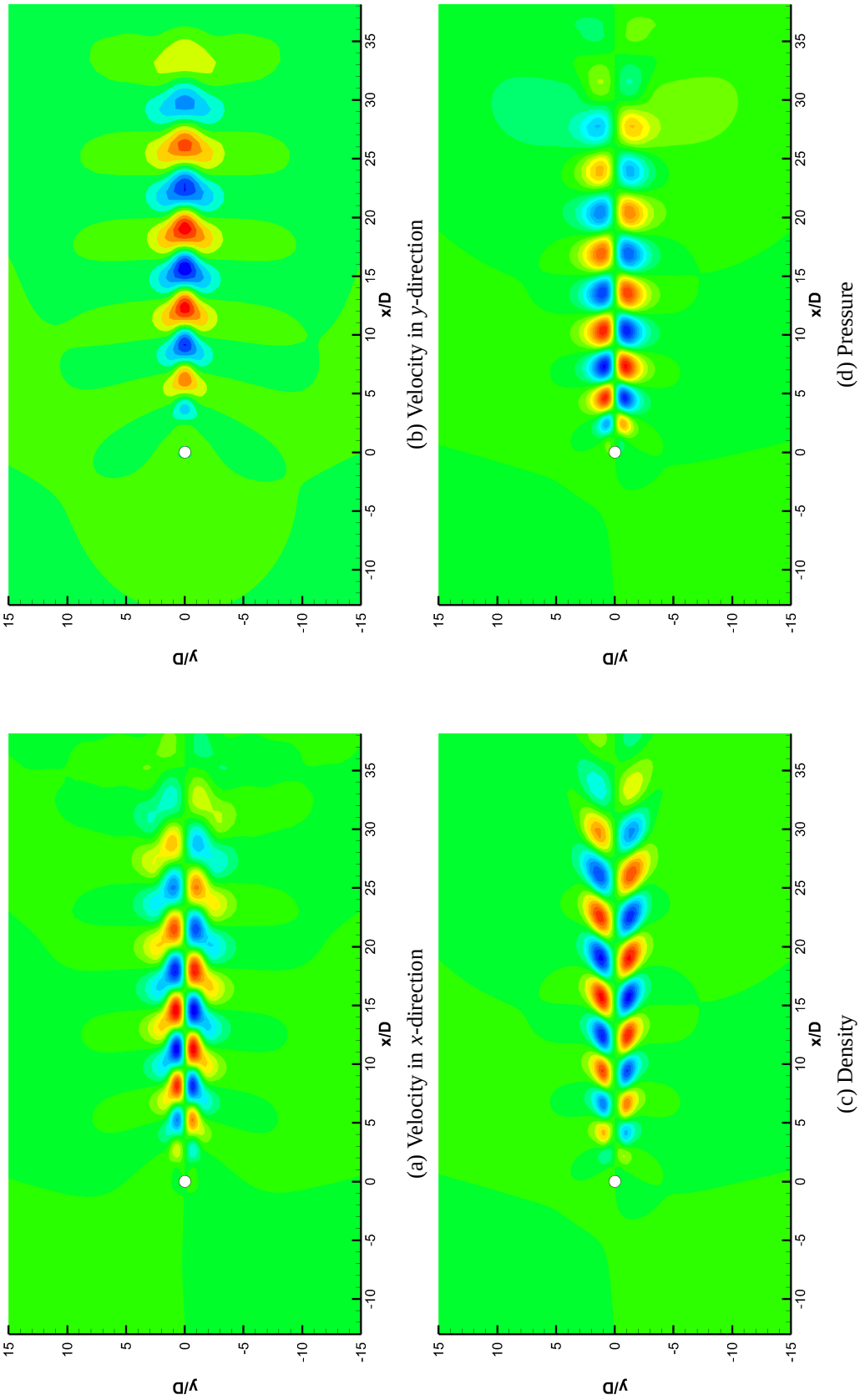

(a) Velocity in x-direction (b) Velocity in y-direction

(c) Density (d) Pressure

Figure 4.7: Eigenvectors of the most unstable mode at $Re = 50$, $Ma = 0.2$. Only the real part is shown.

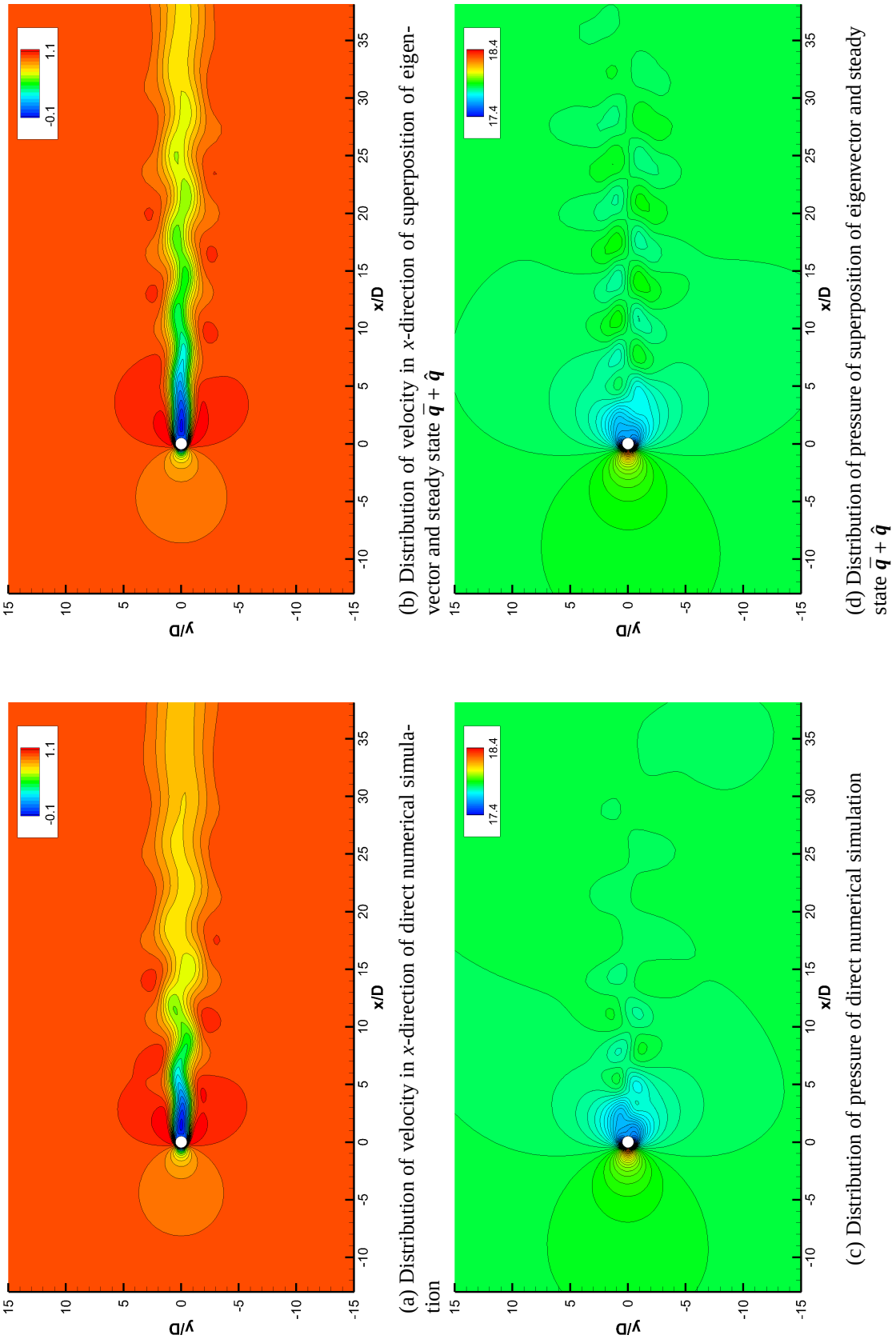

(a) Distribution of velocity in x-direction of direct numerical simulation

(b) Distribution of velocity in x-direction of superposition of eigenvector and steady state $\bar{\boldsymbol{q}} + \hat{\boldsymbol{q}}$

(c) Distribution of pressure of direct numerical simulation

(d) Distribution of pressure of superposition of eigenvector and steady state $\bar{\boldsymbol{q}} + \hat{\boldsymbol{q}}$

Figure 4.8: Comparison of results of direct numerical simulation and superposition of eigenvector and steady state $\bar{\boldsymbol{q}} + \hat{\boldsymbol{q}}$.

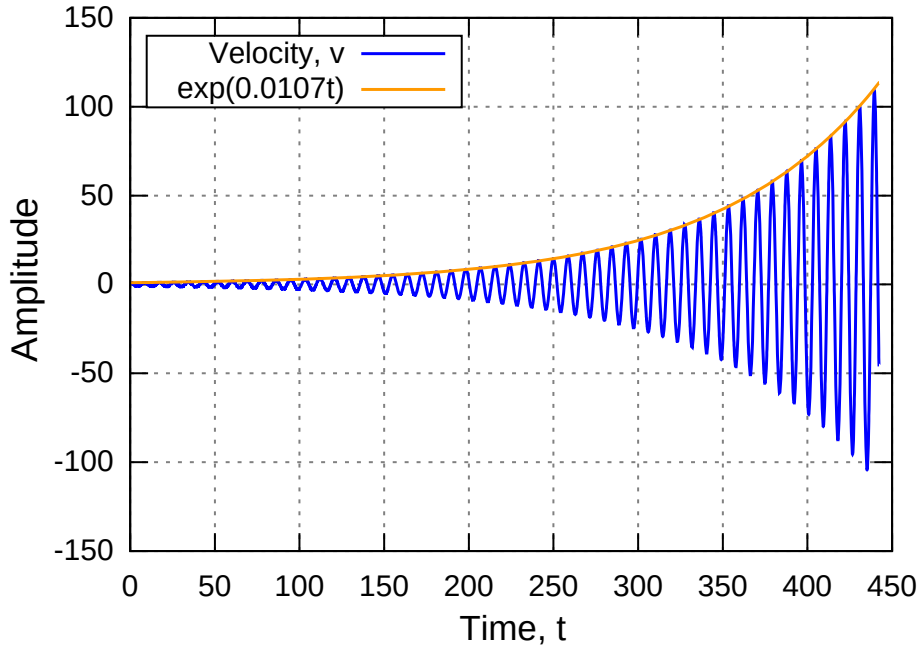

Figure 4.9: Temporal variation of the perturbation superimposed on the steady state at $Re = 50$, $Ma = 0.2$. The velocity v at $x/D = 10$, $y/D = 0$ is plotted. Growth rate and Strouhal number are estimated to $\sigma = 1.07 \times 10^{-2}$ and $St = 0.116$.

4.4.4 Effects of outflow boundary

When a numerical simulation of an external-flow is conducted, the computational domain has inflow and outflow boundaries. To obtain a realistic solution by the numerical simulation (CFD), a proper treatment of the outflow boundary is important because the outflow boundary contaminates the solution with the non-physical reflection of acoustic waves, fluid structures such as a vortex, and a numerical noise. It can be inferred that the global linear stability analysis is also affected by the outflow boundary. Therefore, the detailed analysis of this effect is desired.[26]

Here, we compare the results of global linear stability analysis with two different outflow boundary conditions. The one, case-1, is same as the above simulations, namely the non-reflecting boundary conditions proposed by Rudy and Strikwerda,[59,60] , namely (identical to Eqs. 4.12, 4.13, 4.18, and 4.19.),

$$p_{ib}^{n+1} = \frac{p_{ib}^{n} + \alpha_{rs}\Delta t_n p_\infty + \rho_{ib}^{n} c_{ib}^{n}(V_{ib}^{n+1} - V_{ib}^{n})}{1 + \alpha_{rs}\Delta t_n}$$

and,

$$u_{ib} = u_{ib-1}, \quad v_{ib} = v_{ib-1}, \quad T_{ib} = T_{ib-1}$$

for perturbations,

$$p'^{n+1}_{ib} = \frac{p'^{n}_{ib} + \overline{\rho}_{ib}\overline{c}_{ib}(V'^{n+1}_{ib} - V'^{n}_{ib})}{1 + \alpha_{rs}\Delta t}$$

and,

$$u'_{ib} = u'_{ib-1}, \quad v'_{ib} = v'_{ib-1}, \quad T'_{ib} = T'_{ib-1}$$

The boundary is placed at $r = 150D$.

The other, case-2, is as follows:

$$\rho_{ib} = 2\rho_{ib-1} - \rho_{ib-2} \tag{4.20}$$

$$(\rho u)_{ib} = 2(\rho u)_{ib-1} - (\rho u)_{ib-2} \tag{4.21}$$

$$(\rho v)_{ib} = 2(\rho v)_{ib-1} - (\rho v)_{ib-2} \tag{4.22}$$

$$p_{ib} = p_{\infty} \tag{4.23}$$

This outflow boundary condition assumes that the pressure recovers to the freestream value at the boundary and the other variables can be simply extrapolated from inside of the computational domain. Corresponding boundary conditions for perturbations are as follows:

$$\rho'_{ib} = 2\rho'_{ib-1} - \rho'_{ib-2} \tag{4.24}$$

$$(\rho u)'_{ib} = 2(\rho u)'_{ib-1} - (\rho u)'_{ib-2} \tag{4.25}$$

$$(\rho v)'_{ib} = 2(\rho v)'_{ib-1} - (\rho v)'_{ib-2} \tag{4.26}$$

$$p'_{ib} = 0 \tag{4.27}$$

In addition, the boundary is placed at $r = 50D$ in case-2.

Figure. 4.10 shows the eigenvalue distribution of the two cases. The figure clearly indicates that the eigenvalues obtained by the global linear stability analysis are affected by the outflow boundary. The eigenvalues of the two cases are not in correspondence except for the most unstable mode. The eigenvalues of the most unstable mode are $\lambda = -9.20 \times 10^{-3} + 7.22 \times 10^{-1} i$ for the case-1 and $\lambda = -4.77 \times 10^{-3} + 7.19 \times 10^{-1} i$ for the case-2. The eigenvectors of the most unstable mode are shown in Fig. 4.11. In case-2, the eigenvectors are contaminated with non-physical reflection waves although the structure of shear flow instability appears. The non-physical reflection is generated at the boundary which the wake flow is going out across. In contrast, any reflection waves are not observed in case-1.

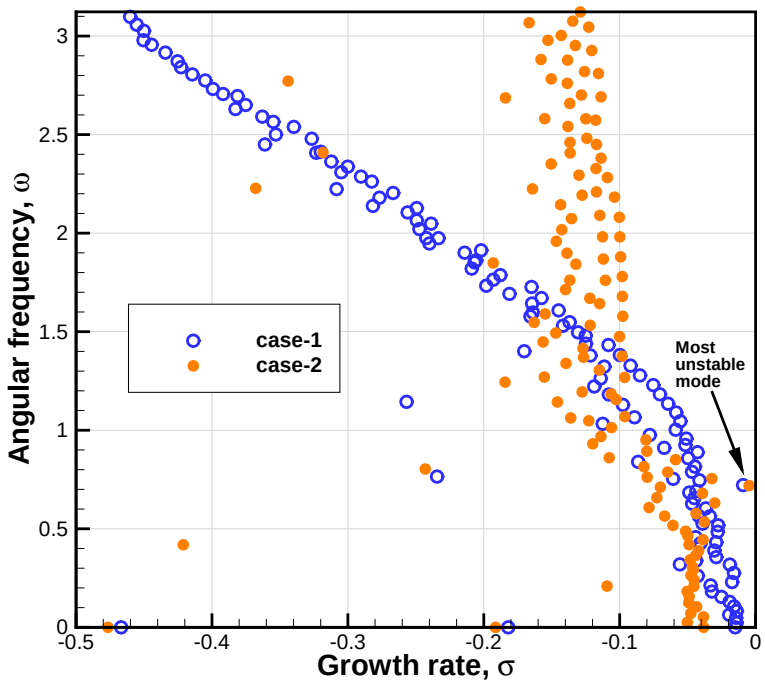

Figure 4.10: Comparison of eigenvalue distributions between case-1 and 2.

As a result, it is concluded that results of the global linear stability analysis are affected by the outflow boundary. However, such unfavorable effects of the outflow boundary can be avoided. The nor-reflecting boundary condition[59, 60] and to locate the boundaries far from a body are effective for reducing the influence of non-physical phenomenon on the global linear stability analysis. Therefore, it is important to carefully set the outflow boundary condition and confirm the influence of the outflow boundary on the results.

4.5 Applicability to flowfield including shock waves

4.5.1 Introduction

Shock waves appear in supersonic and transonic flows around a body. The shock wave is a rapid change of pressure, density, temperature, and so on. Therefore, when a perturbation cuts across the shock wave, the perturbation also experiences a rapid change, and the change might be nonlinear. Thus, the applicability of the global linear stability analysis to flowfields including shock waves is not obvious. However, the global linear stability analysis of supersonic and transonic flows can be helpful and desired because unsteady phenomena often occur in such

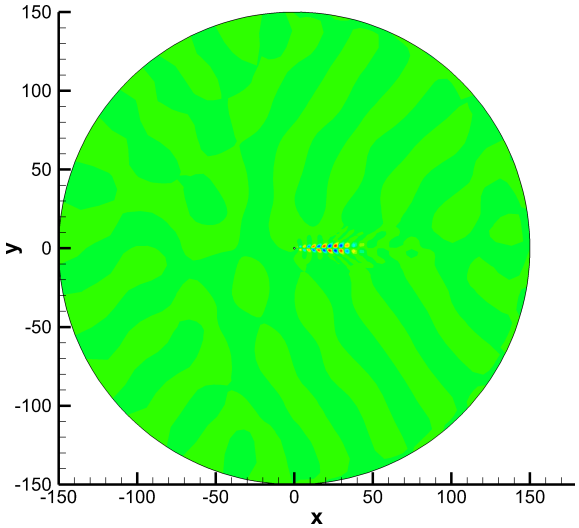

(a) Eigenvector of density for case-1

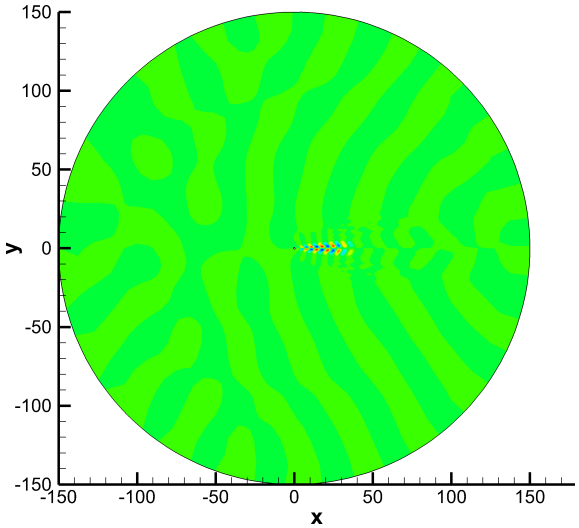

(b) Eigenvector of velocity in x-direction for case-1

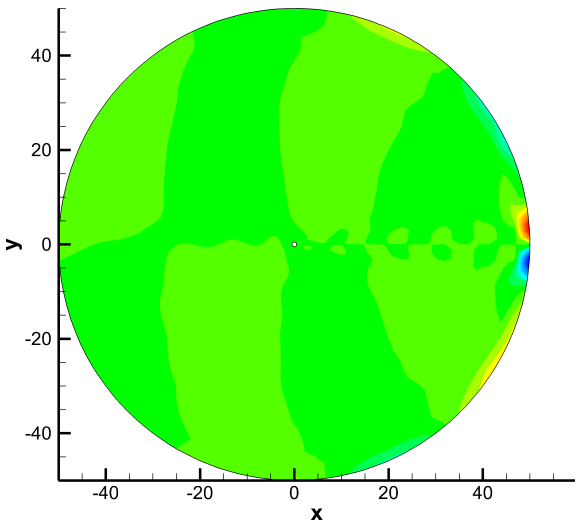

(c) Eigenvector of density for case-2

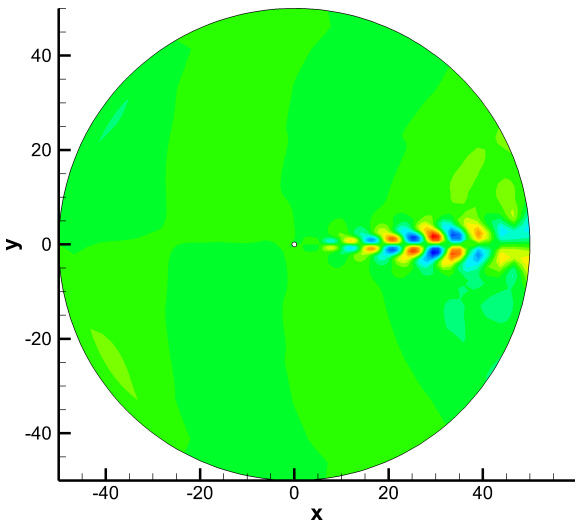

(d) Eigenvector of velocity in x-direction for case-2

Figure 4.11: Comparison of eigenvectors of the most unstable mode between case-1 and 2.

flows, for example, a shock wave/boundary layer interaction, a buffet phenomenon over an airfoil, a supersonic flow around a bluff body, and so on.

Crouch et al.[16,17] have conducted the global linear stability analysis of a transonic flow around the NACA0012 airfoil and investigated the shock-induced transonic-buffet. As a result, they have shown that the condition which introduces unsteadiness, predicted by the global linear stability analysis, coincides with experimental results. However, except for the works of Crouch et al., no previous studies have analyzed flowfields including shock waves by using the global linear stability analysis. Therefore, the applicability of the global linear stability analysis to flowfields including shock waves should be carefully validated.

We can assume that unsteady flows including shock waves can be classified into two cases. The one is the case that the flow is unsteady but the shock wave causes nor affects the unsteadiness, and the other is the case that the flow is unsteady and the shock wave causes or affects the unsteadiness. Apparently, it is more difficult for the global linear stability analysis to deal with the latter case than the former case, although Crouch et al. have successfully performed it.

In this section, we consider the former case and investigate applicability of our proposed method to flowfields including shock waves. Here, the wake of a circular cylinder is analyzed again although the freestream is supersonic.

4.5.2 Problem description and Numerical method

Flow condition and computational grid

The Mach number of the freestream is $Ma = 1.3$. A computational grid used for this simulation is similar to that of Fig. 4.2. The number of grid points is 211×601 (azimuthal $\times$ radial directions) for the half domain ($y \geq 0$) and 421×601 for the entire domain. The minimum grid spacing is $\Delta_{min} = 0.00049D$.

Simulation of full compressible Navier-Stokes equation for obtaining basic state $\bar{q}$

Same methods used in the above Section 4.4, namely the compact difference scheme, the tridiagonal filter, and the TVD Runge-Kutta scheme, are employed. The coefficient of the tridiagonal filter α_f is set to 0.495. In addition to the compact difference scheme, the LAD method is used in order to capture shock discontinuities.

The wall boundary conditions are also same as Eqs. 4.2 - 4.5 and the partial difference $\frac{\partial}{\partial n}$ is evaluated by the second-order one-sided finite difference method.

Flow variables are simply extrapolated by linear approximations for the outflow boundary because the flow is supersonic,

$$\rho_{ib} = 2\rho_{ib-1} - \rho_{ib-2} \tag{4.28}$$

$$u_{ib} = 2u_{ib-1} - u_{ib-2} \tag{4.29}$$

$$v_{ib} = 2v_{ib-1} - v_{ib-2} \tag{4.30}$$

$$T_{ib} = 2T_{ib-1} - T_{ib-2} \tag{4.31}$$

The symmetry boundary conditions are used at the symmetry plane $y = 0$ when we calculate the steady state for obtaining the basic state $\overline{\boldsymbol{q}}$.

Simulation of Linearized compressible Navier-Stokes equations for time-stepping method

The methods for solving the linearized compressible Naview-Stokes equations are also same as the above Section 4.4.

Initial conditions are $\boldsymbol{q}'(t_0) = \boldsymbol{\zeta}$ and wall boundary conditions are Eqs. 4.14 - 4.17.

The outflow boundary conditions are as follows:

$$\rho'_{ib} = 2\rho'_{ib-1} - \rho'_{ib-2} \tag{4.32}$$

$$u'_{ib} = 2u'_{ib-1} - u'_{ib-2} \tag{4.33}$$

$$v'_{ib} = 2v'_{ib-1} - v'_{ib-2} \tag{4.34}$$

$$T'_{ib} = 2T'_{ib-1} - T'_{ib-2} \tag{4.35}$$

4.5.3 Results and Discussions

Results of direct numerical simulations

Figure 4.12 shows a steady flowfield at $Re = 2500$. A bow shock and trailing shock waves occur in front of and behind the circular cylinder, respectively. In addition, there is a steady free shear flow behind a twin-vortex attached to the cylinder. Figure 4.13 shows the unsteady flowfield at $Re = 5000$. It can be confirmed that the free shear flow becomes unstable and generates a

vortex-street. The spatial wavelength of the vortex is estimated to $\lambda_{spatial} \simeq 1.0D$. The frequency distribution shown in Fig. 4.14 indicates that there is the peak frequency of $St = 1.0$.

Results of global linear stability analysis

Figure 4.15 shows the eigenvalue distribution at $Re = 5000$. The distribution shows that the growth rate decreases as the frequency increases except for several distinguishing modes whose growth rates are relatively high. This distribution is similar to that of subsonic flows around a circular cylinder discussed above.

The eigenvector of the mode-a (illustrated in Fig. 4.15) is shown in Fig. 4.16. We can confirm that the instability of free shear flows (namely, alternating distributions) appears. The Strouhal number of this mode is $St = 0.95$ and the spatial wavelength is $\lambda_{spatial} = 0.95$ estimated from this figure. Because the modes whose frequencies are close to $St = 1.0$ are relatively unstable (shown in Fig. 4.15), it is inferred that these modes appear and make the dominant structure of Fig. 4.13. These results indicate that the proposed method can capture the global linear stability of free shear flows even if the flowfield includes shock waves in the computational domain.

However, the results also indicate that all the oscillatory modes are stable ($\sigma < 0$) and there are several distinguishing modes (for example, mode-b) whose growth rates are larger than mode-a. Therefore, it is inferred that the transition from steady to unsteady flows is triggered by other physics such as the non-modal linear instability. Further investigations are necessary to clarify the cause of this discrepancy.

As expected, spurious modes which might be caused by numerical instability due to the shock wave appear as a result of the global linear stability analysis. Figure 4.17 shows the eigenvector of the one of the spurious mode which is labeled mode-c in Fig. 4.15. It is inferred that this mode indicates the instability caused by a misalignment of the shock wave and the computational grid lines. To reduce the effect of numerical instability due to shock waves, it is important to stably capture the shock waves by numerical schemes.

4.5.4 Conclusion of this section

In this section, we investigated the applicability of the proposed method for the global linear stability analysis of a flowfield including shock waves. We confirmed that the proposed method is able to analyze the global linear stability of the free shear flow behind a circular cylinder

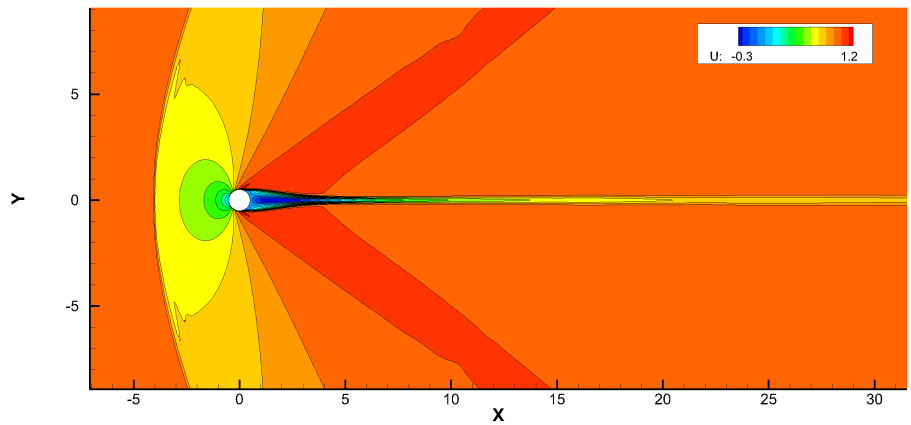

(a) Velocity in x-direction

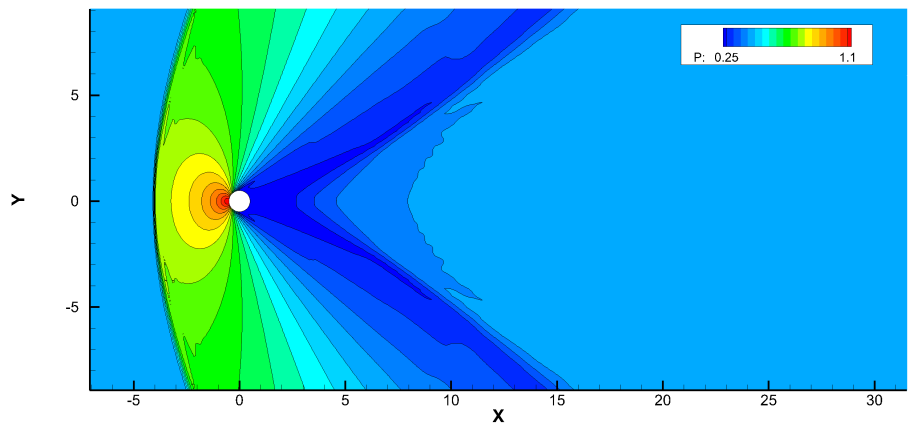

(b) Pressure

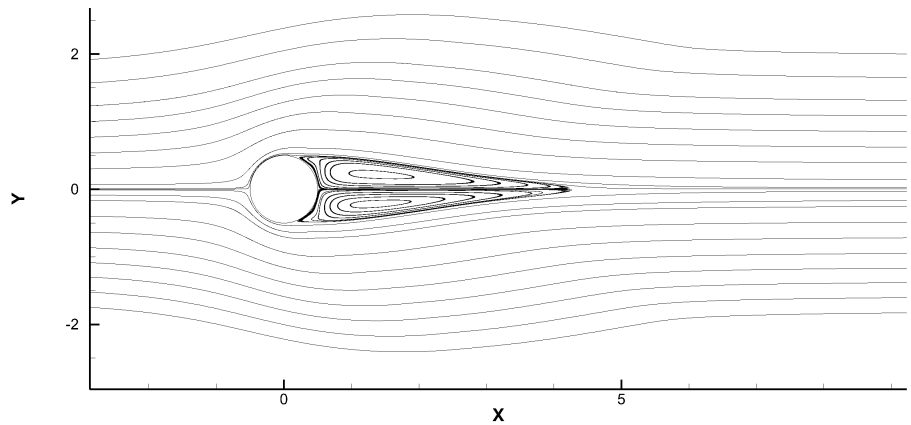

(c) Streamlines

Figure 4.12: Steady flowfield at $Re = 2500$.

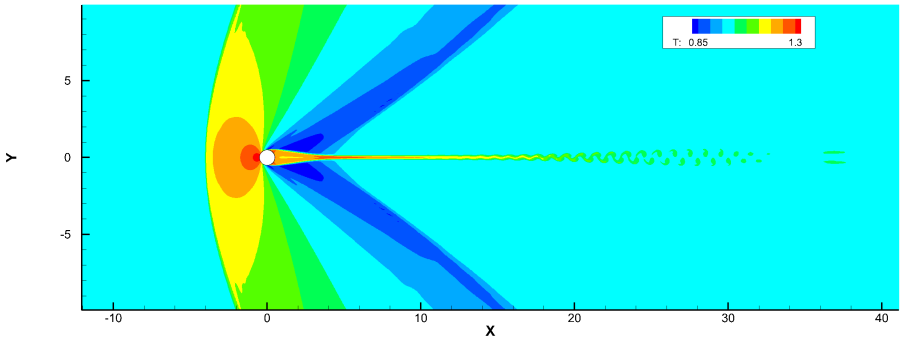

(a) Temperature

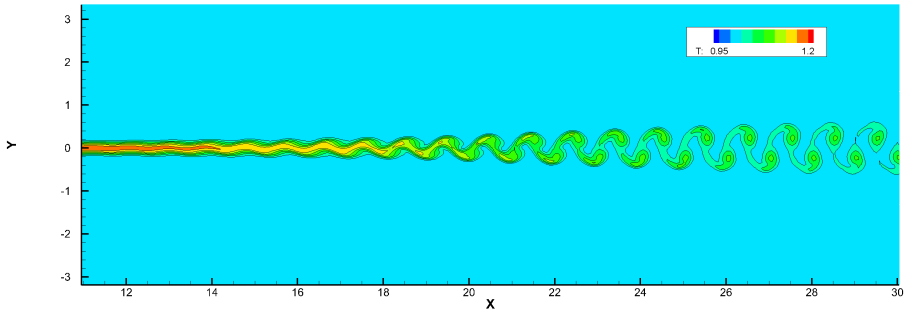

(b) Temperature. Close-up view of shear flow instability.

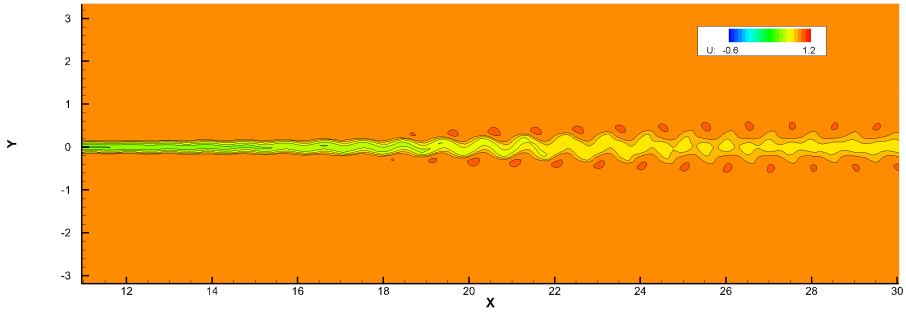

(c) Velocity in x-direction. Close-up view of shear flow instability.

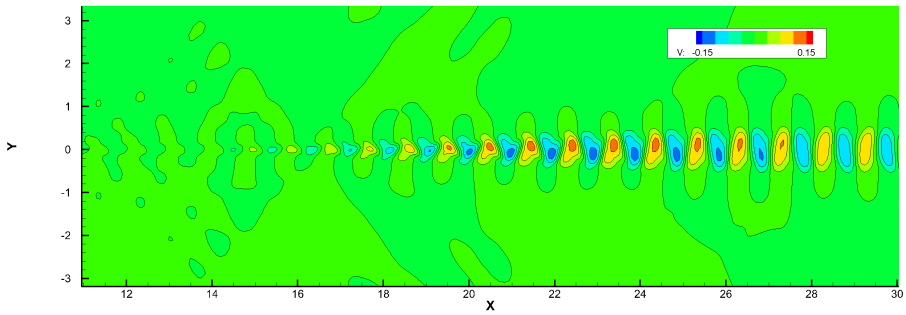

(d) Velocity in y-direction. Close-up view of shear flow instability.

Figure 4.13: Unsteady flowfield at $Re = 5000$.

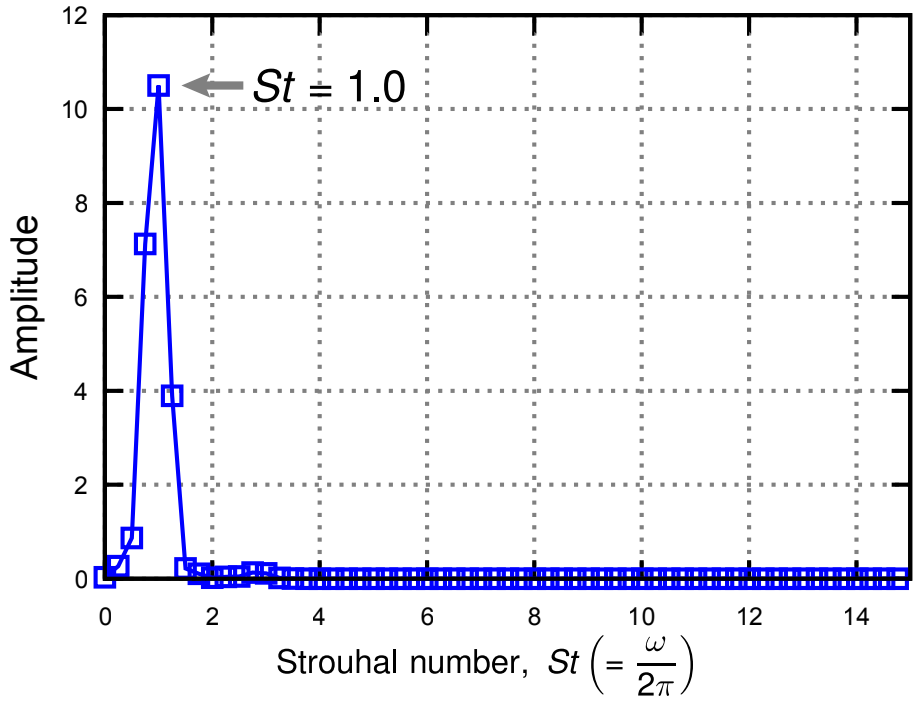

Figure 4.14: Frequency distribution of unsteady flow at $Re = 5000$. The reference point for obtaining the temporal variation is $x/D = 25$, $y/D = 0$.

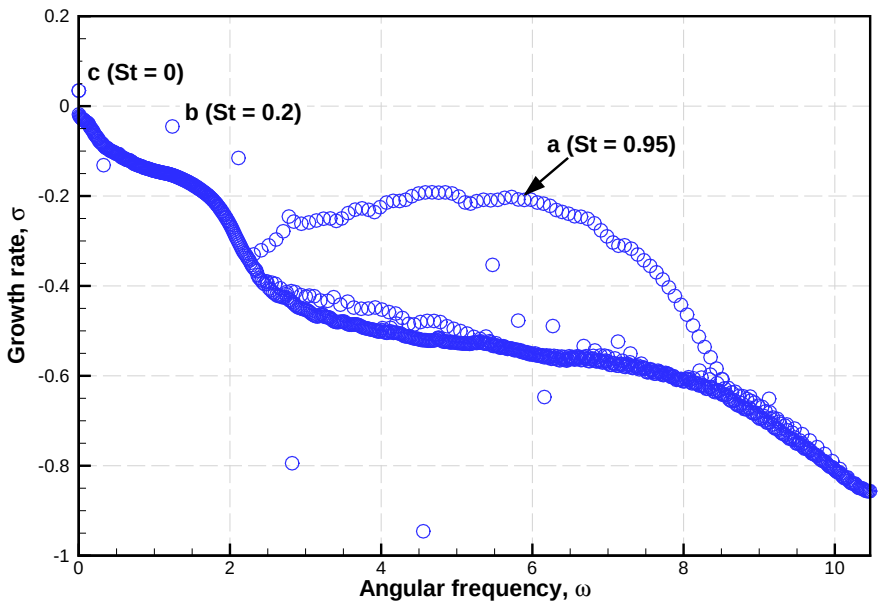

Figure 4.15: Eigenvalue distribution at $Re = 5000$. Three characteristic eigenmodes are labeled a, b, and c.

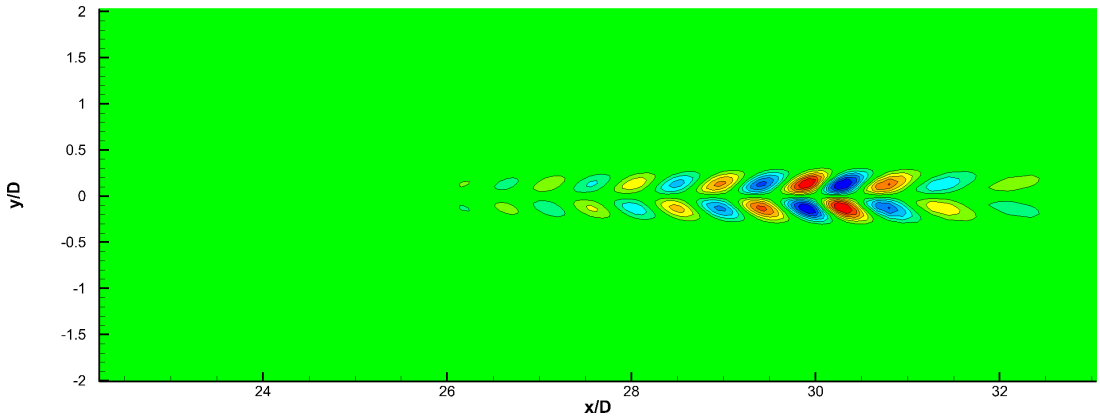

(a) Temperature

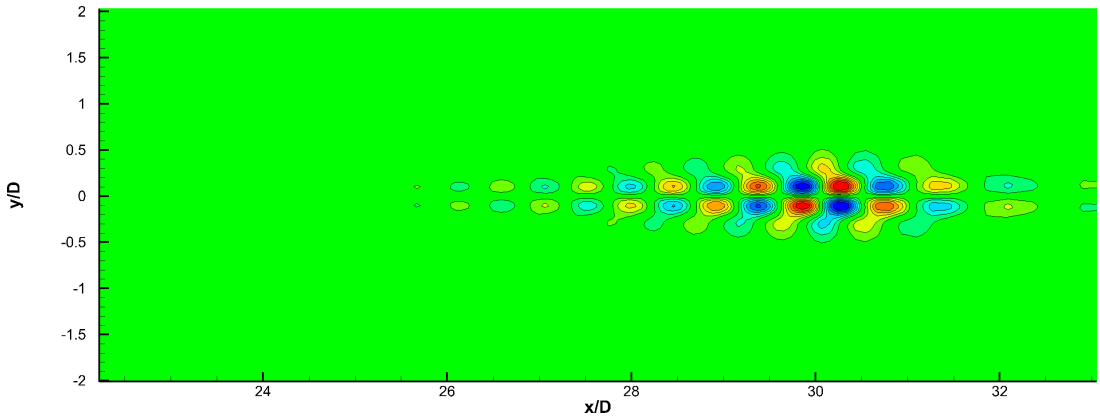

(b) Velocity in *x*-direction

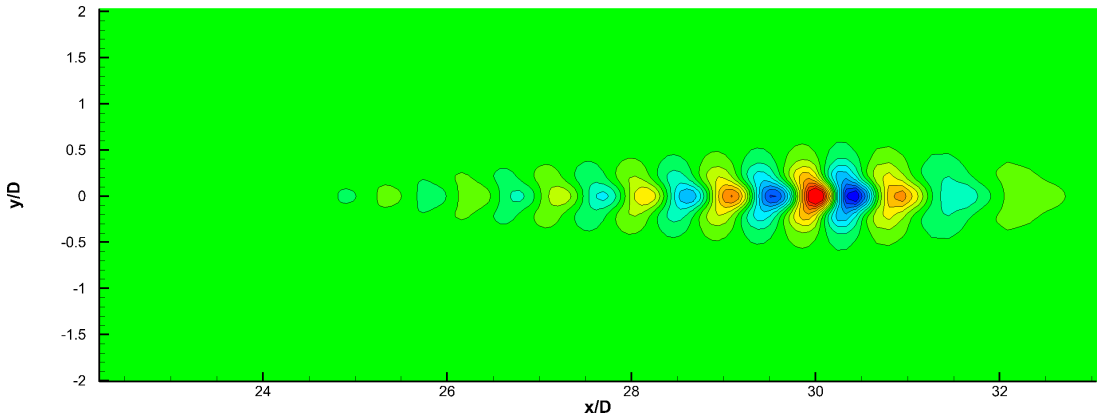

(c) Velocity in *y*-direction

Figure 4.16: Eigenvectors of mode-a. Only the real part is shown.

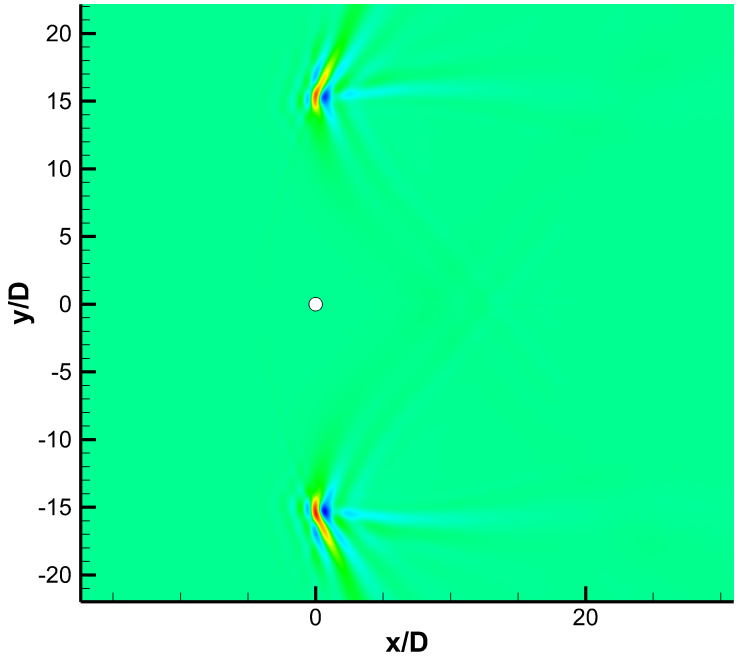

Figure 4.17: Spurious mode. Density eigenvector of mode-c.

whose flowfield includes shock waves. The frequency and the spatial wavelength of the eigenmode are similar to those of the vortex-street of unsteady flows at $Re = 5000$. However, the spurious mode due to the shock wave also appeared as a result of the global linear stability analysis. Therefore, when a flowfield to be analyzed includes a shock wave, the shock wave needs to be stably solved and we must carefully check whether the obtained results are caused by numerical or physical instability.

4.6 Summary of this chapter

In this chapter, we proposed and validated a numerical method of the global linear stability analysis for compressible viscous flows.

First, the time-stepping method and the shift-invert method were compared. The results showed that both method produce qualitatively same results and the results coincide with the results of previous studies. In terms of a computational time cost, the cost of the time-stepping method can be higher than that of the shift-invert method because the time-marching of flow simulations is computationally expensive. However, the shift-invert method needs much computational memory because it forms and inverts a matrix, whereas the time-stepping method

does not need much memory because it does not form any matrix. If the the number of grid points is large, which leads large dimensions of the Jacobian matrix A, the memory requirements of the shift-invert method may exceed the available memory. In addition, the time-stepping method has the advantage of simplicity of its coding.

Then, we proposed and validated a method for the global linear stability analysis which has the high-order spatial accuracy, memory saving properties, the applicability to various equations, and the simplicity of the coding. The method uses the time-stepping method as the spectral transformation and the compact difference scheme as the discretization method for fluid simulations. As a validation of the method, the analysis of the two-dimensional flows past a circular cylinder was conducted. It was confirmed that the method can produce the accurate eigenvalue and eigenvector. In addition, the influence of the outflow boundary on the global linear stability analysis was investigated. The result shows that results of the global linear stability analysis are affected by the outflow boundary and the influence can be avoided by setting the appropriate boundary condition.

Finally, the applicability of the proposed method to a flowfield including shock waves was investigated. As a result, we confirmed that the proposed method is able to analyze the global linear stability of the free shear flow behind a circular cylinder whose flowfield includes shock waves. However, it is necessary to confirm the effect of numerical instability on the result because spurious modes caused by shock waves also appear in the result.

The method proposed and validated in this chapter is used in the next chapter.

5 Global Linear Stability Analysis of Compressible Cavity Vortex

5.1 Introduction

In this chapter, to elucidate the effects of compressibility on the stability of vortical flows, the instability of a compressible cavity vortex is analyzed by the global linear stability analysis.

A cavity flow is one of the most basic vortical flows and many studies have been conducted for several decades. The studies on the cavity flows are roughly classified into two categories. The one is the study on the cavity tone.[13,61] The cavity tone is a noise caused by a shear flow which separated from the cavity front edge and impinges on the cavity rear edge. The investigations of this flow are very important because the cavity tone appears in many engineering applications although its flow physics is complex. The latter is study on the Lid-Driven Caivty (LDC).[62–65] The LDC has a square domain which is composed of three stationary walls and one moving wall. The LDC is often used as a test problem for validation of numerical schemes for a fluid simulation because the its geometry and boundary conditions are very simple. Especially, results of numerical simulations conducted by Ghia et al.[62] is famous and often used as data for a comparison. The flowfield of LDC becomes unsteady from the steady state when the Reynolds number exceeds a certain value (called the critical Reynolds number Re_{cr}). In this study, we conduct the global linear stability analysis of the LDC flow because this flowfield has unsteady phenomenon of a vortex and it is easy to conduct numerical simulations because of its simple geometry and boundary conditions.

The velocity profiles on the walls of the cavity to be analyzed in this study are as follows:

at a moving wall

$$u = 16u_{max}(x/L)^2(1 - x/L)^2 \tag{5.1}$$

$$v = 0 \tag{5.2}$$

at stationary walls

$$u = 0 \tag{5.3}$$

$$v = 0 \tag{5.4}$$

where u and v are the velocity in x- and y-directions, and L is the length of one side of the square cavity. The LDC defined by this velocity profile is called the regularized cavity flow.

The regularized cavity flow was investigated by Shen.[66,67] He analyzed this flow by simulating a temporal development numerically. He reported that the first critical Reynolds number exists between 10000 and 10500, and the flowfiled becomes a time-periodic flow. He also reported that when Reynolds number exceeds about 15000, the flowfield breaks the time-periodicity. Here, the Reynolds number Re is defined by the maximum velocity of the moving wall u_{max} and the length of one side of the square cavity L.

Chiba[18,19] conducted the global linear stability analysis of this flowfield. He showed the following results,

- The critical Reynolds number is $Re_{cr} = 10150$ and the critical Strouhal number (nondimensional frequency) is $St_{cr} = 0.332$.
- Eigenmodes of this flowfiled can be classified into two modes, the one relates to instability of an inviscid vortex and the other relates to instability of shear flows.
- The most unstable mode is an unique mode because it relates to the both of above two instability.
- Instability of shear flows becomes unstable as the Reynolds number increases.

These results are explained in detail in Section 5.3.2. Note that the above-mentioned studies considered incompressible viscous flows.

As indicated by Chiba,[18,19] the instability of shear flows is closely related to the unsteadiness of the cavity flow. Compressibility effects on a free shear flow (or a mixing layer) were investigated by many researchers.[3–9] Especially, Sandham and Reynolds[8] revealed that the compressibility stabilizes a mixing layer, in other words, it suppresses the growth of the mixing layer.

In this chapter, to elucidate the effect of compressibility on the stability of vortical flows, we consider the global linear stability of the regularized cavity flow including compressibility. How the compressibility effects on shear flows relates to the stability of a cavity vortex is investigated.

5.2 Problem description and Numerical methods

In this study, the simulations of the full compressible Navier-Stokes equation Eq. 3.1 are conducted in order to obtain a basic state $\bar{\boldsymbol{q}}$ and analyze temporal development of a flowfield. The time-stepping method is used as a spectral transformation method, and the linearized compressible Navier-Stokes equation Eq. 3.21 is solved to obtain $\boldsymbol{B}\boldsymbol{\zeta}_k$ of Eq. 2.28. The problem description and the methods for these simulations are explained below.

5.2.1 Simulation of full compressible Navier-Stokes equation for obtaining basic state $\bar{\boldsymbol{q}}$

The sixth-order compact difference scheme is used for the calculations of inviscid and viscous terms of the full compressible Navier-Stokes equation. The eighth-order tridiagonal filter is used in order to suppress spurious oscillations. The coefficient α_f is set to 0.45. Time integration is performed by the third-order TVD Runge-Kutta scheme.

Initial velocity fields are set to be stationary. Namely,

$$u_0 = 0 \tag{5.5}$$

$$v_0 = 0 \tag{5.6}$$

where the subscript 0 denotes the initial condition. The initial density, temperature, and pressure are set to the values satisfying the setup Reynolds number. Here, the Reynolds number are defined as follows:

$$Re = \frac{\rho_0 u_{max} L}{\mu_0} \tag{5.7}$$

The velocity profiles on the walls follow the Eqs. 5.1-5.4. The wall temperature is assumed to be constant at $T = T_0$. The pressure on the walls is calculated as follows:

$$\frac{\partial p}{\partial n} = 0 \tag{5.8}$$

where n indicates a vector normal to the cavity wall. The partial difference $\frac{\partial}{\partial n}$ is evaluated by the second-order one-sided finite difference method.

For the discussions below, we define the time t as follows:

$$t = \frac{t^*}{L/u_{max}} \tag{5.9}$$

where t^* is time with units and $t = 0$ corresponds to the initial condition.

5.2.2 Simulation of Linearized compressible Navier-Stokes equations for time-stepping method

The sixth-order compact difference scheme, the eighth-order tridiagonal filter with $\alpha_f = 0.45$, and the third-order TVD Runge-Kutta scheme are used for the simulation of linearized compressible Navier-Stokes equations.

The initial conditions are set to $\boldsymbol{q}'(t_0) = \boldsymbol{\zeta}$. The boundary conditions are obtained by substituting $\boldsymbol{q} = \bar{\boldsymbol{q}} + \boldsymbol{q}'$ into the boundary conditions for the full compressible Navier-Stokes equation. Therefore, for all the wall boundaries,

$$u' = 0 \tag{5.10}$$

$$v' = 0 \tag{5.11}$$

$$\frac{\partial p'}{\partial n} = 0 \tag{5.12}$$

$$T' = 0 \tag{5.13}$$

5.2.3 Effect of parameters on global linear stability analysis

In this section, effects of computational grids and the number of iterations M of Arnoldi iterations on the results of global linear stability analysis are investigated. The integration time Δt of Eq. 2.23 is set to 0.1 for all the global liner stability analysis in this chapter.

grid refinement study

In order to check the grid dependency of the present analysis, the results from global linear stability analysis with two computational grids having different grid resolution are compared. Figure 5.1 shows a baseline grid as an example. The computational grids are non-uniform spaced Cartesian grids. Grid points for the baseline grid are 161×161, and the minimum grid

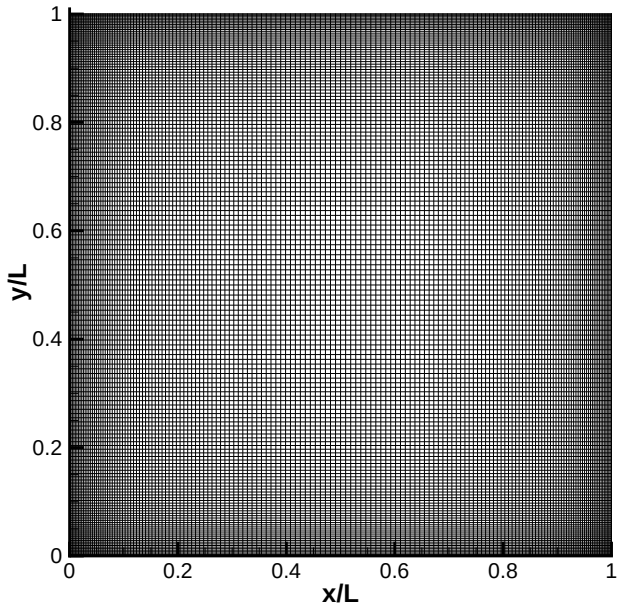

Figure 5.1: Computational grid.

spacing is $\Delta_{min} = 0.0025L$. Grid points for the fine grid are 241×241, and the minimum grid spacing is $\Delta_{min} = 0.001L$.

Figure 5.2 shows eigenvectors of an oscillatory mode (this mode, called mode-I in this study, is explained in Section 5.3.2 in detail) obtained by the global linear stability analysis on these computational grids. Flow conditions and the parameters of the Arnoldi method are $Ma = 0.3$, $Re = 10000$, $t = 1500$ and $M = 800$. By this comparison, we can confirm that mode shapes of the mode-I obtained on the different computational grids show good agreement. Corresponding eigenvalues are $\sigma = -6.49 \times 10^{-3}$ and $\omega = 2.07$ for the baseline grid, and $\sigma = -2.23 \times 10^{-2}$ and $\omega = 2.07$ for the fine grid, namely, the angular frequencies are same although the growth rates are a little different. Therefore, it can be concluded that the baseline grid has enough resolution for analyzing the qualitative properties (such as mode shapes and its frequency) of the eigenmodes, although the grid can not obtain a correct value of a growth rate because a grid resolution has a relatively large effect on it. In this chapter, we use the baseline grid because of high computational cost of the fine grid.

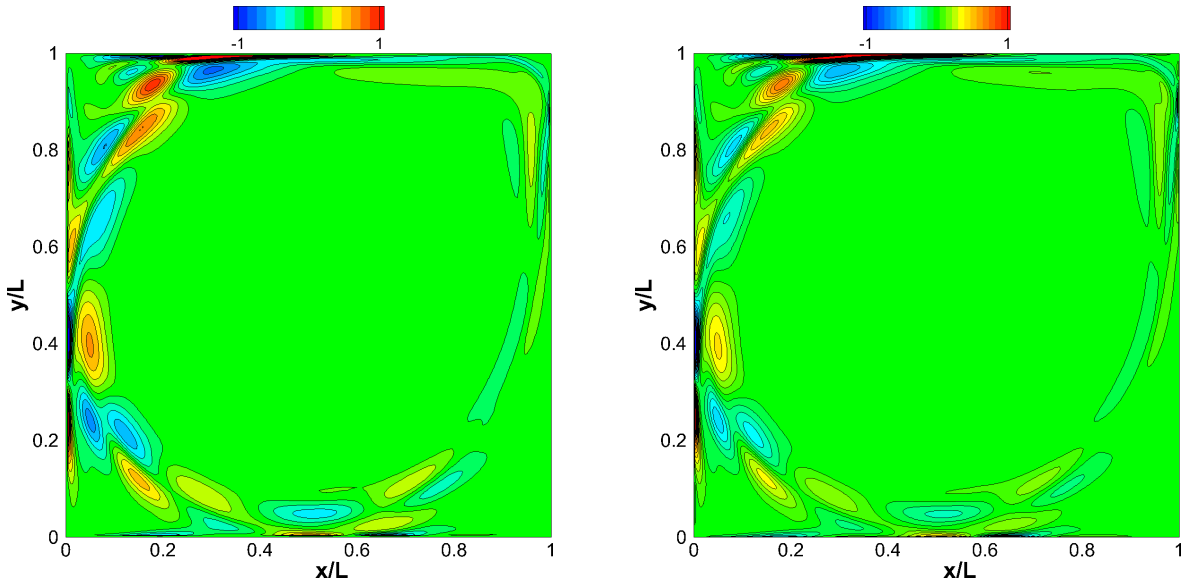

(a) Baseline grid (b) Fine grid

Figure 5.2: Comparison of vorticity eigenvectors of the mode-I obtained with different computational grids. Only the real part is shown.

Effect of the number of iterations M

Here, we check effects of the number of iterations M of Arnoldi iterations on the present global linear stability analysis. Figure. 5.3 shows the convergence properties of the growth rate and the angular frequency of the mode-I against the M. The changes in the growth rate and frequency are not very large, when the M is greater than 500. Figure. 5.4 shows the eigenvectors of density at different M. The mode shape at $M = 500$ and $M = 800$ are very similar. On the other hand, compared to other two cases, the mode shape at $M = 300$ is a little distorted. Consequently, it is confirmed that $M = 500$ is enough for convergence. In this chapter, $M = 800$ is used for all the analyses.

5.3 Results and Discussions

5.3.1 Temporal variation of compressible cavity flow

Figure 5.5 shows the time history of the velocity and density at a reference point ($x/L = 0.5, y/L = 0.75$) for the case of $Ma = 0.6$, $Re = 11000$. The density is still decreasing at $t = 3000$ while the velocity fields converged enough at $t = 1500$. In this flowfield, the kinetic

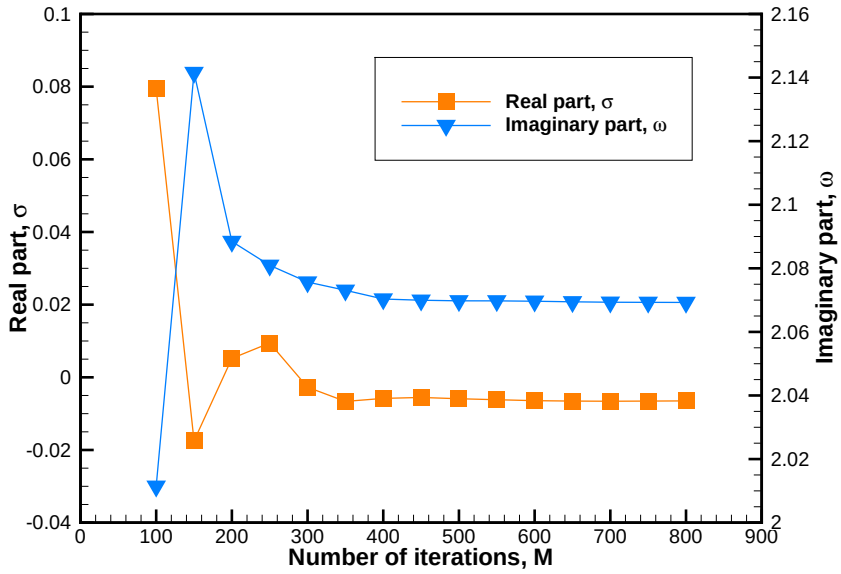

Figure 5.3: Convergence property of eigenvalue of the mode-I against the number of iterations M.

energy that the fluid received from the moving wall is transformed to thermal energy via viscous dissipation, and then the thermal energy is absorbed by the wall. Because of the long time scale of this process, the flowfield does not reach its steady state even at $t = 3000$. By this process, the effective Reynolds number of this flowfield is decreased with time (the density decreases with time in Fig. 5.5).

Temporal variations of the eigenvalues of the mode-I are shown in Fig. 5.6. The flowfields between $t = 1500$ and 3000 were used as basic states for this analysis. As time goes on and the dissipation process progresses (which results in the decrease of the effective Reynolds number), the real part of the eigenvalue decreases, namely the flowfield becomes more stable. On the other hand, the change of the imaginary part of the eigenvalue is small. The difference between the values at $t = 1000$ and 3000 is about 1%. The mode shape of the corresponding eigenvector at $t = 1000$ and $t = 3000$ are almost same (not shown here, they are similar distribution to Figs 5.14(f) and 5.15(f) shown later). Therefore, it is concluded that the qualitative properties of the mode-I do not change in time between $t = 1000$ and 3000, while the growth rate decreases.

The objective of this study is to elucidate the effect of compressibility on the global stability

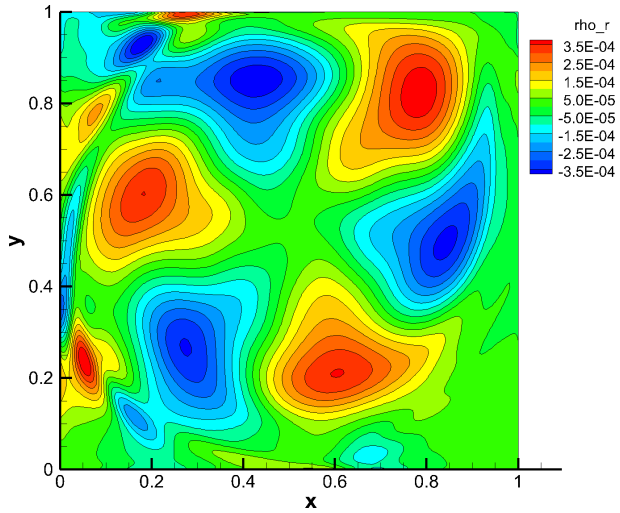

(a) $M = 300$

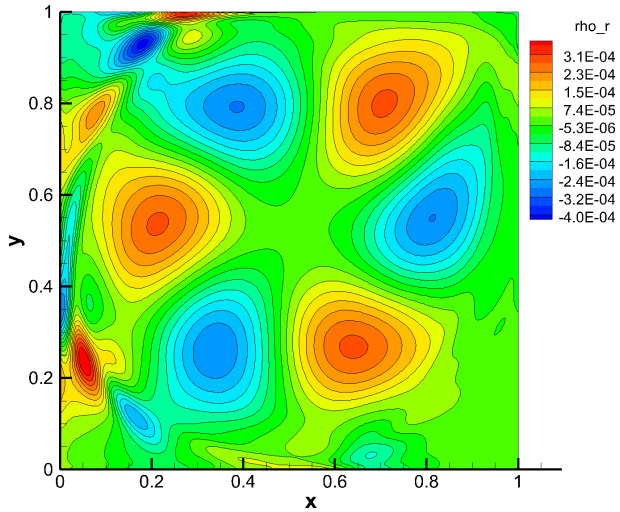

(b) $M = 500$

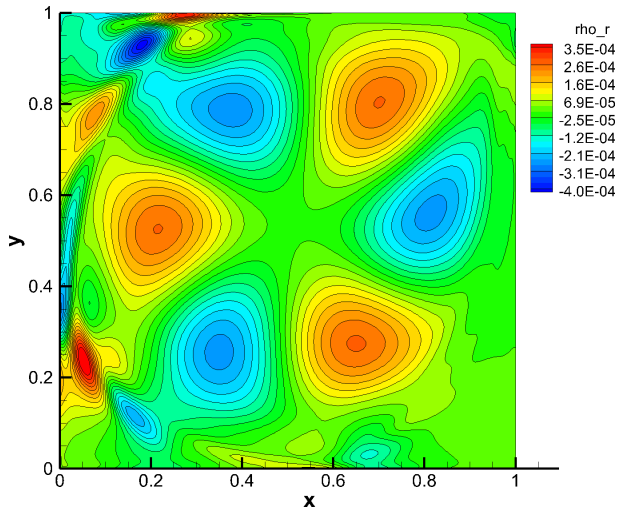

(c) $M = 800$

Figure 5.4: Density eigenvectors at $M = 300,\ 500$, and 800. Only the real part is shown.

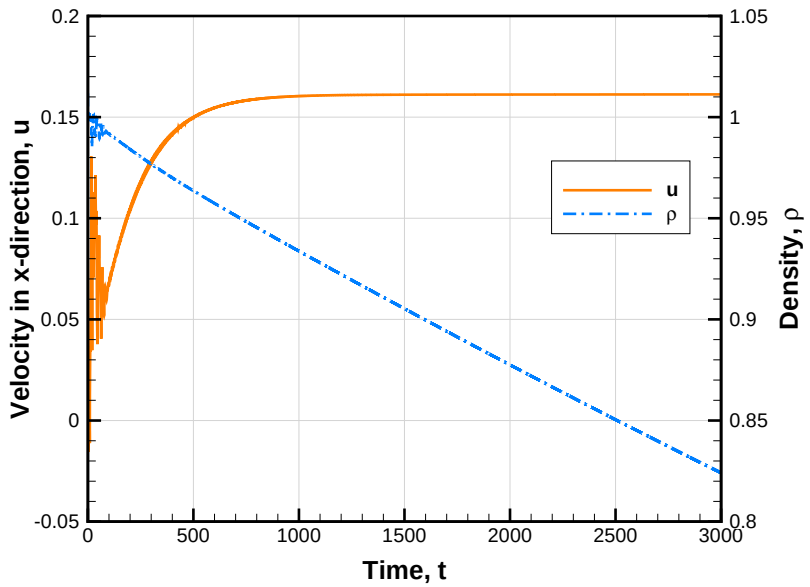

Figure 5.5: Time history of density ρ and velocity in x-direction u at $Re = 11000$, $Ma = 0.6$. Sampling point is $x/L = 0.5$, $y/L = 0.75$.

of vortical flows by observations of eigenmodes at various Mach numbers. Therefore, it is preferred that the effective Reynolds number of the flow do not change from the initial condition. In this study, the flowfield at the time $t = 1500$, when the velocity fields converge enough, is used as the basic state $\bar{\boldsymbol{q}}$.

5.3.2 Flowfields at low mach number

In this section, we confirm that the results of incompressible flow analysis conducted by Chiba[18, 19] can be reproduced by our compressible flow analysis at a low Mach number condition, and review the results of Chiba's analysis by comparing with our results.

Steady and periodic flows

Figure 5.7 shows the flowfield at $Ma = 0.05$ and $Re = 6000$. The flowfield is steady, and a main vortex at the central region and sub vortices at corners are generated by the moving wall. Previous studies[18, 19, 67] have showed that the critical Reynolds number Re_{cr} of this flow exists between 10000 and 10500. Our results also showed that the flowfield becomes a periodic flow from a steady flow when Reynolds number is larger than about 10000.

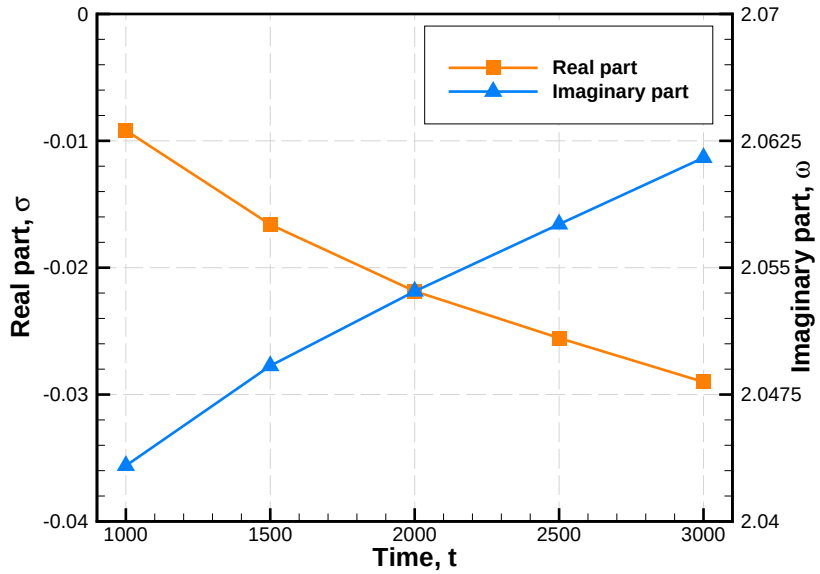

Figure 5.6: Temporal variation of the eigenvalue of the mode-I at $Re = 11000$, $Ma = 0.6$.

The frequency distribution of the velocity in x-direction of the unsteady flow at $Re = 10750$ is shown in Fig. 5.8. This result clearly indicates that the flow is oscillatory and has a single frequency $St \equiv fL/u_{max} = 0.33$. In this study, we conduct detailed analysis of this unstable mode which induces this oscillation.

Results of global linear stability analysis

The eigenvalue distribution at $Re = 10000$ obtained by the global linear stability analysis is shown in Fig. 5.9. The Strouhal number, which is calculated by $St = \omega/(2\pi)$, of the least stable oscillatory mode is 0.33. This Strouhal number coincides with that of the oscillatory flow at $Re = 10750$ shown in Fig. 5.8. Therefore, it is inferred that the oscillation of the flow is induced by this mode which is unstable when the Reynolds number is high enough. For convenience of explanations, we call this oscillatory mode (whose Strouhal number is about 0.33) the mode-I.

In addition, a following relation between relatively low stable modes in Fig. 5.9 can be found.

$$\omega_m = m \times 0.7 \qquad (m = 0, 1, 2, \cdots) \tag{5.14}$$

Chiba[18,19] also found this relation and he showed that eigenmodes of the regularized cavity flow can be classified into the following modes,

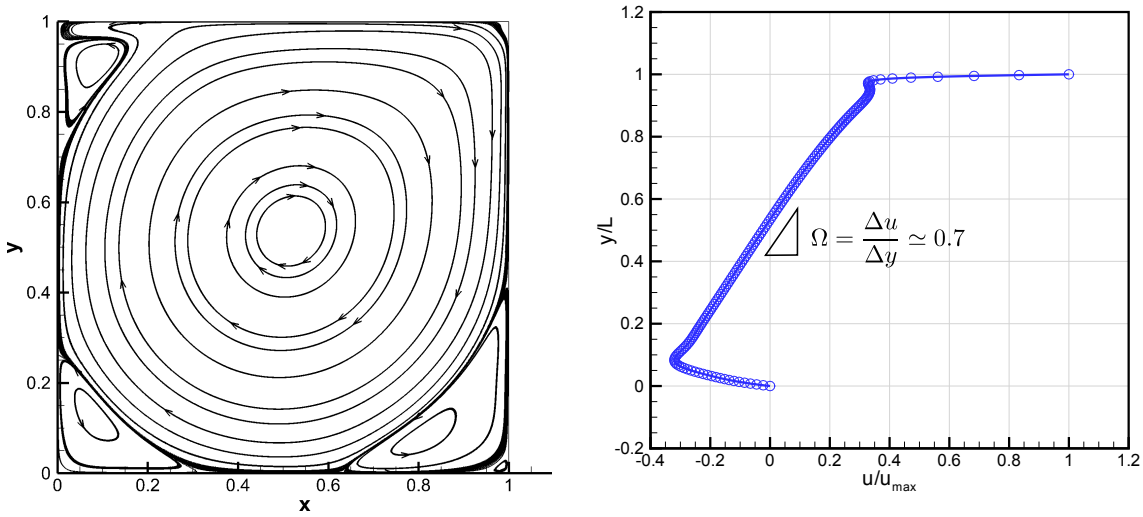

(a) Streamlines

(b) Distribution of the velocity u at $x/L = 0.5$

Figure 5.7: Steady flow at $Re = 6000$, $Ma = 0.05$, $t = 1500$.

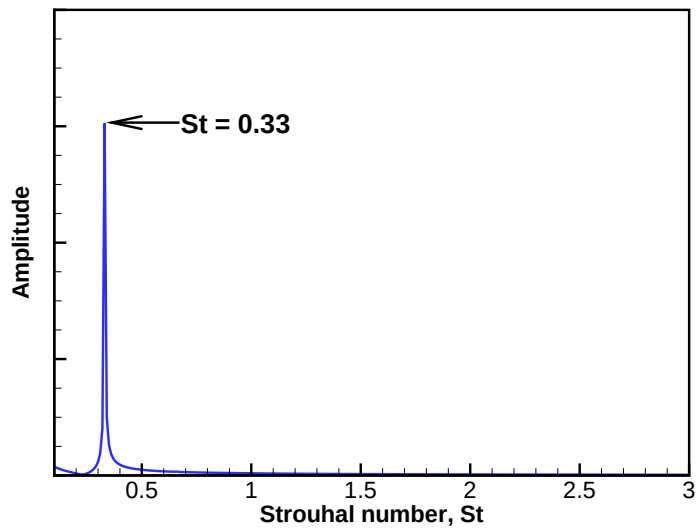

Figure 5.8: Frequency distribution of flowfield at $Re = 10750$, $Ma = 0.05$. Time history of velocity u at $x/L = 0.5$, $y/L = 0.75$ is used.

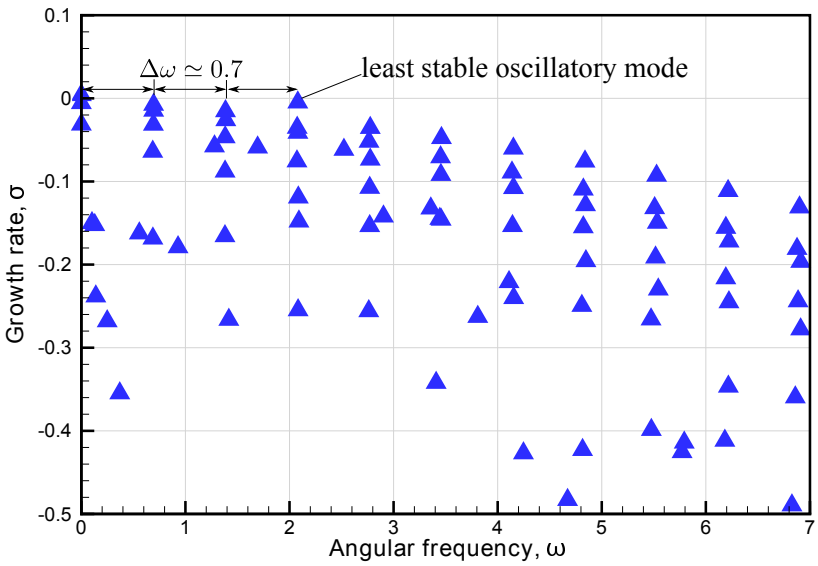

Figure 5.9: Eigenvalue distribution at $Re = 10000$, $Ma = 0.05$, $t = 1500$.

- Modes of inviscid Couette flows (C mode): This mode appears at the core region of the main vortex, where the velocity profile shows linear variation, in other words, the region of a constant vorticity.
- Modes of shear flows (S mode): This mode appears at the region of shear flows around the vortex core of the main vortex, where the velocity profile shows a curve with a significant change caused by the walls.

Moreover, he revealed that the relation of Eq. 5.14 can be explained as the C mode, as follows. In the case of an inviscid vortex whose vorticity is constant in the entire region of the flow, its eigenvectors and corresponding angular frequencies are described as follows,[18, 19, 68]

$$\varphi_{m,j} = C_0 \exp\left[i(\omega_m t + m\theta)\right] J_m(\alpha_{mj} r) \tag{5.15}$$

$$\omega_m = m\Omega \qquad (m = 0, 1, 2, \cdots) \tag{5.16}$$

where r and θ form the cylindrical coordinates (r, θ). $\varphi_{m,j}$ is an eigenvector of a stream function, m is a wavenumber in the circumferential direction, j is the number of nodal circles, J_m is the m-th order Bessel function, α_{mj} is the j-th solution of $J_m(x) = 0$, Ω is the vorticity, ω_m is the angular frequency, and C_0 is an arbitrary constant. The C mode has periodicity in circumferential

direction and the relation of its wavenumber and angular frequency is described by Eq. 5.16. In fact, the Strouhal number of the mode-I coincides with that of $(m, \Omega) = (3,\ 0.7)$, namely $St = \dfrac{\omega_3}{2\pi} = \dfrac{3 \times 0.7}{2\pi} \simeq 0.33$. Moreover, the vorticity of the core region of the main vortex is estimated to $\Omega \simeq 0.7$ by examining the velocity profile of Fig. 5.7(b) .

Characteristics of the mode-I

If an imaginary part of a eigenvalue has non zero value, the eigenmode periodically changes in time. This periodic change of the real part of the eigenvector is calculated by the following equation:

$$\hat{\boldsymbol{q}}(x, y, t) = C_0 \exp(\sigma t)\left[\hat{\boldsymbol{q}}_r(x, y)\cos(\omega t) - \hat{\boldsymbol{q}}_i(x, y)\sin(\omega t)\right] \tag{5.17}$$

where C_0 is an arbitrary constant. In order to observe the time variation of the mode-I, the eigenvector of the vorticity at $Re = 6000$ and 10000 are calculated by Eq. 5.17, and shown in Figs. 5.10 and 5.11. The coefficient $C_0 \exp(\sigma t)$ is set to 1, namely the growth (or damping) of the oscillation is ignored here for convenience.

In the case of $Re = 6000$, there is a periodical structure in the circumferential direction at the core region of the main vortex. This structure is caused by the C mode, and it is confirmed that the circumferential wavenumber is $m = 3$. In addition, the distribution of alternating vorticities caused by the S mode appears at the region of shear flows around the core region of the main vortex. These structures at the region of shear flow of $Re = 6000$ and 10000 are almost same. Therefore, these modes are believed to be the identical mode, namely the mode-I. However, in the case of $Re = 10000$, the structure of the C mode becomes weaker and the structure of the S mode becomes dominant. Consequently, the mode-I is the mode which is related to both of the instabilities of the core region of the main vortex (C mode) and the shear flow around the core region (S mode). In addition, the mode-I becomes unstable and induces the periodic oscillation of $St = 0.33$ to the flow due to the destabilization of the region of the shear flow as the Reynolds number increases.

The time sequential figures of the mode-I in Figs. 5.10 and 5.11 indicate that the structures of the C and S modes rotate in the same direction as the rotational direction of the main vortex. The angular frequency of the C mode toward the center of the main vortex is estimated to 0.7, and it is same as the vorticity of the main vortex. The angular frequency of the S mode is

estimated to 0.26 which is slower than that of the C mode. These results also agree very well with the results of the incompressible flow analysis conducted by Chiba.[18,19]

5.3.3 Changes of mode-I by Mach number

Figure 5.12 shows the change of the eigenvalue of the mode-I by the Mach and Reynolds numbers. In the case of all the Mach numbers, the stability of the mode-I decreases as the Reynolds number increases. On the other hand, the mode-I is stabilized as the Mach number increases. Especially, in the case of $Ma = 0.6$, the mode-I is highly stabilized, and the critical Reynolds number that is the Reynolds number at which the growth rate becomes positive, is high. Eigenvectors of the vorticity for various Reynolds numbers, at $Ma = 0.3$ and 0.6, are shown in Fig. 5.13. In the both cases of $Ma = 0.3$ and 0.6, structures of regions of shear flows (S mode) become more unstable as the Reynolds number increases, as well as the case of $Ma = 0.05$ discussed in Section 5.3.2. Figures. 5.14 and 5.15 show eigenvectors of the pressure and density for various Mach and Reynolds numbers. The change of pressure eigenvectors by the Reynolds number is similar to the change of the vorticity eigenvector. However, the magnitude of the pressure perturbation of this mode hardly changes by the Mach number.† In contrast, the density eigenvectors change by the Mach number. As the Mach number increases, the structures of the region of the shear flow (S mode) become dominant and its magnitudes become significantly large while this mode becomes stabilized. Therefore, it is inferred that the stabilizing effect of the increasing Mach number is caused by the density perturbation. In the next section, we investigate how the density perturbation stabilizes the mode-I.

5.3.4 Stabilizing effect of compressibility

In this section, the dynamics of vortices is considered, in order to clarify the stabilizing effect of the density perturbation. In two-dimensional compressible viscous flows, the spanwise vorticity ω_z is governed by the following vorticity equation:

$$\frac{D\omega_z}{Dt} = \underbrace{-\omega_z\left(\frac{\partial u}{\partial x} + \frac{\partial v}{\partial y}\right)}_{\text{vorticity}-\text{dilatation}} + \underbrace{\frac{1}{\rho^2}\left(\frac{\partial p}{\partial x}\frac{\partial \rho}{\partial y} - \frac{\partial p}{\partial y}\frac{\partial \rho}{\partial x}\right)}_{\text{baroclinic torque}} + \underbrace{\frac{1}{Re}\left(\frac{\partial^2 \omega_z}{\partial x^2} + \frac{\partial^2 \omega_z}{\partial y^2}\right)}_{\text{viscous diffusion}} \tag{5.18}$$

†The eigenvectors are normalized to unit length. Namely, $\sqrt{\hat{\boldsymbol{q}} \cdot \hat{\boldsymbol{q}}} = 1$. In addition, the number of elements of all the vectors in this section is same. Therefore, we can compare the magnitudes of the eigenvectors of different figures.

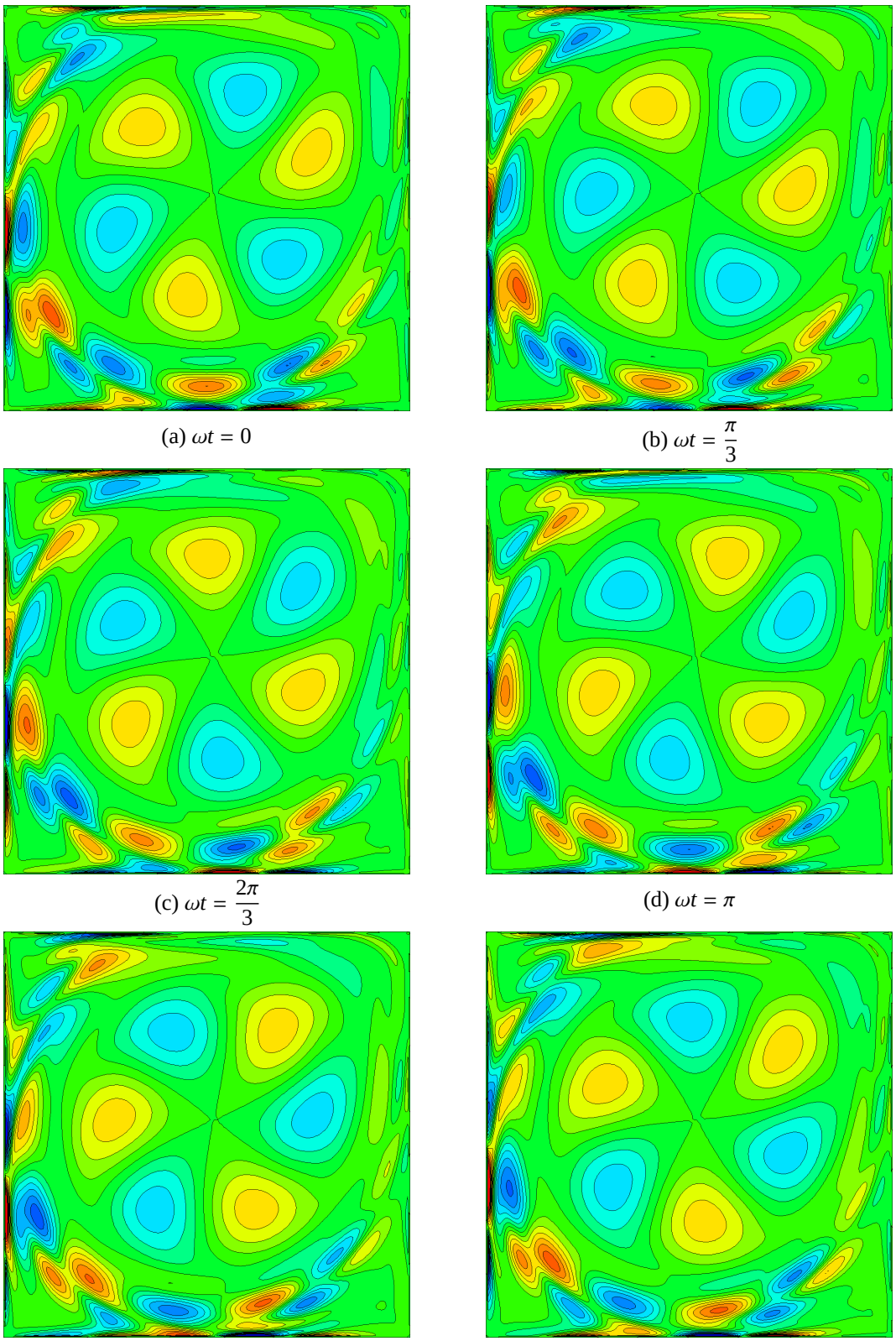

(a) $\omega t = 0$

(b) $\omega t = \frac{\pi}{3}$

(c) $\omega t = \frac{2\pi}{3}$

(d) $\omega t = \pi$

(e) $\omega t = \frac{4\pi}{3}$

(f) $\omega t = \frac{5\pi}{3}$

Figure 5.10: Temporal change of vorticity eigenvector at $Re = 6000$, $Ma = 0.05$. Eigenvalue λ is $\sigma = -4.73 \times 10^{-2}$, $\omega = 2.11$. Only the real part is shown.

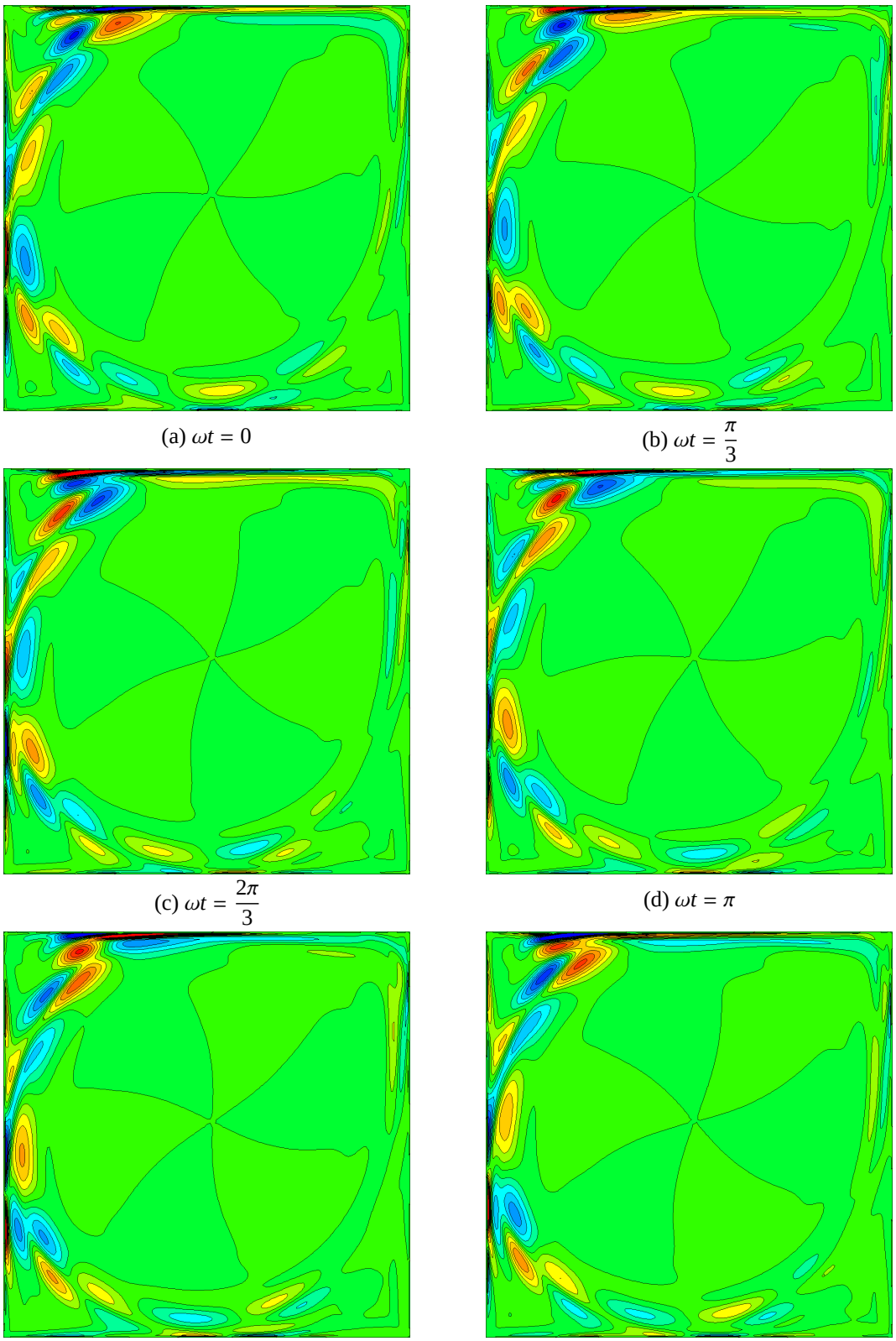

(a) $\omega t = 0$

(b) $\omega t = \frac{\pi}{3}$

(c) $\omega t = \frac{2\pi}{3}$

(d) $\omega t = \pi$

(e) $\omega t = \frac{4\pi}{3}$

(f) $\omega t = \frac{5\pi}{3}$

Figure 5.11: Temporal change of vorticity eigenvector at $Re = 10000, Ma = 0.05$. Eigenvalue λ is $\sigma = -4.86 \times 10^{-3}$, $\omega = 2.08$. Only the real part is shown.

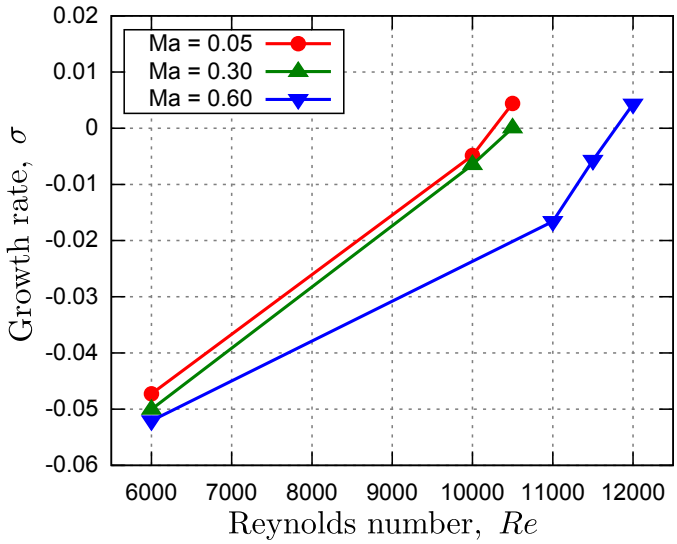

Figure 5.12: Changes in eigenvalues of the mode-I by Reynolds and Mach numbers.

where,

$$\omega_z \equiv \frac{\partial u}{\partial y} - \frac{\partial v}{\partial x} \tag{5.19}$$

$$\frac{D\omega_z}{Dt} \equiv \frac{\partial \omega_z}{\partial t} + u\frac{\partial \omega_z}{\partial x} + v\frac{\partial \omega_z}{\partial y} \tag{5.20}$$

The first term on the right hand side of Eq. 5.18 is a vorticity-dilatation term which represents an effect of dilatation and contraction of a vortex. If a vortex is contracted, its vorticity becomes large, and if the vortex is dilated, its vorticity becomes small. The second term is a baroclinic torque which represents the effect of misaligned gradients of the pressure and density. If there are misaligned gradients of the pressure and density, the unequal acceleration occurs and it results in a generation of the vorticity. These terms are caused by the density change. Therefore they indicate effects of the compressibility. The third term represents a dissipation effect of the viscosity.

Here, we consider distributions of the spanwise vorticity ω_z', the vorticity-dilatation term S'_{vd}, and the baroclinic torque S'_{bt} caused by perturbations $\boldsymbol{q}'$ superimposed on the basic state $\bar{\boldsymbol{q}}$.

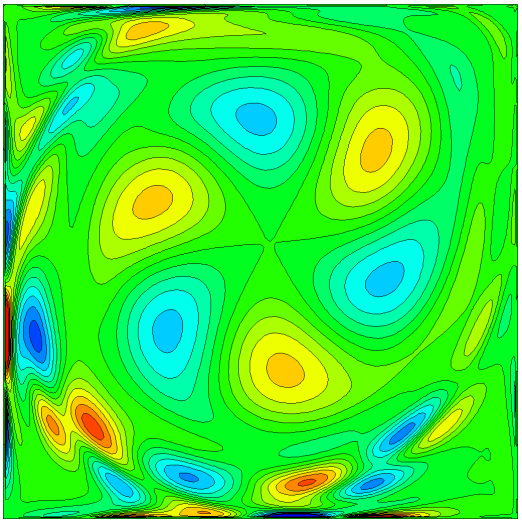

(a) $Ma = 0.3$, $Re = 6000$. Eigenvalue λ is $\sigma = -5.00 \times 10^{-2}$, $\omega = 2.09$

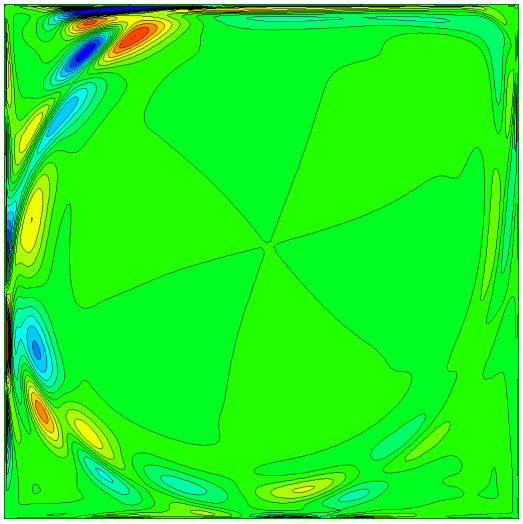

(b) $Ma = 0.3$, $Re = 10500$. Eigenvalue λ is $\sigma = 6.03 \times 10^{-5}$, $\omega = 2.07$

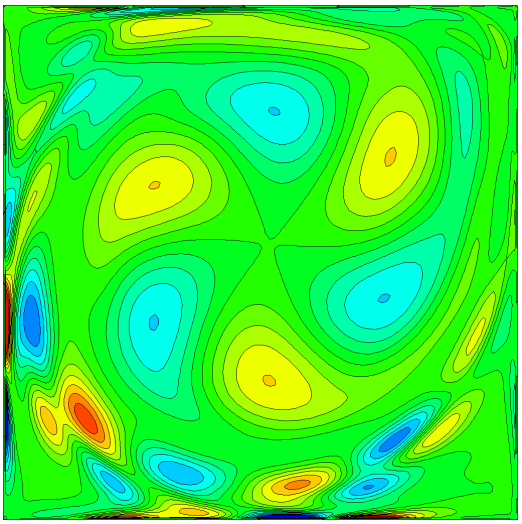

(c) $Ma = 0.6$, $Re = 6000$. Eigenvalue λ is $\sigma = -5.21 \times 10^{-2}$, $\omega = 2.05$

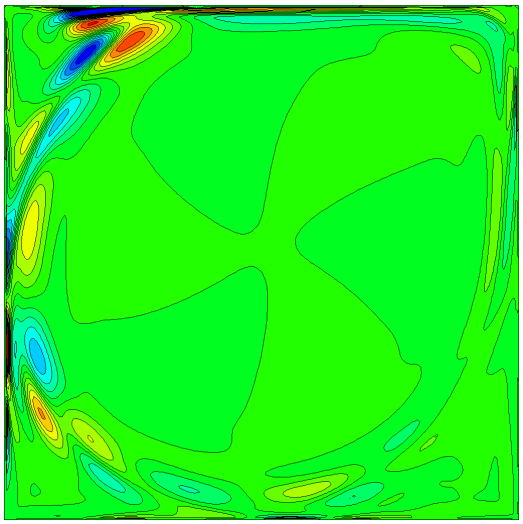

(d) $Ma = 0.6$, $Re = 12000$. Eigenvalue λ is $\sigma = 4.30 \times 10^{-3}$, $\omega = 2.04$

Figure 5.13: Changes in vorticity eigenvectors of the mode-I by Reynolds and Mach numbers. Only the real part is shown.

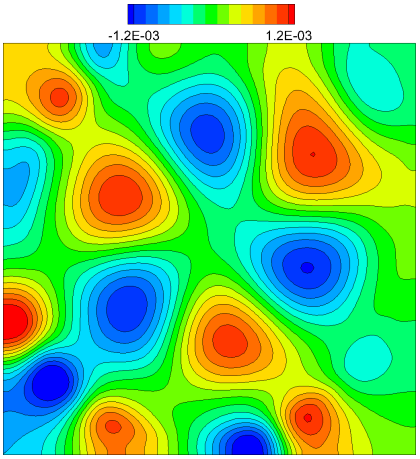

(a) $Ma = 0.05$, $Re = 6000$. Eigenvalue λ is $\sigma = -4.73 \times 10^{-2}$, $\omega = 2.11$

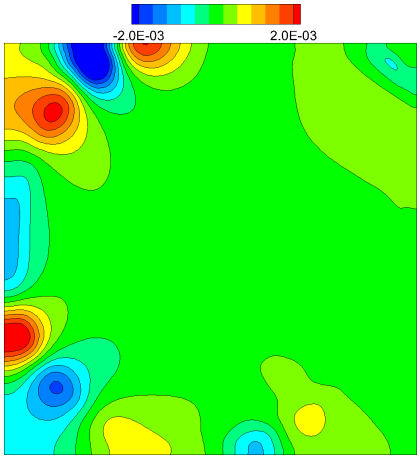

(b) $Ma = 0.05$, $Re = 10500$. Eigenvalue λ is $\sigma = 4.41 \times 10^{-3}$, $\omega = 2.08$

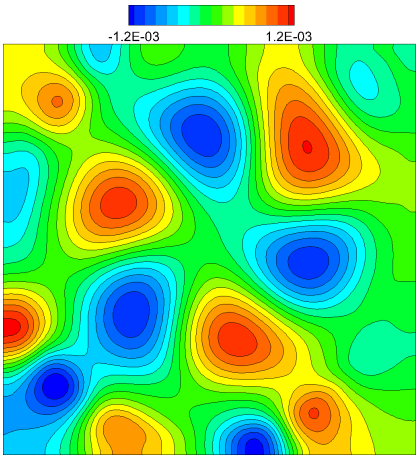

(c) $Ma = 0.3$, $Re = 6000$. Eigenvalue λ is $\sigma = -5.00 \times 10^{-2}$, $\omega = 2.08$

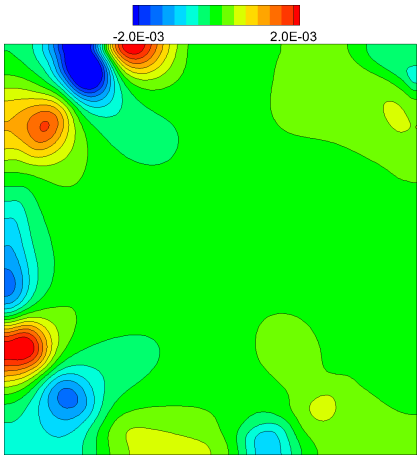

(d) $Ma = 0.3$, $Re = 10500$. Eigenvalue λ is $\sigma = 6.03 \times 10^{-5}$, $\omega = 2.07$

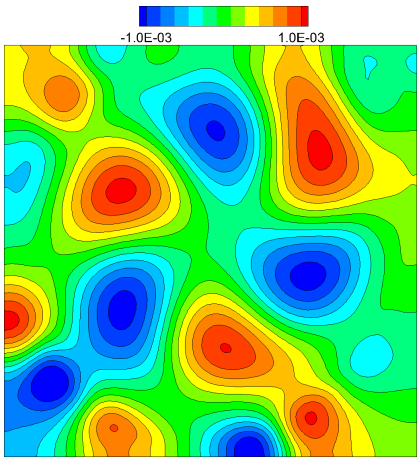

(e) $Ma = 0.6$, $Re = 6000$. Eigenvalue λ is $\sigma = -5.21 \times 10^{-2}$, $\omega = 2.05$

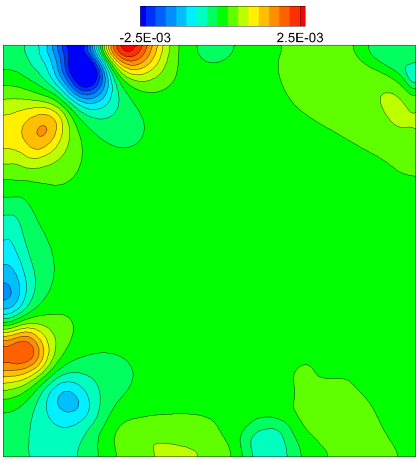

(f) $Ma = 0.6$, $Re = 12000$. Eigenvalue λ is $\sigma = 4.30 \times 10^{-3}$, $\omega = 2.04$

Figure 5.14: Changes in pressure eigenvectors of the mode-I by Reynolds and Mach numbers. Only the real part is shown.

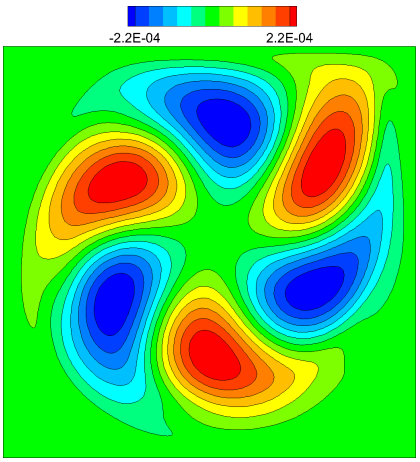

(a) $Ma = 0.05$, $Re = 6000$. Eigenvalue λ is $\sigma = -4.73\times10^{-2}$, $\omega = 2.11$

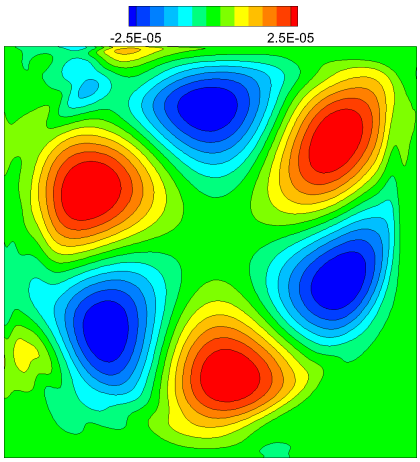

(b) $Ma = 0.05$, $Re = 10500$. Eigenvalue λ is $\sigma = 4.41 \times 10^{-3}$, $\omega = 2.08$

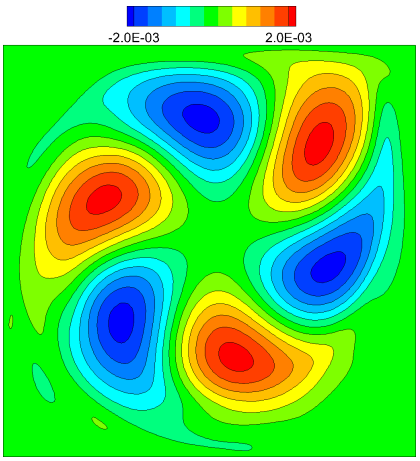

(c) $Ma = 0.3$, $Re = 6000$. Eigenvalue λ is $\sigma = -5.00 \times 10^{-2}$, $\omega = 2.08$

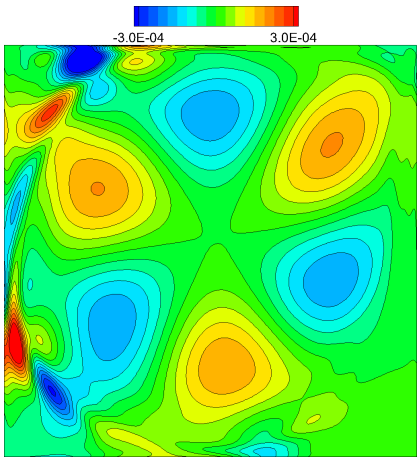

(d) $Ma = 0.3$, $Re = 10500$. Eigenvalue λ is $\sigma = 6.03 \times 10^{-5}$, $\omega = 2.07$

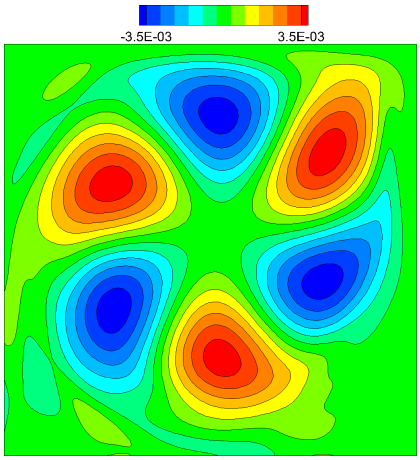

(e) $Ma = 0.6$, $Re = 6000$. Eigenvalue λ is $\sigma = -5.21 \times 10^{-2}$, $\omega = 2.05$

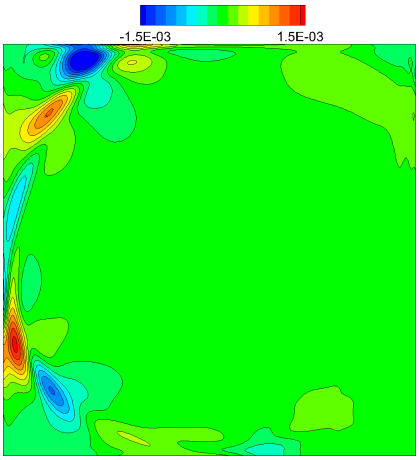

(f) $Ma = 0.6$, $Re = 12000$. Eigenvalue λ is $\sigma = 4.30 \times 10^{-3}$, $\omega = 2.04$

Figure 5.15: Changes in density eigenvectors of the mode-I by Reynolds and Mach numbers. Only the real part is shown.

These terms generated by the perturbations are indicated by the following equations:

$$\omega_z' = \frac{\partial u'}{\partial y} - \frac{\partial v'}{\partial x} \tag{5.21}$$

$$S_{vd}' = -\bar{\omega}_z\left(\frac{\partial u'}{\partial x} + \frac{\partial v'}{\partial y}\right) - \omega_z'\left(\frac{\partial \bar{u}}{\partial x} + \frac{\partial \bar{v}}{\partial y}\right) \tag{5.22}$$

$$S_{bt}' = \frac{1}{\bar{\rho}^2}\left(\frac{\partial \bar{p}}{\partial x}\frac{\partial \rho'}{\partial y} - \frac{\partial \bar{p}}{\partial y}\frac{\partial \rho'}{\partial x} + \frac{\partial p'}{\partial x}\frac{\partial \bar{\rho}}{\partial y} - \frac{\partial p'}{\partial y}\frac{\partial \bar{\rho}}{\partial x}\right) \tag{5.23}$$

where, the overbar and prime denote variables of the basic state and perturbations, respectively. These terms ω_z', S_{vd}', and S_{bt}' caused by the linear instability of the mode-I are calculated by substituting the eigenvector $\hat{\boldsymbol{q}}$ into $\boldsymbol{q}'$. Distributions of the ω_z', S_{vd}', and S_{bt}' at close to the critical Reynolds number, are shown in Figs. 5.16 and 5.17 for $Ma = 0.05$ and 0.6, respectively.

At both Mach numbers of 0.05 and 0.6, the effect of dilatation (indicated by the vorticity-dilatation term S_{vd}') is found in the region of shear flows, and its distribution is similar to the spanwise vorticity ω_z' (the alternating distribution). In addition, the vorticity-dilation term has the opposite signs to the spanwise vorticity in many regions. This means that he vorticity-dilatation term attenuates vorticity perturbations. It has been known that this stabilizing effect of the vorticity-dilatation term also appears in a compressible mixing layer.[8]

At $Ma = 0.05$, the magnitude of the baroclinic torque S_{bt}' is much smaller than that of the vorticity-dilatation term, and therefore negligible. In contrast, at $Ma = 0.6$, the baroclinic torque has the comparable magnitude to the vorticity-dilatation term. The baroclinic torque distributes to the region of shear flows and has large values especially near reattachment points of the base flow $\bar{q}$. The distribution of this term does not form the alternating distribution unlike the spanwise vorticity and the vorticity-dilatation term. It is inferred that the spanwise vortices are deformed to elongated shapes by this baroclinic torque distribution.

The mode-I can be considered as an incompressible instability mode because it appears in low Mach number flows, and therefore it is inferred that the alternating distribution of vortices, which sustains the vortices themselves like the Kármán vortex-street, is important to destabilize the mode-I. Therefore, the above deformation effect on the spanwise vorticies of the baroclinic torque results in the stabilization of the mode-I, because it breaks such alternating distributions of vorticies. Moreover, the difference between the low Mach number flow ($Ma = 0.05$) and the higher Mach number flow ($Ma = 0.6$) is the magnitude of the baroclinic torque. Thus, it is concluded that the stabilization of the mode-I with the increasing Mach number is caused by

the baroclinic torque which deforms the spanwise vortices.

5.4 Summary

In this chapter, in order to elucidate effects of compressibility on the global stability of the cavity vortex, the global linear stability analyses of the compressible regularized cavity flow for various Mach and Reynolds numbers were conducted.

The result of the global linear stability analysis at the low Mach number condition shows good agreement with the results of incompressible flow analysis conducted by Chiba.[18, 19] It is summarized as follows:

- The flowfield becomes an oscillatory flow when the Reynolds number exceeds a certain value (about $Re = 10000$).
- The oscillation is caused by a linear instability mode (called mode-I in this study).
- Linear instability of the regularized cavity flow can be classified into two modes, namely the C and S modes. The C mode relates to instability of a inviscid vortex and exists in the core region of the main vortex. The S mode relates to instability of shear flows and exists in outer regions of the core region of the main vortex.
- The mode-I has the instability nature of both of the C and S mode.
- Instability of the S mode becomes unstable and dominant as the Reynolds number increases.

Then, we analyzed the effect of the compressibility on instability of the mode-I. We compared the eigenvectors of the mode-I for various Mach numbers. In addition, we investigated the distributions of two terms of the vorticity transport equation, namely, the baroclinic torque and the vorticity-dilatation term which describe compressibility effects.

- Density perturbations in the region of shear flows become significant as the Mach number increases, whereas the velocity and pressure perturbations do not change significantly.
- In the region of shear flows, the vorticity-dilatation term attenuates spanwise vortices, namely,this term has stabilizing effect. This result is similar to results of previous study on a compressible mixing layer.[8]

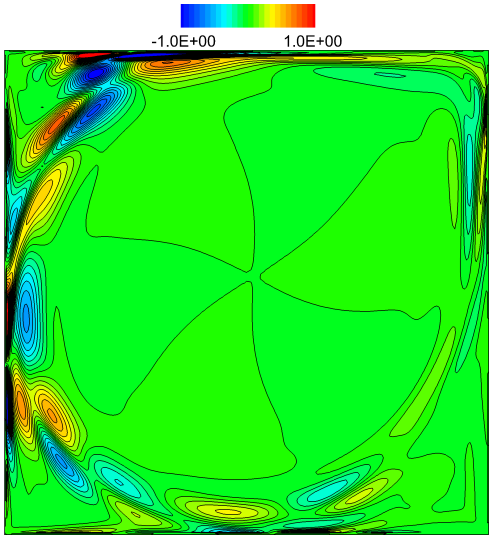

(a) Spanwise vorticity ω_z'

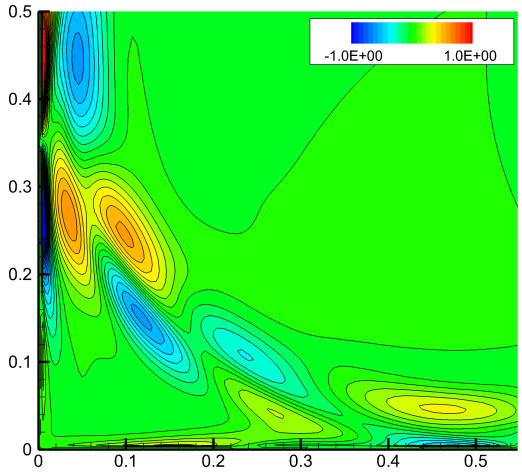

(b) Closeup view of spanwise vorticity ω_z'

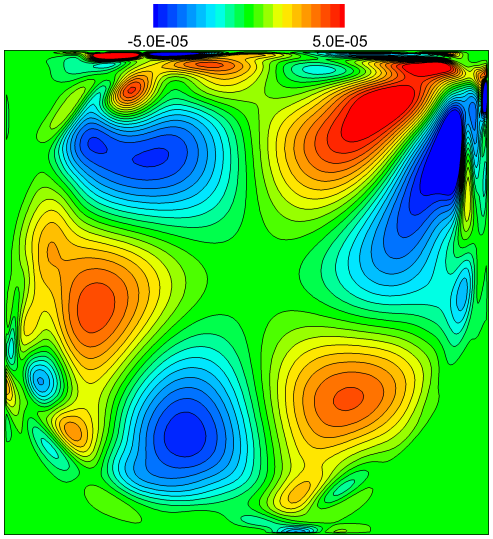

(c) Baroclinic torque S'_{bt}

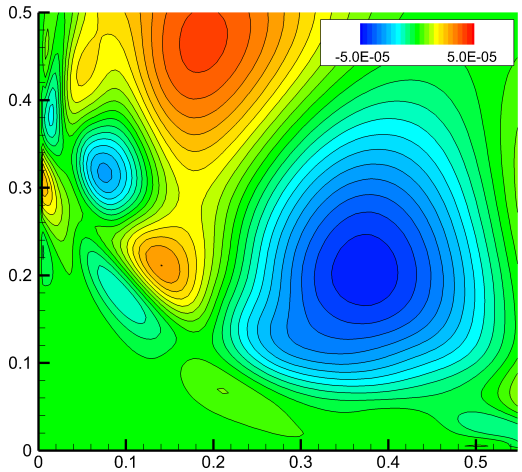

(d) Closeup view of baroclinic torque S'_{bt}

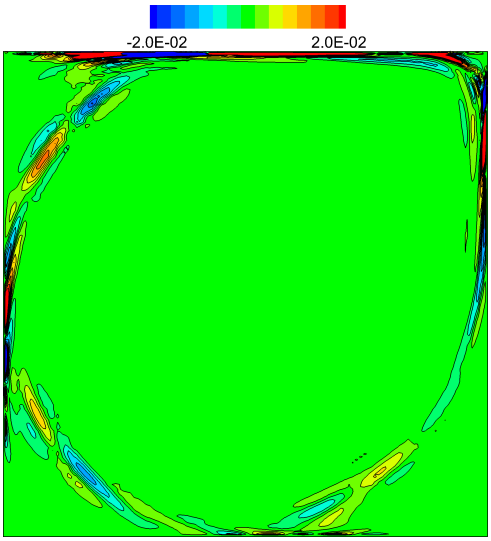

(e) Vorticity-dilatation term S'_{vd}

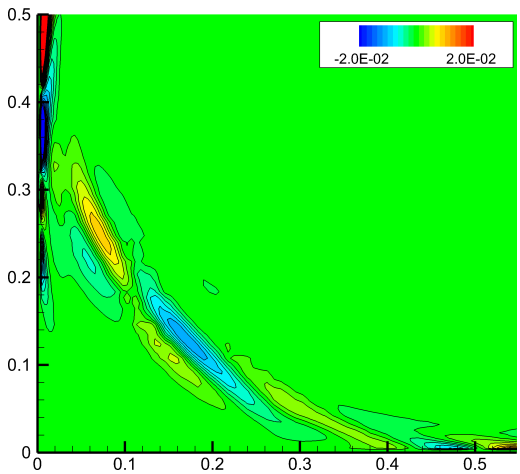

(f) Closeup view of vorticity-dilatation term S'_{vd}

Figure 5.16: Distributions of ω_z', S'_{bt}, and S'_{vd}. $Ma = 0.05$, $Re = 10500$.

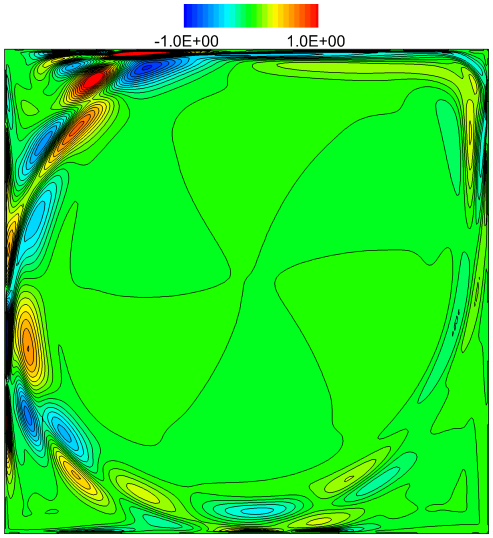

(a) Spanwise vorticity ω_z'

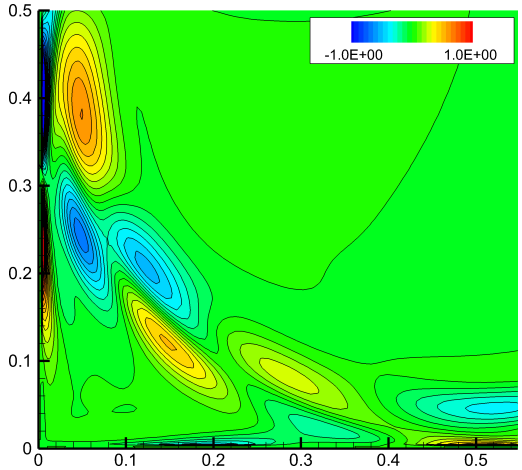

(b) Closeup view of spanwise vorticity ω_z'

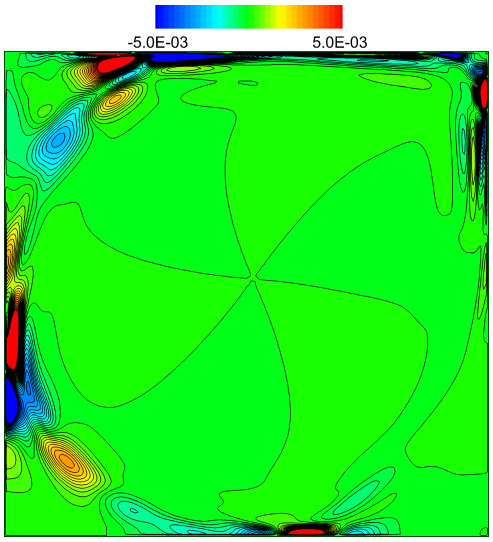

(c) Baroclinic torque S_{bt}'

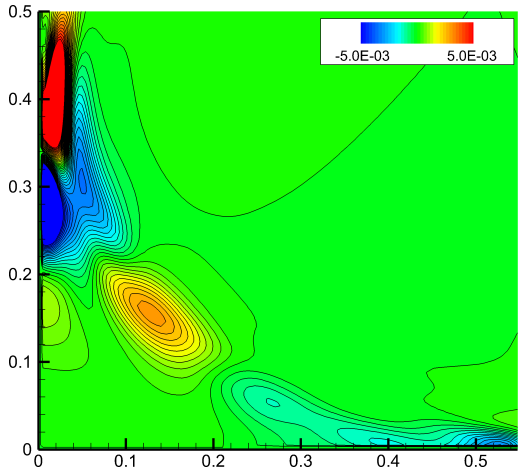

(d) Closeup view of baroclinic torque S_{bt}'

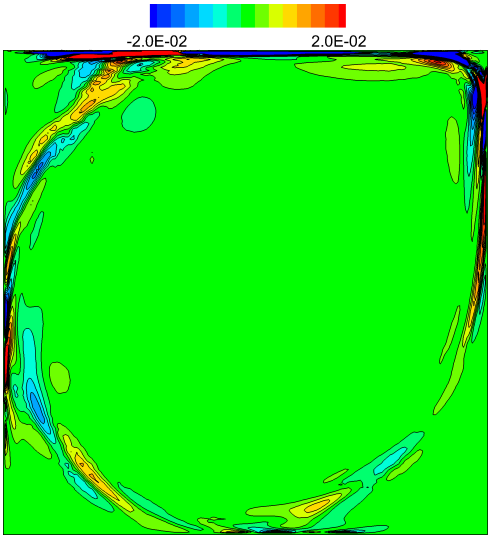

(e) Vorticity-dilatation term S_{vd}'

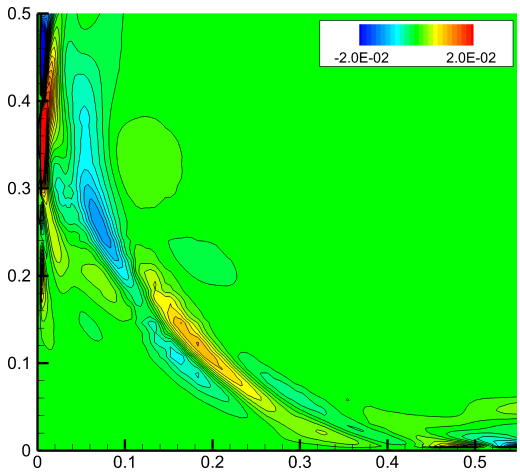

(f) Closeup view of vorticity-dilatation term S_{vd}'

Figure 5.17: Distributions of ω_z', S_{bt}', and S_{vd}'. $Ma = 0.6$, $Re = 12000$.

- The magnitude of the baroclinic torque becomes large as the Mach number increases, while that of the vorticity-dilatation term does not greatly change.
- In the region of shear flows, the baroclinic torque deforms spanwise vortices to elongated shapes.
- In conclusion, the stabilizing effect of the compressibility on the cavity vortex is caused by the increase of the deformation effects of the baroclinic torque.

Finally, it should be emphasized that the above results are achieved by the global linear stability analysis which is able to analyze the global stability of non-parallel, compressible, and viscous flows.

6 Conclusions

The results of this thesis are summarized as follows:

High-resolution and matrix-free method of the global linear stability analysis for compressible viscous flows

In Chapter 4, we discussed about the desired properties of the numerical method for the future global linear stability analysis, and proposed the method that satisfies the properties.

First, we discussed about two spectral transformation methods, namely, the time-stepping method and the shift-invert method. In terms of computational time cost, the time-stepping method can be more computationally expensive than the shift-invert method, because the time-stepping method needs to solve the time development of fluids. By contrast, the time-stepping method needs considerably less computational memory than the shift-invert method, because the time-stepping method does not form any matrix explicitly, namely, this method is matrix-free. The memory requirement of the shift-invert method is proportional to the square of dimensions of the Jacobian matrix $\boldsymbol{A}$, since this method forms the matrix $\boldsymbol{A}$ explicitly. Therefore, the memory requirement of the shift-invert method readily exceeds the available memory of the computer when the number of computational grid points for fluid simulations is large, which leads a large dimension of the Jacobian matrix $\boldsymbol{A}$. Especially in the case of three-dimensional flow analysis, it might be crucial. In addition, to write the code of the time-stepping method is easy because the routine of conventional CFD codes is used. Therefore, we concluded that the time-stepping method is promising for future studies that analyze three-dimensional flows.

Next, we proposed and validated the numerical method of the global linear stability analysis for compressible viscous flows that has the high-order spatial accuracy and uses a matrix-free method. We consider that the high-order spatial accuracy and the low memory requirement are necessary properties of the method for future global linear stability analyses because future

studies are believed to treat small spatial structures and perturbations such as the aeroacoustics and turbulent flows. The proposed method uses the time-stepping method as the spectral transformation method and the compact difference scheme as the method for fluid simulations. Therefore, the proposed method has good properties of the compact difference scheme and the time-stepping method, namely, the high-order spatial accuracy and the low memory requirement, as well as the applicability to various equations and the simplicity of the coding.

Then, for the validation of the proposed method, two-dimensional compressible viscous flows past a circular cylinder was analyzed by this method. The results showed good agreement with previous studies. The superimposition of the most unstable mode and the steady state depicted the flowfield that includes the Kármán vortex-street. In addition, effects of an outflow boundary was investigated. It was found that the global linear stability analysis is affected by an outflow boundary and the influence can be avoided by proper boundary conditions such as a non-reflecting boundary condition and to locate the boundaries far from a body.

Finally, we investigated the applicability of the proposed method for flowfields including shock waves. The applicability of the global linear stability analysis for the flowfields including shock waves has not been investigated before. This study analyzed a global linear stability of a supersonic flowfield around a circular cylinder. We confirmed that the proposed method can analyze the global linear stability of wake flows behind the cylinder. Consequently, it was found that the proposed method is able to analyze global linear stability of supersonic flows including shock waves. However, the global linear stability analysis of flowfields including shock waves needs to be paid attention to a numerical instability due to shock waves.

Compressibility effects on the global linear stability of a vortex

In Chapter 5, to elucidate compressibility effects on the global linear stability of a vortex, the compressible cavity vortex was investigated by the method of global linear stability analysis proposed in Chapter 4.

First, it was confirmed that the results of the global linear stability analysis of incompressible cavity flows are reproduced by our analysis of the compressible cavity flow. The instability of the cavity vortex is classified into two modes, namely, C and S modes which relate to an inviscid vortex located in the core region of the main vortex and a shear flow located in the

outer region of the inviscid vortex, respectively. The cavity flow becomes an oscillatory flow when the Reynolds number exceeds a certain value. This oscillatory flow is caused by a linear instability mode called the mode-I in this study. The mode-I is related to both of the C and S modes, and the S mode, namely, the instability of shear flows rapidly grows and becomes unstable as the Reynolds number increases.

Then, we revealed the stabilizing effects of the compressibility on the cavity vortex by comparisons of the eigenmodes at various Mach number conditions. The global linear stability analysis showed that the mode-I becomes stable as the Mach number increases. The eigenvector results indicated the density perturbation becomes significant as the Mach number increases, whereas the velocity (vorticity) and pressure perturbations do not so greatly change. In addition, the further investigations on the compressibility effect was conducted by analyzing the distributions of the vorticity-dilatation and the baroclinic torque terms of the vorticity transport equation. These terms indicate the compressibility effect on the generation of spanwise vortices. It was found that the vorticity-dilatation term attenuates spanwise vortices in the region of shear flows. In other words, the dilatation has a stabilizing effect. It has been known that this stabilizing effect of the vorticity-dilatation term also appears in a compressible mixing layer. However, the magnitude of the vorticity-dilatation do not so greatly change by the Mach number. We revealed that in contrast to the vorticity-dilatation term, the magnitude of baroclinic torque becomes large as the Mach number increases, and the baroclinic torque deforms spanwise vortices generated in the region of shear flows to elongated shapes. Therefore, it is concluded that the stabilizing effect of the compressibility on the cavity vortex is caused by the increase of the deformation effects of the baroclinic torque.

Concluding remarks

In conclusion, this thesis developed the promising method of the global linear stability analysis for compressible viscous flows, and revealed the stabilizing effect of compressibility on vortical flows by using the developed method. The results of this thesis show that the global linear stability analysis is a helpful analytical method for understanding transition and unsteady phenomena.

References

[1] O. Reynolds. An experimental investigation of the circumstances which determine whether the motion of water in parallel channels shall be direct or sinuous and of the law of resistance in parallel channels. *Philosophical Transactions of the Royal Society of London*, Vol. 174, pp. 935–982, 1883.

[2] F. Gomez, J. H. Quesada, R. Gomez, V. Theofilis, B. Carmo, and J. Meneghini. Stability analysis of the flow around a cylinder fitted with helical strakes. AIAA Paper 2013-2987, 2013.

[3] D. W. Bogdanoff. Compressibility effects in turbulent shear layers. *AIAA Journal*, Vol. 21, No. 6, pp. 926–927, 1983.

[4] N. Chinzei, G. Masuya, T. Komuro, A. Murakami, and K. Kudou. Spreading of two-stream supersonic turbulent mixing layers. *Physics of Fluids*, Vol. 29, No. 5, pp. 1345–1347, 1986.

[5] D. Papamoschou and A. Roshko. The turbulent compressible shear layer: An experimental study. *Journal of Fluid Mechanics*, Vol. 197, pp. 453–477, 1988.

[6] S. A. Ragab and J. L. Wu. Instabilities in the free shear layer formed by two supersonic streams. AIAA Paper 1988-3538, 1988.

[7] N. T. Clements and M. G. Mungal. Two- and three-dimensional effects in the supersonic mixing layer. *AIAA Journal*, Vol. 30, No. 4, pp. 973–981, 1992.

[8] N. D. Sandham and W. C. Reynolds. Compressible mixing layer - Linear theory and direct simulation. *AIAA Journal*, Vol. 28, No. 4, pp. 618–624, 1990.

[9] N. D. Sandham and W. C. Reynolds. Three-dimensional simulations of large eddies in the compressible mixing layer. *Journal of Fluid Mechanics*, Vol. 224, pp. 133–158, 1991.

[10] S. S. Collis, R. D. Joslin, A. Seifert, and V. Theofilis. Issues in active flow control: theory, control, simulation, and experiment. *Progress in Aerospace Sciences*, Vol. 40, pp. 237–289, 2004.

[11] V. Theofilis and T. Colonius. Special issue on global flow instability and control. *Theoretical and Computational Fluid Dynamics*, 2011.

[12] G. A. Bres and T. Colonius. Three-dimensional linear stability analysis of cavity flows. AIAA Paper 2007-1126, 2007.

[13] G. A. Bres and T. Colonius. Three-dimensional instabilities in compressible flow over open cavities. *Journal of Fluid Mechanics*, Vol. 599, pp. 309–339, 2008.

[14] P. Meliga, D. Sipp, and J.-M. Chomaz. Effect of compressibility on the global linear stability of axisymmetric wake flows. *Journal of Fluid Mechanics*, Vol. 660, pp. 499–526, 2010.

[15] C. J. Mack, P. J. Schmid, and J. L. Sesterhenn. Global stability of swept flow around a parabolic body: connecting attachment-line and crossflow modes. *Journal of Fluid Mechanics*, Vol. 611, pp. 205–214, 2008.

[16] J. D. Couch, A. Garbaruk, and D. Magidov. Predicting the onset of flow unsteadiness based on global instability. *Journal of Computational Physics*, Vol. 224, No. 2, pp. 924–940, 2007.

[17] J. D. Crouch, A. Garbaruk, D. Magidov, and A. Travin. Origin of transonic buffet on aerofoils. *Journal of Fluid Mechanics*, Vol. 628, pp. 357–369, 2009.

[18] 千葉賢. 非圧縮性粘性流体の全体安定性の数値的研究. PhD thesis, 東京大学工学研究科（航空宇宙工学）, 1997.

[19] 千葉賢. 非圧縮性粘性流体の全体安定性解析. 日本数値流体力学会誌, Vol. 7, No. 1, pp. 20–48, 1998.

[20] L. E. Eriksson and A. Rizzi. Computer-aided analysis of the convergence to steady state of discrete approximations to the euler equations. *Journal of Computational Physics*, Vol. 57, No. 1, pp. 90–128, 1985.

[21] 竹内伸太郎, 三宅裕, 梶島岳夫. 全体安定性解析による円形噴流の崩壊過程の解析. 日本機械学会論文集（B 編）, Vol. 68, No. 665, 2002.

[22] A. Tezuka and K. Suzuki. Three-dimensional global linear stability analysis of flow around a spheroid. *AIAA Journal*, Vol. 44, No. 8, pp. 1697–1708, 2006.

[23] J. W. Nichols and S. K. Lele. Global modes and transient response of a cold supersonic jet. *Journal of Fluid Mechanics*, Vol. 669, pp. 225–241, 2011.

[24] S. Bagheri, E. Åkerbik, L. Bandt, and D. S. Henningson. Matrix-free methods for the stability and control of boundary layers. *AIAA Journal*, Vol. 47, No. 5, pp. 1057–1068, May 2009.

[25] S. Bagheri, P. Schlatter, P. J. Schmid, and D. S. Henningson. Global stability of a jet in crossflow. *Journal of Fluid Mechanics*, Vol. 624, pp. 33–44, 2009.

[26] V. Theofilis. Global linear instability. *Annual Review of Fluid Mechanics*, Vol. 43, pp. 319–352, 2011.

[27] F. Gómez, S. Le Clainche, P. Paredes, M. Hermanns, and V. Theofilis. Four decades of studying global linear instability: Progress and challenges. *AIAA Journal*, Vol. 50, No. 12, pp. 2731–2743, December 2012.

[28] D. A. Knoll. and D. E. Keyes. Jacobian-free Newton-Krylov methods: a survey of approaches and applications. *Journal of Computational Physics*, Vol. 193, pp. 357–397, 2004.

[29] W. E. Arnoldi. The principle of minimized iterations in the solution of the matrix eigenvalue problem. *Quarterly of Applied Mathematics*, Vol. 9, pp. 17–29, 1951.

[30] H. A. van der Vorst. Bi-CGSTAB: A fast and smoothly converging variant of Bi-CG for the solution of nonsymmetric linear systems. *SIAM Journal on Scientific and Statistical Computing*, Vol. 13, No. 2, pp. 631–644, 1992.

[31] Y. Saad. and M. H. Schultz. GMRES: A generalized minimal residual algorithm for solving nonsymmetric linear systems. *SIAM Journal on Scientific and Statistical Computing*, Vol. 7, No. 3, pp. 856–869, 1986.

[32] O. Schenk, K. Gärtner, W. Fichtner, and A. Stricker. PARDISO: a high-performance serial and parallel sparse linear solver in semiconductor device simulation. *Future Generation Computer Systems*, Vol. 18, No. 1, pp. 69 – 78, 2001.

[33] S. K. Lele. Compact finite difference schemes with spectral-like resolution. *Journal of Computational Physics*, Vol. 103, No. 1, pp. 16–42, 1992.

[34] D. V. Gaitonde and M. R. Visbal. High-order schemes for navier-stokes equations: Algorithm and implementation into FDL3DI. Technical report, Air Force Research Laboratory, 1998.

[35] M. R. Visbal and D. V. Gaitonde. On the use of higher-order finite-difference schemes on curviliner and deforming meshes. *Journal of Computational Physics*, Vol. 181, pp. 155–185, 2002.

[36] S. Kawai and S. K. Lele. Localized artificial diffusivity scheme for discontinuity capturing on curvilinear meshes. *Journal of Computational physics*, Vol. 227, pp. 9498–9526, 2008.

[37] S. Kawai., S. K. Shankar., and S. K. Lele. Assessment of localized artificial diffusivity scheme for large-eddy simulation of compressible turbulent flows. *Jounal of Computational Physics*, Vol. 229, pp. 1739–1762, 2010.

[38] A. W. Cook. Artificial fluid properties for large-eddy simulation of compressible turbulent mixing. *Physics of Fluids*, Vol. 19, No. 5, p. 055103, 2007.

[39] A. W. Cook. A high-wavenumber viscosity for high-resolution numerical method. *Journal of Computational Physics*, Vol. 195, No. 2, pp. 594–601, 2004.

[40] F. Ducros., V. Ferrand., F. Nicoud., C. Weber., D. Darracq., C. Gacherieu., and T. Poinsot. Large-eddy simulation of the shock/turbulence interaction. *Journal of Computational Physics*, Vol. 152, No. 2, pp. 517–549, 1999.

[41] 嶋英志. 低マッハ数で誤差の小さい圧縮性 CFD 手法について. 第 40 回流体力学講演会／航空宇宙数値シミュレーション技術シンポジウム講演集, pp. 71–74, 2008.

[42] E. Shima and K. Kitamura. Parameter-free simple low-dissipation AUSM-family scheme for all speeds. *AIAA Journal*, Vol. 49, No. 8, pp. 1693–1709, August 2011.

[43] M.-S. Liou and C. Steffen. A new splitting scheme. *Journal of Computational Physics*, Vol. 107, pp. 23–39, 1993.

[44] B. van Leer. Toward the ultimate conservative difference scheme. 4, a new approach to numerical convection. *Journal of Computational Physiscs*, Vol. 23, pp. 276–299, 1977.

[45] B. van Leer. Toward the ultimate conservative difference scheme. 5, a second-order sequel to godunov's method. *Journal of Computational Physiscs*, Vol. 32, pp. 101–136, 1979.

[46] G. D. van Albada, B. van Leer, and W. W. Roberts. A comparative study of computational methods in cosmic gas dynamics. *Astronomy and Astrophysics*, Vol. 108, pp. 76–84, 1982.

[47] C. W. Shu and S. Osher. Efficient implementation of essentially non-oscillatory shock capturing schemes. *Journal of Computational Physics*, Vol. 77, No. 2, pp. 439–471, 1988.

[48] M. Nishioka and H. Sato. Mechanism of determination of shedding frequency of vortices behind a cylinder at low Reynolds numbers. *Journal of Fluid Mechanics*, Vol. 89, No. 1, pp. 49–60, 1978.

[49] 水島二郎, 藤村薫. 流れの安定性. 朝倉書店, 2003.

[50] S. Kawai. Divergence-free-preserving high-order schemes for magnetohydrodynamics: An artificial magnetic resistivity method. *Journal of Computational Physics*, Vol. 251, pp. 292–318, October 2013.

[51] T. Arasawa, K. Fujii, and K. Miyaji. High-order compact difference scheme applied to double-wing vortical flows. *Journal of Aircraft*, Vol. 41, No. 4, pp. 953–957, 2004.

[52] R. E. Gordnier and M. R. Visbal. Compact difference scheme applied to simulation of low-sweep deltawing flow. *AIAA Journal*, Vol. 43, No. 8, pp. 1744–1752, 2005.

[53] P. E. Morgan, D. P. Rizzetta, and M. R. Visbal. High-order numerical simulation of turbulent flow over a wall-mounted hump. *AIAA Journal*, Vol. 44, No. 2, pp. 239–251, 2006.

[54] S. Kawai and K. Fujii. Compact scheme with filtering for large-eddy simulation of transitional boundary layer. *AIAA Journal*, Vol. 46, No. 3, pp. 690–700, March 2008.

[55] S. Teramoto. Large eddy simulation of Shock wave/Boundary layer interaction. *Transactions of the Japan Society for Aeronautical and Space Sciences*, Vol. 47, No. 275, pp. 268–277, 2005.

[56] J. A. Ekaterinaris. Implicit, high-resolution, compact schemes for gas dynamics and aeroacoustics. *Journal of Computational Physics*, Vol. 156, pp. 272–299, 199.

[57] A. Inasawa, M. Asai, and T. Nakano. Sound generation in the flow behind a rectangular cylinder of various aspect ratios at low mach numbers. *Computers and Fluids*, Vol. 82, pp. 148–157, 2013.

[58] 手塚亜聖, 鈴木宏二郎. 2 次元円柱，3 次元球及び低アスペクト比円柱周り非対称流れの全体安定性解析. 日本航空宇宙学会論文集, Vol. 51, No. 597, pp. 529–536, 2003.

[59] D. H. Rudy and J. C. Strikwerda. A non-reflecting outflow boundary condition for subsonic Navier-Stokes calculations. *Journal of Computational Physics*, Vol. 36, pp. 55–70, 1980.

[60] D. H. Rudy and J. C. Strikwerda. Boundary conditions for subsonic compressible Navier-Stokes calculations. *Computers and Fluids*, Vol. 9, pp. 327–338, 1981.

[61] J. E. Rossiter. Wind-tunnel experiments on the flow over rectangular cavities at subsonic and transonic speeds. Technical report, ARC, 1964.

[62] U. Ghia, K. N. Ghia, and C. T. Shin. High-resolutions for incompressible flows using navier-stokes equations and a multigrid method. *Journal of Computational Physics*, Vol. 48, pp. 387–411, 1982.

[63] J. Kim and P. Moin. Application of a fractional-step method to incompressible navier-stokes equations. *Journal of Computational Physics*, Vol. 59, pp. 308–323, 1985.

[64] T. Kawamura, H. Takami, and K. Kuwahara. New higher-order upwind scheme for incompressible navier-stokes equations. *Lecture Notes in Physics*, Vol. 218, pp. 308–323, 1985.

[65] Charles-Henri Bruneau and Mazen Saad. The 2d lid-driven cavity problem revisited. *Computers and Fluids*, Vol. 35, pp. 326–348, 2006.

[66] J. Shen. Dynamics of regularized cavity flow at high reynolds numbers. *Applied Mathematics Letters*, Vol. 2, No. 4, pp. 381–184, 1989.

[67] J. Shen. Hopf bifurcation of the unsteady regularized driven cavity flow. *Journal of Computational Physics*, Vol. 95, pp. 228–245, 1991.

[68] S. Chandrasekhar. *Hydrodynamic and Hydromagnetic Stability*. Dover, 1981.

Acknowledgment

本研究を進めるにあたり，多くの方々からご指導，ご協力を賜りました．

指導教員である鈴木宏二郎教授には，５年間に渡って懇切なるご指導を頂きました．先生に頂いた全体安定性解析という研究テーマは，研究するほどに惹きこまれ非常に興味深いものであり，私にとって最高の研究テーマでした．また，鈴木先生の下で学ばせて頂く中で，どのようなことも自分なりに解釈してみる，研究を楽しむ，といった研究者としての基本的な姿勢の大切さを再認識することができました．私は研究者としてまだまだ足りない部分が多いと感じておりますが，これらの基本的な姿勢を大切にし，今後も精進してまいります．本当にありがとうございました．

特任助教の矢野良輔先生にはスーパーコンピュータの利用法や，興味深い論文を教えて頂きました．

先輩であり，現宇宙航空研究開発機構 (JAXA) の金森正史さんからは，特に CFD について基礎的なことから応用にいたるまで多くの事を学びました．金森さんから学んだ知識なしに本研究は成し得なかったと思います．ここに感謝の意を表します．

研究で何か悩むことがあれば最初に相談するのは同期の渡邉保真君でした．渡邉君に相談することで解決したことも多く，大変感謝しています．また，同じく同期の濵﨑勝俊君とはよく息抜きに付き合ってもらいました．２人の仲間がいたことで５年間の研究生活を楽しむことができたと思います．

本研究にご協力頂いた多くの先輩，鈴木研究室の皆様に深く感謝するとともに厚くお礼申し上げます．

最後に，大学院生活を支えてくれた両親と家族に感謝の意を表したいと思います．